Supporting Information

Multicomponent Synthesis on a Diiron Platform of Stable Ferrabenzenes with Promising Anticancer Activity

Sara Benetti,[a] Tommaso Nottoli,[a] Zhimei Xiao,[b] Tiziana Funaioli,[a] Stefano Zacchini,[c] Gilles Gasser,[b] Filippo Lipparini,[a] and Fabio Marchetti [a]

[a] University of Pisa, Department of Chemistry and Industrial Chemistry, Via G. Moruzzi 13, 56124 Pisa, Italy
[b] Chimie ParisTech, PSL University, CNRS, Institute of Chemistry for Life and Health Sciences, 75005 Paris, France
[c] University of Bologna, Department of Industrial Chemistry "Toso Montanari", Via P. Gobetti 85, 40129 Bologna, Italy

Table of Contents

1. Synthesis and spectroscopic characterization of compounds

1.1. Materials and methods. Reactants were purchased from Merck or TCI Europe and were of the highest purity available, while solvents were purchased from Merck. THF, CH_2Cl_2 and diethyl ether were purified with the solvent purification system mBraun MB SPS5. Other solvents were used as received, Diiron complexes **1a-d** were prepared according to the literature.[1] Chromatographic purifications were carried out on columns of deactivated alumina (Merck, 3% *w/w* water), using solvents from the bottle unless otherwise specified. Infrared spectra of solutions were recorded on a Perkin Elmer Spectrum 100 FT-IR spectrometer with a CaF_2 liquid transmission cell (2250-1500 cm^{-1} range). UV-Vis spectra were recorded on an Ultraspec 2100 Pro spectrophotometer. IR and UV-Vis spectra were processed with Spectragryph software.[2] NMR spectra for characterization were recorded at 298 K on a Jeol JNM-ECZ400R instrument equipped with a Royal HFX Broadband probe, while NMR spectra for aqueous studies were recorded at 298 K on a Jeol JNM-ECZ500R instrument equipped with a Royal HFX Broadband probe. Chemical shifts (expressed in parts per million) are referenced to the residual solvent peaks (^1H, ^{13}C). [3] NMR spectra were assigned with the assistance of ^1H-^{13}C (*gs*-HSQC and *gs*-HMBC) correlation experiments.[4] NMR signals due to secondary isomeric forms (where detectable) are italicized, and integral values of these ^1H signals are not reported in the text for clarity. Elemental analyses were performed on a Vario MICRO cube instrument (Elementar); analyses for **2b** and **4b** were repeated and found to be satisfactory, after small deviations from calculated values were observed initially. ESI-MS spectra for compound characterization were recorded using an InfinityLab LC/MSD XT mass spectrometer (Agilent, Santa Clara, CA, USA), equipped with AJS source and a single quadrupole detector.

1.2. Diiron vinyliminium complexes (2a-d)

1.2.1. General procedure (Scheme S1)**.** The synthesis of **2a** was previously reported.[5] To obtain **2b-d** and **2a^D**, a solution of **1a-d** (ca. 0.5 mmol) in MeCN (ca. 10 mL) was treated with Me_3NO (1.3 eq.). The resulting mixture was stirred for 1 hour, during which time progressive color-darkening occurred. The complete conversion of the starting material into the corresponding acetonitrile adduct $[Fe_2Cp_2(CO)(\mu\text{-}CO)(NCMe)\{\mu\text{-}CN(Me)(R)\}]CF_3SO_3$ was checked by IR spectroscopy, as is routine for this reaction type.[6] The volatiles were removed under vacuum to afford a dark-brown residue which was dissolved into dichloromethane (ca. 20 mL) and treated with the alkyne (ca. 1.4 eq. unless otherwise specified). The mixture was stirred at room temperature for 2 days, then it was chromatographed on an alumina column in air. Elution with CH_2Cl_2/THF mixtures allowed to separate impurities, then the fraction corresponding to the desired product was isolated using acetonitrile as the eluent. Volatiles were

evaporated under reduced pressure, the residue was dissolved in CH_2Cl_2 and diethyl ether/hexane (1:1 v/v) was added. The obtained precipitate was dried under vacuum and isolated as an air-stable powder.

Scheme S1. Two-step synthesis of diiron vinyliminium complexes via coupling of bridging aminocarbyne ligands with ethynylcyclohexane. Wavy bonds indicate *E*/*Z* stereoisomerism when R ≠ Me. Cy = C_6H_{11} (cyclohexyl); Xyl = 2,6-$C_6H_3Me_2$ (*meta*-xylyl).

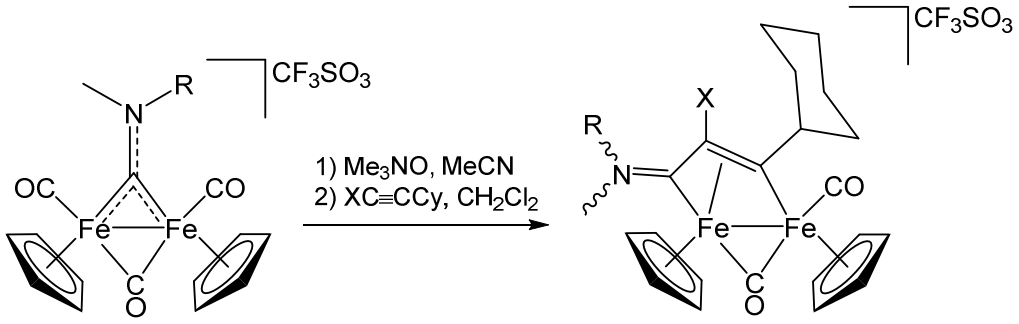

	R	*X*	
1a	4-C_6H_4OMe	H	**2a**
1b	Me	H	**2b**
1c	2-naphthyl	H	**2c**
1d	Xyl	H	**2d**
1a	4-C_6H_4OMe	D	**2a^D**

1.2.2. $[Fe_2Cp_2(CO)(\mu\text{-}CO)\{\mu\text{-}\eta^1\text{:}\eta^3\text{-}C^3(Cy)C^2(H)C^1NMe_2\}]CF_3SO_3$, 2b (Figure S1)

Figure S1. Structure of the cation of **2b**

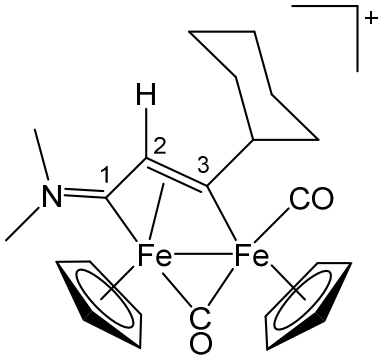

From **1b** (241 mg, 0.444 mmol) and HC≡CCy. Brown solid, yield 236 mg (87%). Anal. calcd. for $C_{24}H_{28}F_3Fe_2NO_5S$: C, 47.16; H, 4.62; N, 2.29; S, 5.25. Found: C, 47.03; H, 4.57; N, 2.21; S, 5.13. IR (CH_2Cl_2): $\tilde{\nu}$/cm^{-1} = 1989vs (CO), 1801s (μ-CO), 1691m (C^1N). ^{1}H NMR (acetone-d_6): δ/ppm = 5.47 (s, 5H, Cp); 5.24 (s, 5H, Cp); 4.69 (s, 1H, C^2H); 4.35 (t, $^3J_{HH}$ = 11.3 Hz, 1H, CH^{Cy}); 3.95 (s, 3H, NMe); 3.30 (s, 3H, NMe); 2.58-2.33 (m, 2H, CH_2^{Cy}); 1.99-1.49 (m, 8H, CH_2^{Cy}). $^{13}C\{^1H\}$ NMR (acetone-d_6): δ/ppm = 257.7 (μ-CO); 226.5 (C^1); 218.9 (C^3); 211.6 (CO); 122.4 (q, $^1J_{CF}$ = 322.0 Hz, $CF_3SO_3^-$); 91.8, 87.8 (Cp); 61.3 (CH^{Cy}); 51.2, 45.0 (NMe); 47.1 (C^2); 41.9, 34.5, 28.3, 27.4, 27.2 (CH_2^{Cy}).

1.2.3. $[Fe_2Cp_2(CO)(\mu\text{-}CO)\{\mu\text{-}\eta^1\text{:}\eta^3\text{-}C^3(Cy)C^2(H)C^1N(Me)(C_{10}H_7)\}]CF_3SO_3$, 2c (Figure S2)

Figure S2. Structure of the cation of **2c** (wavy bonds denote *E-Z* isomers)

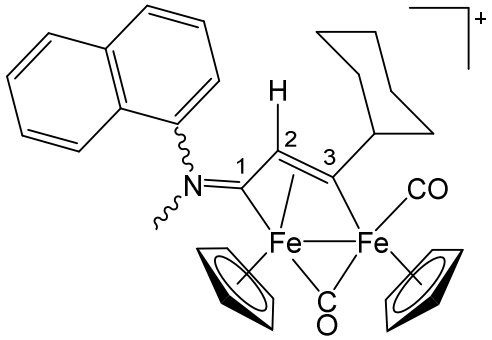

From **1c** (106 mg, 0.165 mmol) and HC≡CCy. Brown solid, yield 97 mg (81%). Anal. calcd. for $C_{33}H_{32}F_3Fe_2NO_5S$: C, 54.79; H, 4.46; N, 1.94; S, 4.43. Found: C, 54.50; H, 4.60; N, 1.98; S, 4.40. IR (CH_2Cl_2): $\tilde{\nu}$/cm^{-1} = 1990vs (CO), 1808s (μ-CO), 1642w, 1625w, (arom CC), 1597m (C^1N). ^{1}H NMR (acetone-d_6): δ/ppm = 7.96-7.29 (s, 7H, CH^{Naph}); 5.60, *5.53* (s, 5H, Cp); 5.42, *5.02* (s, 5H, Cp); *5.10*, 4.87 (s, 1H, C^2H); 4.59, *3.79* (s, 3H, NMe); 4.40 (tt, $^3J_{HH}$= 11.7, 2.7 Hz, 1H, CH^{Cy}); 2.66-2.30 (m, 3H, CH_2^{Cy}); 1.93-1.41 (m, 6H, CH_2^{Cy}); 1.39-1.20 (m, 1H, CH_2^{Cy}). *E*/*Z* ratio = 4. $^{13}C\{^1H\}$ NMR (acetone-d_6): δ/ppm = 256.4, *256.3* (μ-CO); 232.1, *230.2* (C^1); *221.5,* 220.3 (C^3); 211.7 (CO); 144.1, 141.9, 138.2, 134.1, 133.7, 133.5, 130.6, 130.3, 129.3, 128.9, 128.6, 128.3, 126.0, 124.6, 123.2, 120.6, 120.0 ($C_{10}H_7$); 92.4, *92.3*, 88.5, *88.1* (Cp); 61.7 (CH^{Cy}); *54.0*, 46.7 (NMe); 49.1, *48.9* (C^2); *41.8*, 41.7, *34.5*, 34.4, *28.3*, 28.1, *27.4*, 27.2, 27.0, 26.1 (CH_2^{Cy}).

1.2.4. $[Fe_2Cp_2(CO)(\mu\text{-}CO)\{\mu\text{-}\eta^1\text{:}\eta^3\text{-}C^3(Cy)C^2(H)C^1N(Me)(Xyl)\}]CF_3SO_3$, 2d (Figure S3)

Figure S3. Structure of the cation of **2d**

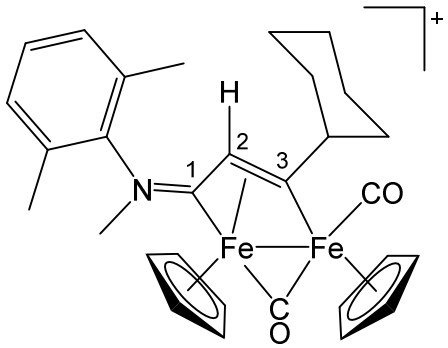

From **1d** (203 mg, 0.327 mmol) and HC≡CCy. Brown solid, yield 200 mg (87%). Anal. calcd. for $C_{33}H_{32}F_3Fe_2NO_5S$: C, 54.79; H, 4.46; N, 1.94; S, 4.43. Found: C, 54.60; H, 4.39; N, 2.03; S, 4.29. IR (CH_2Cl_2): $\tilde{\nu}$/cm^{-1} = 2000vs (CO), 1811s (μ-CO), 1632w (C^1N). ^{1}H NMR (acetone-d_6): δ/ppm = 7.21 (m, 2H, CH^{Xyl}); 7.03 (d, $^3J_{HH}$ = 7.3 Hz, 1H, CH^{Xyl}); 5.64 (s, 5H, Cp); 5.48 (s, 5H, Cp); 4.42 (tt, $^3J_{HH}$ = 11.4 Hz, 2.6 Hz, 1H, CH^{Cy}); 4.34 (s, 3H, NMe); 4.25 (s, 1H, C^2H);

2.32 (s, 3H, Me^{Xyl}); 2.44-2.41, (m, 1H, CH_2^{Cy}); 2.28-2.25 (m, 1H, CH_2^{Cy}); 2.00-1.88, (m, 3H, CH_2^{Cy}); 1.81 (s, 3H, Me^{Xyl}); 1.70-1.59, (m, 2H, CH_2^{Cy}); 1.38-1.21 (m, 3H, CH_2^{Cy}). $^{13}C\{^1H\}$ NMR (acetone-d_6): δ/ppm = 255.7 (μ-CO); 233.8 (C^1); 223.0 (C^3); 211.7 (CO); 145.9 (ipso-C^{Xyl}); 132.9, 132.3 (C^{Xyl}-Me); 130.3, 130.1 (CH^{Xyl}); 92.6, 88.2 (Cp); 62.0 (CH^{Cy}); 47.3 (C^2); 46.4 (NMe); 41.6, 34.5, 28.1, 27.3, 27.0 (CH_2^{Cy}); 18.0, 17.3 (Me^{Xyl}).

1.2.5. $[Fe_2Cp_2(CO)(\mu\text{-}CO)\{\mu\text{-}\eta^1\text{:}\eta^3\text{-}C^3(Cy)C^2(D)C^1N(Me)(4\text{-}C_6H_4OMe)\}]CF_3SO_3$, $2a^D$ (Figure S4)

Figure S4. Structure of the cation of $\mathbf{2a^D}$ (wavy bonds denote *E*-*Z* isomers)

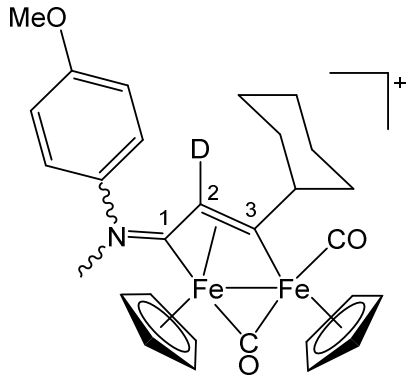

From **1a** (109 mg, 0.175 mmol) and DC≡CCy (approximately 3 eq. in diethyl ether solution, see below). Brown solid, yield 92 mg (75%). IR (CH_2Cl_2): ν̃/cm^{-1} = 1990vs (CO), 1808s (μ-CO), 1635m (C^1N). ^1H NMR (acetone-d_6): δ/ppm = *7.65*, 7.17 (d, $^3J_{HH}$ = 8.9 Hz, 2H, C_6H_4); *7.23,* 6.92 (d, $^3J_{HH}$ = 8.9 Hz, 4H, C_6H_4); 5.56, *5.50* (s, 5H, Cp); 5.37, *5.02* (s, 5H, Cp); 4.42, *3.95* (s, 3H, NMe); 4.37 (m, 1H, CH^{Cy}); 3.79, *3.64* (s, 3H, OMe); 2.62-2.27 (m, 3H, CH_2^{Cy}); 1.95-1.61 (m, 7H, CH_2^{Cy}). *E*/*Z* ratio = 2.

Preparation of ethynylcyclohexane-D (DC≡CCy): ethynylcyclohexane (HC≡CCy) (0.050 mL, 0.38 mmol) was dissolved in purified diethyl ether (5 mL) and treated with BuLi (0.24 mL of a 1.6M hexane solution, 0.38 mmol), at 0 °C. After 15 minutes, the colorless solution was allowed to warm to room temperature and stirred for an additional 2h. During this time, the solution gradually turned yellow, followed by the precipitation of a white solid. A large excess of D_2O (0.1 mL) was then added, resulting in a colorless mixture. After 24 h, H_2O (ca. 5 mL) was added, and the organic phase was extracted. An aliquot of this organic solution was subsequently used for the synthesis of $\mathbf{2a^D}$.

1.3. Ferra-cyclohexadienone complexes (4a-c)

General procedure. A brown solution of **2a-c** (ca. 0.1 mmol) in purified THF (ca. 10 mL) was treated with N_2CHCO_2Et (5 eq) and ^tBuOK (2 eq), in the order given. The reaction mixture was stirred under a N_2 atmosphere for 3 hours, then rapidly filtered through an alumina column under N_2, using purified THF as the eluent. After evaporation of the volatiles under vacuum, the residue was subjected to further purification by alumina

chromatography (under N_2). The crude product was dissolved in the minimum volume of CH_2Cl_2 and loaded onto an alumina column. Impurities were separated using a mixture of CH_2Cl_2 and THF (20:1 v/v) as the eluent. The green band corresponding to **3a-c** was eluted using THF/MeOH (10:1 v/v). After solvent removal under vacuum, the obtained powder was stored under N_2.

Notes: diiron vinyliminium complexes are reactive towards bases of varying strength, including ^tBuOK, and predominantly undergo fragmentation into monoiron species via single-electron reduction;[7] therefore, an excess of N_2CHCO_2Et is required to ensure incorporation of the ethyl diazoacetate moiety, thereby preventing alternative pathways.

1.3.1. [$Fe^2Cp\{\kappa Fe,\kappa^5 C$-$Fe^1(Cp)(CO)C^4(O)C^5(CO_2Et)C^1(NMe(4\text{-}C_6H_4OMe))C^2(H)C^3(Cy)\}$], 4a (Figure S5)

Figure S5. Structure of **4a**

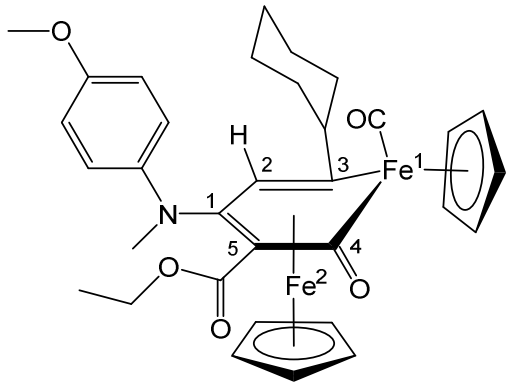

From **2a** (83 mg, 0.12 mmol). Green solid, yield 41 mg (54%). Anal. calcd. for $C_{33}H_{37}Fe_2NO_5$: C, 61.99; H, 5.83; N, 2.19. Found: C, 61.66; H, 5.73; N, 2.11. IR (CH_2Cl_2): $\tilde{\nu}$/cm^{-1} = 1958vs (CO), 1718w (OC=O), 1604m (arom CC), 1510s (C^4O). ^1H NMR (acetone-d_6): δ/ppm = 6.71-6.65 (m, 4H, C_6H_4); 6.59 (s, 1H, C^2H); 4.99 (s, 5H, Fe^1-Cp), 4.72 (s, 5H, Fe^2-Cp); 3.83 (dq, 1H, $^2J_{HH}$ = 10.7 Hz, $^3J_{HH}$ = 7.1 Hz, CH_2^{Et}), 3.71 (m, 1H, CH^{Cy}); 3.61 (dq, 1H, $^2J_{HH}$ = 10.4 Hz, $^3J_{HH}$ = 7.2 Hz, CH_2^{Et}); 3.68 (s, 3H, OMe); 3.08 (s, 3H, NMe); 2.63-2.19 (3, 10H, CH_2^{Cy}), 2.01-1.44 (m, 7H, CH_2^{Cy}); 0.87 (t, 3H, $^3J_{HH}$ = 7.1 Hz, CH_3^{Et}). $^{13}C\{^1H\}$ NMR (acetone-d_6): δ/ppm = 226.0 (C^4); 217.3 (CO); 207.4 (C^3); 170.3 (OCO); 154.7 (COMe); 145.0 (ipso-C_6H_4); 125.3 (C^1); 120.7, 114.5 (arom-CH); 93.3 (Fe^1-Cp); 81.1 (C^2); 80.8 (Fe^2-Cp); 64.9 (C^5); 61.0 (CH_2^{Et}); 61.0 (CH^{Cy}); 55.7 (OMe); 42.1 (NMe); 42.0, 34.6, 28.6, 28.0, 27.6 (CH_2^{Cy}); 14.1 (CH_3^{Et}). ESI-MS (CH_2Cl_2): $[M + H]^+$ *m/z* = 640.2, 100% (theoretical for $[C_{33}H_{38}Fe_2NO_5]^+$, *m/z* = 640.1); $[M + H - CO]^+$ *m/z* = 612.2, 19% (theoretical for $[C_{32}H_{38}Fe_2NO_4]^+$: *m/z* = 612.1). Crystals suitable for X-ray analysis were obtained from a saturated solution of **4a** in acetone, which was allowed to settle at –30°C. The intermediate formation of **3a** was detected by monitoring the reaction leading to **4a** via IR spectroscopy; IR (**3a**, THF): $\tilde{\nu}$/cm^{-1} = 1953vs (CO), 1779s (μ-CO).

1.3.2. [$Fe^2Cp\{\kappa Fe,\kappa^5 C\text{-}Fe^1(Cp)(CO)C^4(O)C^5(CO_2Et)C^1(NMe_2)C^2(H)C^3(Cy)\}$], 4b (Figure S6)

Figure S6. Structure of **4b**

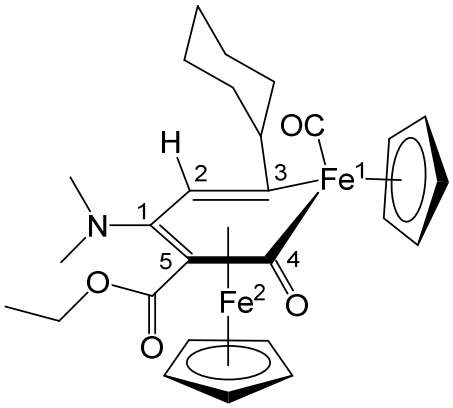

From **1b** (86 mg, 0.14 mmol). Green solid, yield 65 mg (84%). Anal. calcd. for $C_{27}H_{33}Fe_2NO_4$: C, 59.26; H, 6.08; N, 2.56. Found: C, 59.21; H, 6.14; N, 2.48. IR (CH_2Cl_2): $\tilde{\nu}/cm^{-1}$ = 1962vs (CO), 1720m (OC=O). ^1H NMR (acetone-d_6): δ/ppm = 6.56 (s, 1H, C^2H); 4.93 (s, 5H, Fe^1-Cp), 4.61 (s, 5H, Fe^2-Cp); 4.28 (dq, 1H, $^2J_{HH}$ = 10.4 Hz, $^3J_{HH}$ = 7.1, CH_2^{Et}); 4.18 (dq, 1H, $^2J_{HH}$ = 10.4 Hz, $^3J_{HH}$ = 7.1, CH_2^{Et}); 3.67 (tt, 1H, J = $^3J_{HH}$ = 11.2, 2.6 Hz, CH^{Cy}); 2.60-2.56 (m, 1H, CH_2^{Cy}), 2.45-2.19 (m, 2H, CH_2^{Cy}), 2.00-1.82 (m, 4H, CH_2^{Cy}), 1.71-1.46 (m, 3H, CH_2^{Cy}); 2.53 (s, 6H, NMe); 1.30 (t, 3H, $^3J_{HH}$ = 7.1 Hz, CH_3^{Et}). $^{13}C\{^1H\}$ NMR (acetone-d_6): δ/ppm = 227.3 (C^4); 216.5 (CO); 207.2 (C^3); 171.0 (OCO); 128.5 (C^1); 92.9 (Fe^1-Cp); 80.2 (Fe^2-Cp); 75.2 (C^2); 63.5 (C^5); 61.1 (CH_2^{Et}); 60.9 (CH^{Cy}); 45.2 (NMe); 34.6, 28.6, 28.0, 27.7, 21.0 (CH_2^{Cy}); 14.5 (CH_3^{Et}). ESI-MS (CH_2Cl_2): $[M + H]^+$ *m/z* = 548.1 (theoretical for $[C_{27}H_{34}Fe_2NO_4]^+$: *m/z* = 548.1).

1.3.3. [$Fe^2Cp\{\kappa Fe,\kappa^5 C\text{-}Fe^1(Cp)(CO)C^4(O)C^5(CO_2Et)C^1(NMe(C_{10}H_7))C^2(H)C^3(Cy)\}$], 4c (Figure S7)

Figure S7. Structure of **4c**

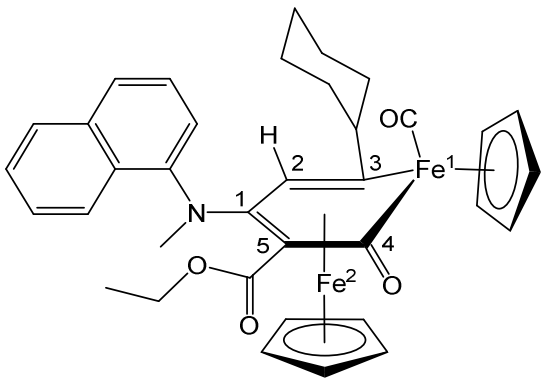

From **1c** (62 mg, 0.086 mmol). Green solid, yield 34 mg (60%). Anal. calcd. for $C_{36}H_{37}Fe_2NO_4$: C, 65.58; H, 5.66; N, 2.12. Found: 65.31; H, 5.77; N, 2.20. IR (CH_2Cl_2): $\tilde{\nu}/cm^{-1}$ = 1960vs (CO), 1718w (OC=O), 1629, 1599w (arom CC), 1508w (C^4O). ^1H NMR (acetone-d_6): δ/ppm = 7.67 (d, J_{HH} = 8.1 Hz, 1H, CH^{Naph}), 7.52 (dd, $^3J_{HH}$ = 13.2, 8.6 Hz,

2H, CH^{Naph}), 7.31 (dd, J_{HH} = 8.6, 7.5 Hz, 1H, CH^{Naph}), 7.20 (t, J_{HH} = 7.5 Hz, 1H, CH^{Naph}), 7.04 (m, 1H, CH^{Naph}); 6.70 (s, 1H, C^2H); 5.03 (s, 5H, Fe^1-Cp), 4.79 (s, 5H, Fe^2-Cp); 3.71 (m, 1H, CH^{Cy}); 3.49 (m, 2H, CH_2^{Et}); 3.24 (s, 3H, NMe); 2.66-2.26 (m, 3H, CH_2^{Cy}), 1.90-1.83 (m, 2H, CH_2^{Cy}), 1.75-1.24 (m, 5H, CH_2^{Cy}); 0.56 (t, 3H, $^3J_{HH}$ = 7.1 Hz, CH_3^{Et}). $^{13}C\{^1H\}$ NMR (acetone-d_6): δ/ppm = 225.8 (C^4); 217.4 (CO); 208.0 (C^3); 170.0 (OCO); 148.6 (ipso-C^{Naph}); 135.3, 129.0 (C^{Naph}); 128.3, 128,1, 127.2, 126.7, 123.6, 120.2, 111.8 (CH^{Naph}); 124.1 (C^1); 93.5 (Fe^1-Cp); 83.6 (C^2); 81.1 (Fe^2-Cp); 64.9 (C^5); 61.0 (CH_2^{Et}); 60.9 (CH^{Cy}); 42.0 (NMe); 41.8, 34.6, 28.6, 28.0, 27.6 (CH_2^{Cy}); 13.7 (CH_3^{Et}). ESI-MS (CH_2Cl_2): $[M + H]^+$ *m/z* = 660.2, 100% (theoretical for $[C_{36}H_{38}Fe_2NO_4]^+$: *m/z* = 660.2); $[M + H - CO]^+$ *m/z* = 631.2, 4.8% (theoretical for $[C_{35}H_{38}Fe_2NO_3]^+$: *m/z* = 631.2). The intermediate formation of **3c** was detected by monitoring the reaction leading to **4c** via IR spectroscopy; IR (**3c**, THF): $\tilde{\nu}/cm^{-1}$ = 1955vs (CO), 1782s (μ-CO).

1.3.4. Synthesis and isolation of azine-bis(alkylidene) complex, $[Fe_2Cp_2(CO)(\mu\text{-}CO)\{\mu\text{-}\eta^1\text{:}\eta^2\text{-}C^3(Cy)C^2(=NN=CHCO_2Et)C^1N(Me)(Xyl)\}]$, 3d (Figure S8)

The reaction of **1d** (103 mg, 0.147 mmol) with N_2CHCO_2Et (5 eq.) and ^tBuOK (2 eq.) and the subsequent work-up were performed using the same procedure described in Section 1.3. Reaction time: 5 h; eluent for chromatography: THF 100%.

Figure S8. Structure of **3d** (wavy bonds denote *Z-E* isomers)

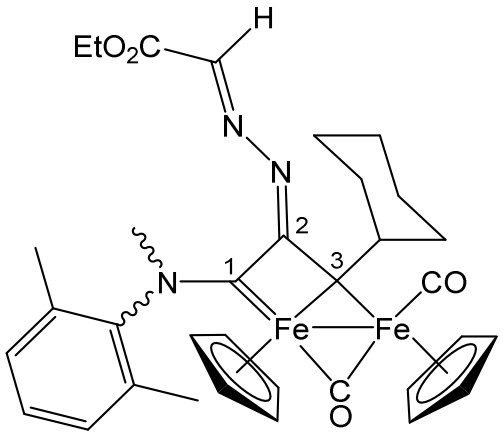

Green solid, yield 60 mg (61%). Anal. calcd. for $C_{34}H_{39}Fe_2N_3O_4$: C, 61.37; H, 5.91; N, 6.32. Found: 61.15; H, 6.05; N, 6.07. IR (CH_2Cl_2): $\tilde{\nu}/cm^{-1}$ = 1948s (CO), 1777vs (μ-CO), 1680m (OCO), 1566w, 1518 (CN). ^1H NMR ($CDCl_3$): δ/ppm, *7.75,* 7.64, (s, 1H, NNCH); 7.36-7.17 (m, 3H, CH^{Xyl}), 4.90, *4.29* (s, 5H, Cp); *4.61,* 4.45 (s, 5H, Cp); 4.19 (m, 3H, CH_2^{Et} + CH^{Cy}); *3.40,* 3.15 (s, 3H, NMe); 2.63, (s, 3H, Me^{Xyl}); 2.09 (s, 3H, Me^{Xyl}); 2.52-2.20, (m, 4H, CH_2^{Cy}) 2.03-1.93, (m, 3H, CH_2^{Cy}); 1.61-1.49 (m, 3H, CH_2^{Cy}); 1.25 (t, $^3J_{HH}$ = 7.1 Hz, CH_3^{Et}). *Z*/*E* ratio ≈ 6. $^{13}C\{^1H\}$ NMR ($CDCl_3$): δ/ppm = 269.0 (μ-CO); 243.8 (C^1); 214.7 (CO); 199.9 (C^3); 166.1 (OCO); 143.5 (ipso-C^{Xyl}); 136.2, 134.6 (C^{Xyl});

134.3 (NNCH); 128.8, 128.6 (CH^{Xyl}); 128.5 (C^2); 89.3, 86.5 (Cp); 59.7 (CH_2^{Et}); 68.1 (CH^{Cy}), 50.3 (NMe); 34.7, 29.9, 28.4, 27.2 (CH_2^{Cy}); 19.2 (Me^{Xyl}); 14.7 (CH_3^{Et}). ESI-MS (CH_2Cl_2): $[M + H]^+$ *m/z* = 666.2, 100% (theoretical for $[C_{34}H_{40}Fe_2N_3O_4]^+$: *m/z* = 667.2); $[M + H - CO]^+$ *m/z* = 638.2, 100% (theoretical for $[C_{33}H_{40}Fe_2N_3O_3]^+$: *m/z* = 638.2).

Complex **3d**, in THF solution, underwent extensive decomposition when heated at ≈ 50 °C for 2 hours.

Scheme S2. Main resonance forms representing the structure of complex **4a** based on X-ray crystallography (Cy = cyclohexyl, R = 4-C_6H_4OMe). Fe – FeC_5 ring connections are highlighted in red for clarity.

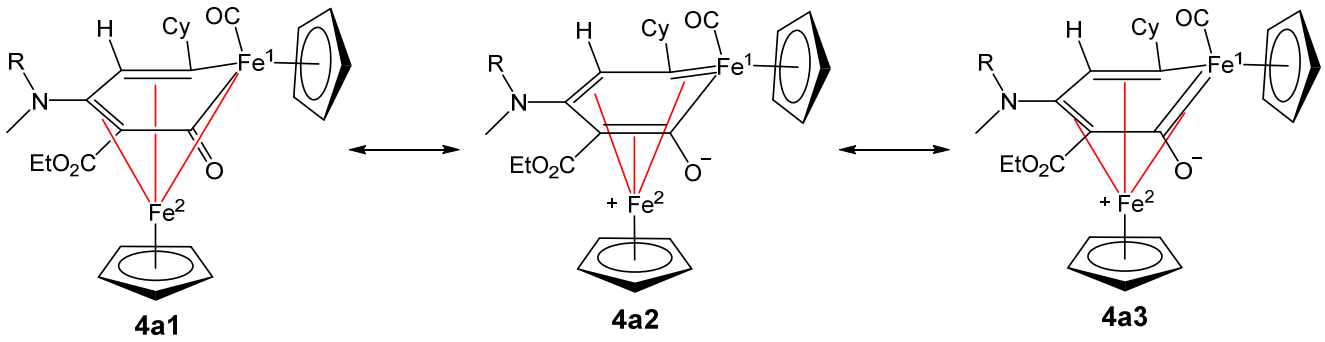

According to IUPAC rules for organometallic complexes, the oxidation states for the iron atoms are: in **4a1**, Fe^1 +III and Fe^2 +I; in **4a2** and **4a3**, Fe^1 +II and Fe^2 +II

1.4. Iron-coordinated ferrabenzenes (5)

General procedure. A solution of **4a-c** in purified dichloromethane (15 mL) was treated with 1.5 eq. of methyl or ethyl triflate while stirring under N_2 atmosphere. After approximately 5 hours, IR analysis on an aliquot from the reaction mixture indicated the complete consumption of **4a-c**. The final solution was dried under vacuum, and the residue was washed first with diethyl ether (50 mL) and then with hexane (2 x 40 mL). The resulting green powder was dried under vacuum and stored in air.

1.4.1. $[Fe^2Cp\{\kappa Fe,\kappa^5 C\text{-}Fe^1(Cp)(CO)C^4(OMe)C^5(CO_2Et)C^1(NMe(4\text{-}C_6H_4OMe))C^2(H)C^3(Cy)\}]CF_3SO_3$, 5a (Figure S9)

Figure S9. Structure of the cation of **5a**

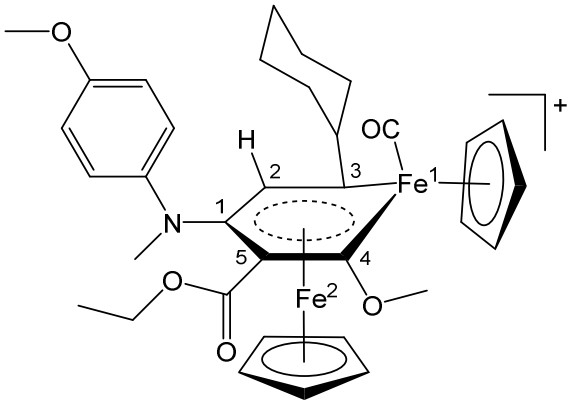

From **4a** (41 mg, 0.064 mmol) and methyl triflate. Green solid, yield 44 mg (86%). Anal. calcd. for $C_{35}H_{40}F_3Fe_2NO_8S$: C, 52.32; H, 5.02; N, 1.74; S, 3.99. Found: C, 52.10; H, 5.14; N, 1.68; S, 4.05. IR (CH_2Cl_2): $\tilde{\nu}$/cm^{-1} = 2002vs (CO), 1728m (OC=O), 1607w (C_6H_4), 1510s (C^1N). ^{1}H NMR (acetone-d_6): δ/ppm = 6.89 (s, 4H, C_6H_4); 6.39 (s, 1H, C^2H); 5.74 (s, 5H, Fe^1-Cp), 5.27 (s, 5H, Fe^2-Cp); 4.05 (dq, 1H, $^2J_{HH}$ = 10.4 Hz, $^3J_{HH}$ = 7.1 Hz, CH_2^{Et}); 3.73 (dq, 1H, $^{2mm}J_{HH}$ = 10.4 Hz, $^3J_{HH}$ = 7.1 Hz, CH_2^{Et}); 4.0 (m, 1H, CH^{Cy})*; 3.99 (s, 3H, C^4OMe); 3.79 (s, 3H, C_6H_4OMe); 3.35 (s, 3H, NMe); 2.60-2.19, (m, 3H, CH_2^{Cy}) 1.94-1.39 (m, 7H, CH_2^{Cy}); 1.19 (t, 3H, $^3J_{HH}$ = 7.1 Hz, CH_3^{Et}). ^{13}C{^{1}H} NMR (acetone-d_6): δ/ppm = 237.4 (C^4); 222.3 (C^3); 212.3 (CO); 167.5 (OCO); 158.4 (COMe); 141.9 (ipso-C_6H_4); 130.7 (C^1); 127.4, 115.5 (C_6H_4); 101.5 (C^5); 93.8 (Fe^1-Cp); 84.7 (Fe^2-Cp); 72.9 (C^2); 65.7 (C^4OMe); 63.3 (CH_2^{Et}); 62.4 (CH^{Cy}); 55.8 (C_6H_4OMe); 43.2 (NMe); 41.6, 34.3, 28.3, 27.4, 27.2 (CH_2^{Cy}); 13.9 (CH_3^{Et}). *Assigned via HSQC experiment. ESI-MS (CH_2Cl_2): $[M]^+$ *m/z* = 654.2 (theoretical for $[C_{34}H_{40}Fe_2NO_5]^+$: *m/z* = 654.2).

1.4.2. [$Fe^2Cp\{\kappa Fe,\kappa^5 C\text{-}Fe^1(Cp)(CO)C^4(OMe)C^5(CO_2Et)C^1(NMe_2)C^2(H)C^3(Cy)\}$]$CF_3SO_3$, 5b (Figure S10)

Figure S10. Structure of the cation of **5b**

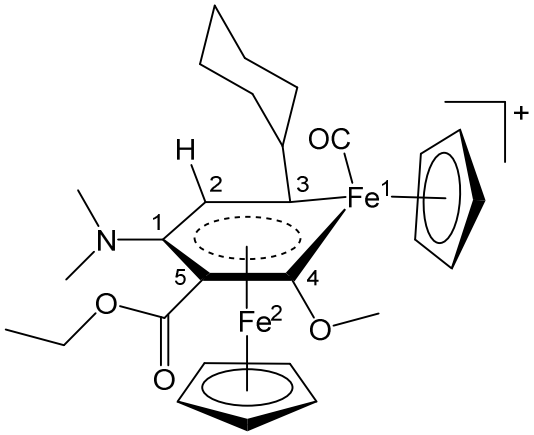

From **4b** (49 mg, 0.090 mmol) and methyl triflate. Green solid, yield 53 mg (83%). Anal. calcd. for $C_{29}H_{36}F_3Fe_2NO_7S$: C, 48.96; H, 5.10; N, 1.96; S, 4.51. Found C, 48.79; H, 5.18; N, 1.81; S, 4.50. IR (CH_2Cl_2): $\tilde{\nu}$/cm^{-1} = 2003vs (CO), 1724m (OC=O), 1522m (C^1N). ^{1}H NMR (acetone-d_6): δ/ppm = 6.24 (s, 1H, C^2H); 5.68 (s, 5H, Fe^1-Cp), 5.18 (s, 5H,

Fe^2-Cp); 4.53 (q, $^3J_{HH}$ = 7.1 Hz, 1H, CH_2^{Et}); 4.52 (q, $^3J_{HH}$ = 7.1 Hz, 1H, CH_2^{Et}); 4.08 (s, 3H, OMe); 4.04 (tt, $^3J_{HH}$ = 11.4, 2.4 Hz, 1H, CH^{Cy}); 2.96 (s, 6H, NMe); 2.58-2.15 (m, 4H, CH_2^{Cy}) 1.92-1.60 (m, 6H, CH_2^{Cy}); 1.48 (t, $^3J_{HH}$ = 7.1 Hz, 3H, CH_3^{Et}). $^{13}C\{^1H\}$ NMR (acetone-d_6): δ/ppm = 237.8 (C^4); 221.6 (C^3); 212.1 (CO); 169.8 (OCO); 135.3 (C^1); 93.4 (Fe^1-Cp); 93.1 (C^5); 83.9 (Fe^2-Cp); 71.2 (C^2); 65.4 (OMe); 63.5 (CH_2^{Et}); 62.1 (CH^{Cy}); 43.0 (NMe); 41.8, 34.0, 28.1, 27.2, 27.0 (CH_2^{Cy}); 14.1 (CH_3^{Et}). ESI-MS (CH_2Cl_2): $[M]^+$ *m/z* = 562.2 (theoretical for $[C_{28}H_{36}Fe_2NO_4]^+$: *m/z* = 562.1).

1.4.3. $[Fe^2Cp\{\kappa Fe,\kappa^5 C\text{-}Fe^1(Cp)(CO)C^4(OMe)C^5(CO_2Et)C^1(NMe(C_{10}H_7))C^2(H)C^3(Cy)\}]CF_3SO_3$, 5c (Figure S11)

Figure S11. Structure of the cation of **5c**

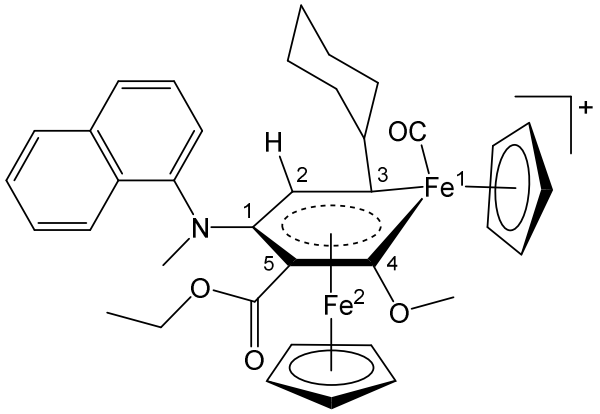

From **4c** (40 mg, 0.060 mmol) and methyl triflate. Green solid, yield 40 mg (80%). Anal. calcd. for $C_{38}H_{40}F_3Fe_2NO_7S$: C, 55.42; H, 4.90; N, 1.70; S, 3.89. Found: C, 55.33; H, 4.78; N, 1.82; S, 3.94. IR (CH_2Cl_2): $\tilde{\nu}/cm^{-1}$ = 2003vs (CO), 1729m (OC=O), 1629, 1600m (arom CC), 1508w (C^1N). ^1H NMR (acetone-d_6): δ/ppm = 7.85-7.10 (m, 7H, CH^{Naph}); 6.61 (s, 1H, C^2H); 5.81 (s, 5H, Fe^1-Cp), 5.39 (s, 5H, Fe^2-Cp); 4.14 (tt, $^3J_{HH}$ = 11.2, 2.4 Hz, 1H, CH^{Cy}); 4.00 (s, 3H, OMe); 3.90, 3.38 (dq, $^2J_{HH}$ = 10.8 Hz, $^3J_{HH}$ = 7.2 Hz, CH_2^{Et}); 3.49 (s, 3H, NMe); 2.61-2.58 (m, 1H, CH_2^{Cy}); 2.31-2.26 (m, 2H, CH_2^{Cy}) 1.96-1.60 (m, 7H, CH_2^{Cy}); 0.77 (t, 3H, $^3J_{HH}$ = 7.1 Hz, CH_3^{Et}). $^{13}C\{^1H\}$ NMR (acetone-d_6): δ/ppm = 237.5 (C^4); 222.3 (C^3); 212.1 (CO); 167.1 (OCO); 146.8 (ipso-C^{Naph}); 134.8, 131.2 (C^{Naph}); 129.8, 128.4, 127.9, 127.6, 127.5, 123.2, 119.8 (CH^{Naph}); 126.1 (C^1); 104.4 (C^5); 94.4 (Fe^1-Cp); 85.3 (Fe^2-Cp); 77.4 (C^2); 65.7 (OMe); 63.3 (CH_2^{Et}); 62.6 (CH^{Cy}); 42.4 (NMe); 41.5, 34.3, 28.3, 27.4, 27.1 (CH_2^{Cy}); 13.5 (CH_3^{Et}). ESI-MS (CH_2Cl_2): $[M]^+$ *m/z* = 674.2, 89% (theoretical for $[C_{37}H_{40}Fe_2NO_4]^+$: *m/z* = 674.2); $[M - CO]^+$ *m/z* = 646.2, 8% (theoretical for $[C_{36}H_{40}Fe_2NO_3]^+$: *m/z* = 646.2).

1.4.4. $[Fe^2Cp\{\kappa Fe,\kappa^5 C\text{-}Fe^1(Cp)(CO)C^4(OEt)C^5(CO_2Et)C^1(NMe(4\text{-}C_6H_4OMe))C^2(H)C^3(Cy)\}]CF_3SO_3$, 5aEt (Figure S12)

Figure S12. Structure of the cation of **5aEt**

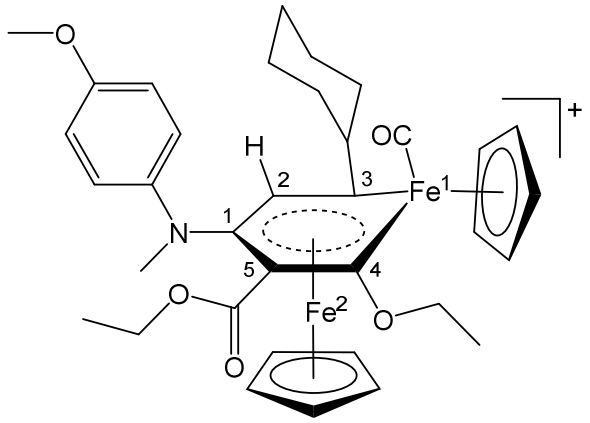

From **4a** (90 mg, 0.14 mmol) and ethyl triflate. Green solid, yield 94 mg (82%). Anal. calcd. for $C_{36}H_{42}F_3Fe_2NO_8S$: C, 52.89; H, 5.18; N, 1.71; S, 3.92. Found: C, 52.68; H, 5.16; N, 1.79; S, 4.03. IR (CH_2Cl_2): $\tilde{\nu}/cm^{-1}$ = 2002vs (CO), 1728m (OC=O)**,** 1607w (C_6H_4), 1510s (C^1N). ^1H NMR (acetone-d_6): δ/ppm = 6.88 (s, 4H, C_6H_4); 6.40 (s, 1H, C^2H); 5.72 (s, 5H, Fe^1-Cp), 5.28 (s, 5H, Fe^2-Cp); 4.19 (q, 2H, $^3J_{HH}$ = 6.9 Hz, $OC\underline{H_2}CH_3$), 4.07 (m, 2H, CH^{Cy} + $OCOCH_2$); 3.78 (b, 5H, OMe + $OCOCH_2$); 3.34 (s, 3H, NMe); 2.58-2.17, (m, 4H, CH_2^{Cy}); 1.99-1.60 (m, 6H, CH_2^{Cy}); 1.44 (t, 3H, $^3J_{HH}$ = 6.9 Hz, $OCH_2C\underline{H_3}$); 1.19 (t, 3H, $^3J_{HH}$ = 7.1 Hz, $OCOCH_2C\underline{H_3}$). $^{13}C\{^1H\}$ NMR (acetone-d_6): δ/ppm = 235.6 (C^4); 221.9 (C^3); 212.3 (CO); 167.5 (OCO); 158.3 ($\underline{C}OMe$); 142.1 (ipso-C_6H_4); 130.2 (C^1); 127.0, 115.5 (C_6H_4); 101.7 (C^5); 93.9 (Fe^1-Cp); 84.8 (Fe^2-Cp); 73.8 (C^2); 73.8 ($O\underline{C}H_2CH_3$); 63.5 ($OCO\underline{C}H_2CH_3$); 62.4 (CH^{Cy}); 55.8 ($C_6H_4O\underline{Me}$); 43.2 (NMe); 41.6, 34.3, 28.3, 27.4, 27.2 (CH_2^{Cy}); 13.9 ($OCOCH_2\underline{C}H_3$). ESI-MS (CH_2Cl_2): $[M]^+$ *m/z* = 668.2 (theoretical for $[C_{35}H_{42}Fe_2NO_5]^+$: *m/z* = 668.2). Crystals suitable for X-ray analysis were obtained by slow diffusion of diethyl ether into a dichloromethane solution of **5aEt** maintained at -30°C.

1.5. Experimental mechanistic studies

Initially, complex **2a^{D}** was synthesized as described in Section 1.2.4. Then, a solution of **2a^{D}** (ca. 0.1 mmol) in purified THF (ca. 10 mL) was treated with N_2CHCO_2Et (5 eq.) and $^{t}BuOK$ (2 eq.). The resulting mixture was stirred under a N_2 atmosphere for 2h. The solution obtained was passed through a short alumina pad under N_2, using purified THF as the eluent. After the volatiles were evaporated under vacuum, the residue was subjected to a more careful alumina chromatography (under N_2). This solid was dissolved in the minimum volume of CH_2Cl_2 and this solution was loaded on top of an alumina column. Impurities were separated using a CH_2Cl_2/THF (15:1 *v/v*) mixture, while the green fraction corresponding to **4a** was collected using neat THF as the eluent. A solution of the residue in purified CH_2Cl_2 (15 mL) was treated with methyl triflate (ca. 1 eq. with respect to **2a^{D}**). After stirring for 4 hours, the solution was dried under vacuum, and the residue was washed with diethyl ether (20 mL) and then hexane (2 x 10 mL). The green powder obtained was dried under vacuum and stored in air. Subsequent ^{1}H NMR analysis revealed the clean formation of $C^{2}H$-containing **5a** (Scheme S3 and Figure S48).

To gain further insights, the reaction of **2a** with N_2CHCO_2Et (5 eq.) and $^{t}BuOK$ (2 eq.) was conducted following the procedure described in Section 1.3, with the only variation being the use of deuterated tetrahydrofuran (THF-d_8, 1.5 mL) in place of non-deuterated THF. ^{1}H NMR analysis of the final reaction mixture revealed the exclusive formation of deuterium-free **4a**.

Scheme S3. Mechanistic study of the multicomponent reaction leading to ferrabenzene formation from a deuterated diiron vinyliminium complex.

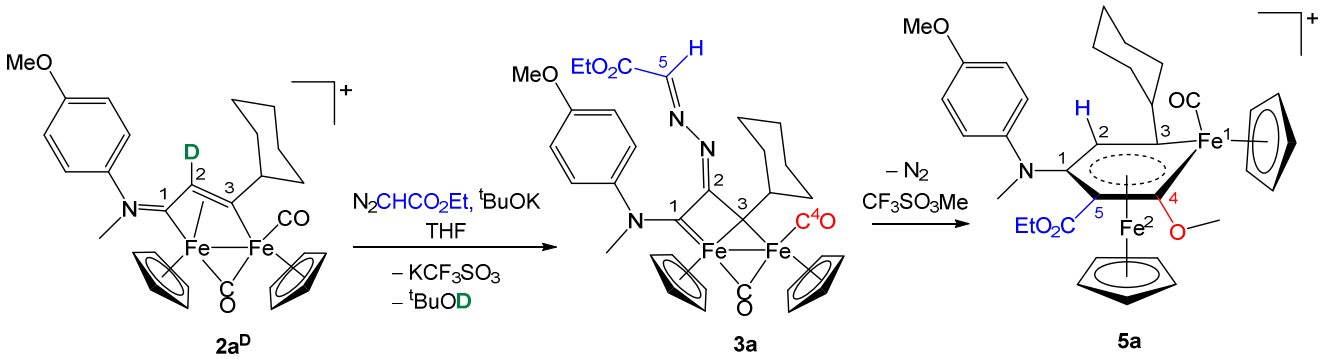

2. X-Ray Crystallography

Crystal data and collection details for **4a** and **5aEt** are reported in Table S1, while selected bonding parameters are compiled in Table S2. Data were recorded on a Bruker APEX II diffractometer equipped with a PHOTON2 detector using Mo–Kα radiation. Data were corrected for Lorentz polarization and absorption effects (empirical absorption correction SADABS).[8] The structures were solved by direct methods and refined by full-matrix least-squares based on all data using F^2.[9] Hydrogen atoms were fixed at calculated positions and refined by a riding model. All non-hydrogen atoms were refined with anisotropic displacement parameters.

Table S1. Crystal data and measurement details for **4a** and **5aEt**.

	4a	**5aEt**
Formula	$C_{36}H_{43}Fe_2NO_6$	$C_{36}H_{42}F_3Fe_2NO_8S$
FW	697.41	817.46
T, K	100(2)	294(2)
λ, Å	0.71073	0.71073
Crystal system	Monoclinic	Monoclinic
Space group	$P2_1/c$	$P2_1/c$
a, Å	16.870(4)	10.5186(9)
b, Å	10.896(3)	14.0466(11)
c, Å	17.187(4)	25.390(2)
β, °	91.391(10)	97.623(2)
Cell Volume, Å^3	3158.3(13)	3718.2(5)
Z	4	4
D_c, g·cm^{-3}	1.467	1.460
μ,mm^{-1}	0.967	0.902
F(000)	1464	1696
Crystal size, mm	0.24×0.21×0.18	0.15×0.13×0.11
θ limits,°	2.213–26.999	1.618–25.059
Reflections collected	47052	24226
Independent reflections	6882 [R_{int} = 0.0293]	6517 [R_{int} = 0.0528]
Data / restraints /parameters	6882 / 0 / 411	6517 / 216 / 501
Goodness on fit on F^2	1.108	1.035
R_1 ($I > 2\sigma(I)$)	0.0277	0.0446
wR_2 (all data)	0.0672	0.1321
Largest diff. peak and hole, e Å^{-3}	0.425 / –0.359	0.402 / –0.395

Table S2. Selected bond lengths (Å) and angles (°) for **4a** and **5aEt**.

	4a	**5aEt**
Fe(1)-Fe(2)	2.6251(5)	2.5708(6)
Fe(1)-C(6)	1.7446(16)	1.755(4)
Fe(1)-C(3)	1.9530(14)	1.954(3)
Fe(1)-C(4)	1.9636(16)	1.915(3)
Fe(1)-Cp	2.1171(16)-2.1691(16)	2.114(3)-2.170(4)
Fe(2)-Cp	2.0686(16)- 2.0913(16)	2.073(3)- 2.094(3)
Fe(2)-C(1)	2.1066(15)	2.218(3)
Fe(2)-C(2)	2.0724(14)	2.088(3)
Fe(2)-C(3)	2.0131(15)	2.027(3)
Fe(2)-C(4)	2.2478(15)	2.012(3)
Fe(2)-C(5)	2.0826(15)	2.087(3)
C(2)-C(3)	1.417(2)	1.408(4)
C(4)-C(5)	1.465(2)	1.431(4)
C(1)-C(2)	1.422(2)	1.429(4)
C(1)-C(5)	1.428(2)	1.436(4)
C(1)-N(1)	1.4315(18)	1.387(4)
N(1)-C(10)	1.4498(19)	1.470(4)
N(1)-C(11)	1.4045(19)	1.424(4)
C(4)-O(2)	1.2435(18)	1.384(3)
O(2)-C(24)	-	1.447(4)
C(6)-O(1)	1.1508(19)	1.139(4)
Fe(1)-C(6)-O(1)	176.47(13)	179.1(3)
C(3)-Fe(1)-C(4)	97.80(6)	92.56(12)
Fe(1)-C(3)-C(2)	120.17(10)	121.4(2)
C(3)-C(2)-C(1)	123.90(13)	126.8(3)
C(2)-C(1)-C(5)	124.80(13)	121.1(3)
C(1)-C(5)-C(4)	127.47(13)	123.4(3)
C(5)-C(4)-Fe(1)	116.97(10)	124.7(2)
C(1)-N(1)-C(10)	121.03(12)	121.3(3)
C(1)-N(1)-C(11)	118.17(12)	118.8(2)
C(10)-N(1)-C(11)	120.48(12)	117.3(3)
Fe(1)-C(4)-O(2)	123.67(11)	122.3(2)
C(5)-C(4)-O(2)	119.34(14)	112.8(3)
C(4)-O(2)-C(24)	-	114.3(2)

3. IR and NMR spectra

Figure S13. IR spectrum (CH_2Cl_2 solution) of **2b**

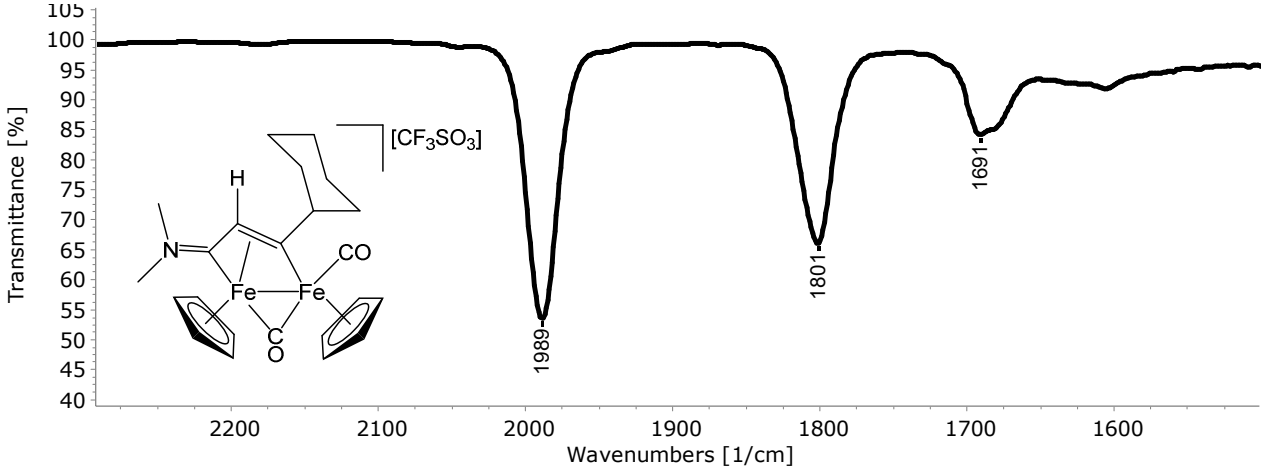

Figure S14. IR spectrum (CH_2Cl_2 solution) of **2c**

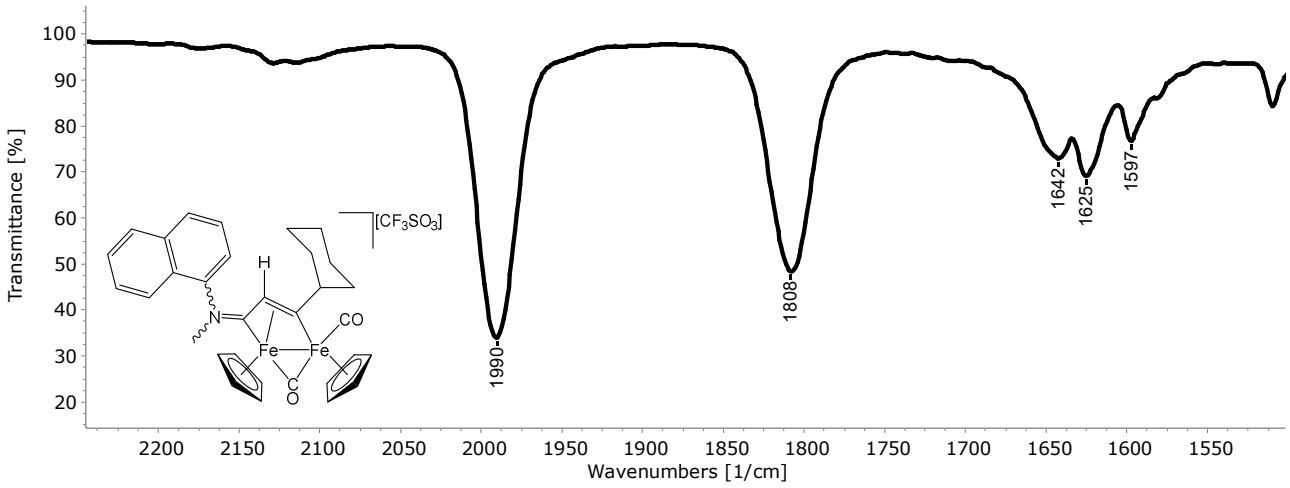

Figure S15. IR spectrum (CH_2Cl_2 solution) of **2d**

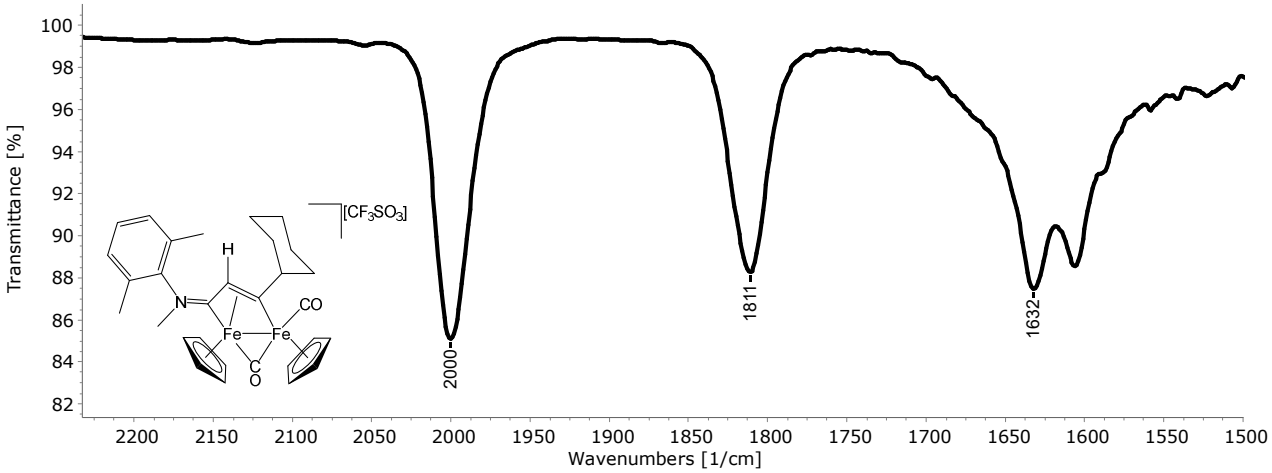

Figure S16. IR spectrum (CH_2Cl_2 solution) of **2a^D**

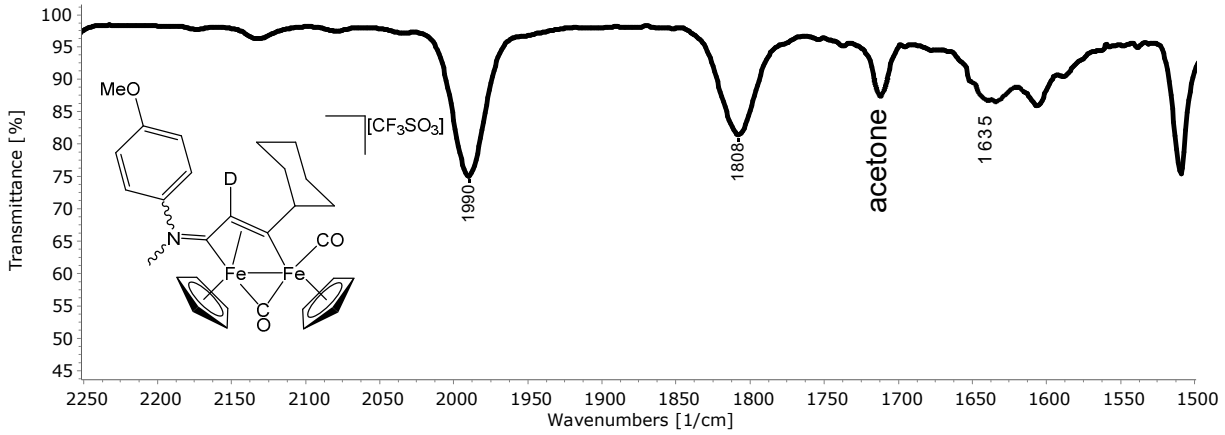

Figure S17. IR spectrum (CH_2Cl_2 solution) of **4a**

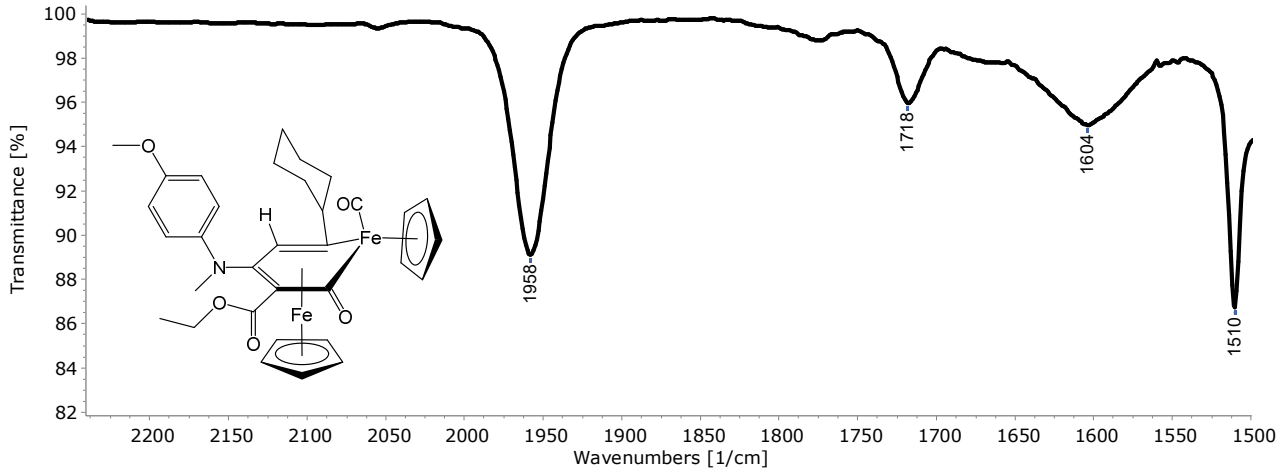

Figure S18. IR spectrum (CH_2Cl_2 solution) of **4b**

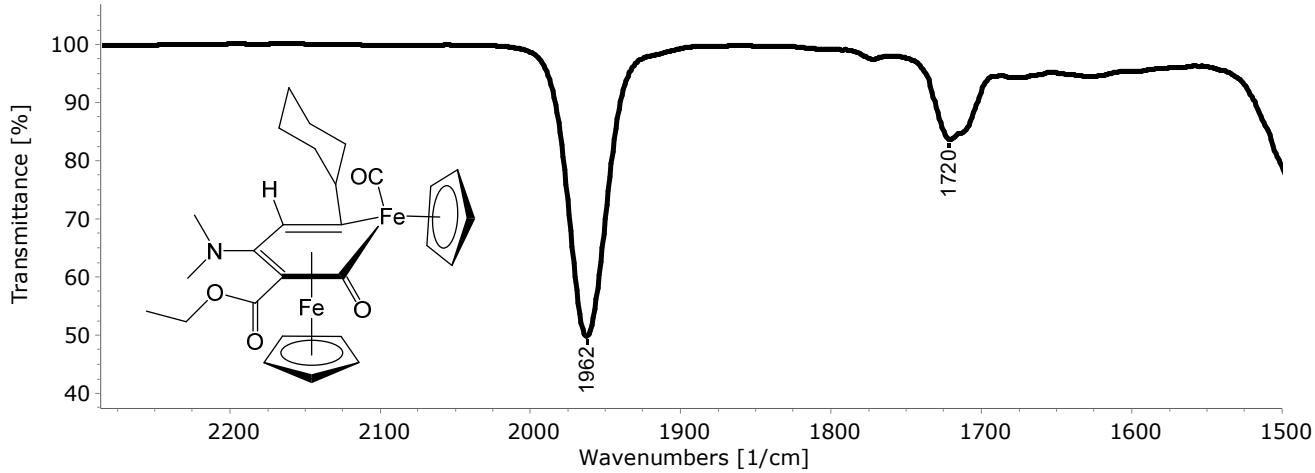

Figure S19. IR spectrum (CH_2Cl_2 solution) of **4c**

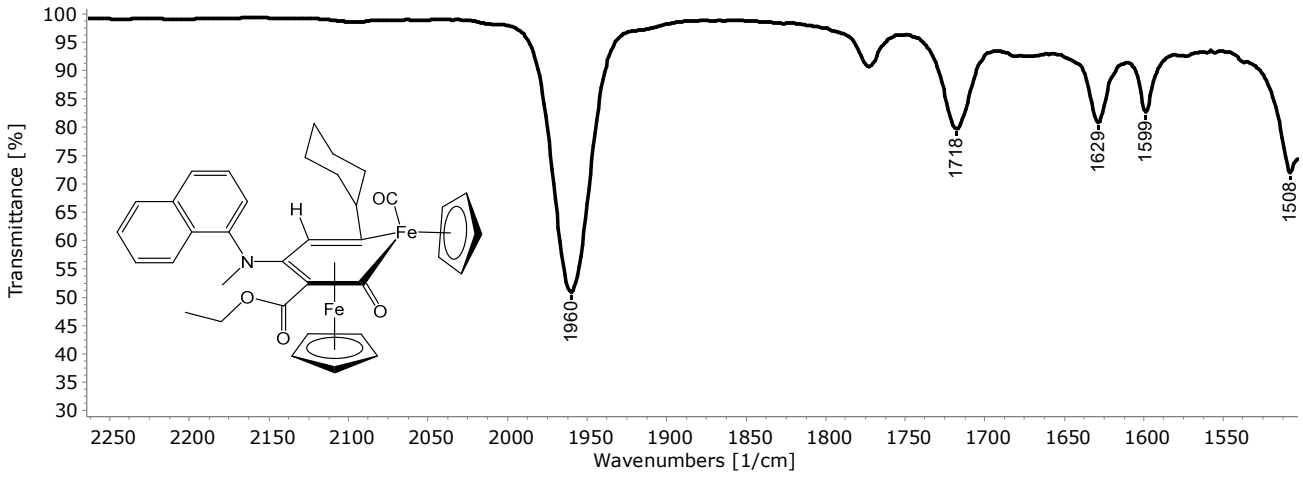

Figure S20. IR spectrum (CH_2Cl_2 solution) of **3d**

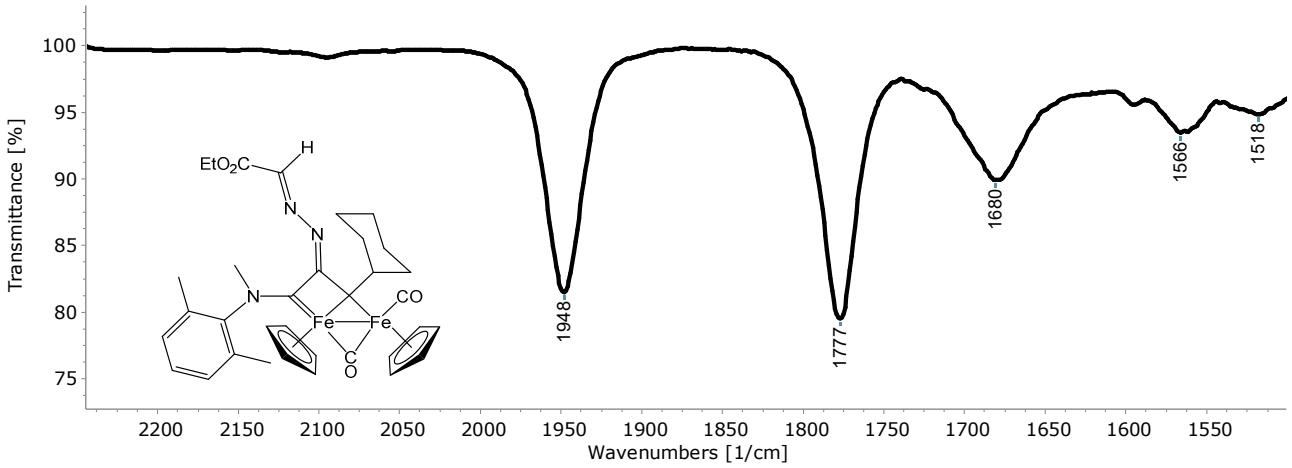

Figure S21. IR spectrum (CH_2Cl_2 solution) of **5a**

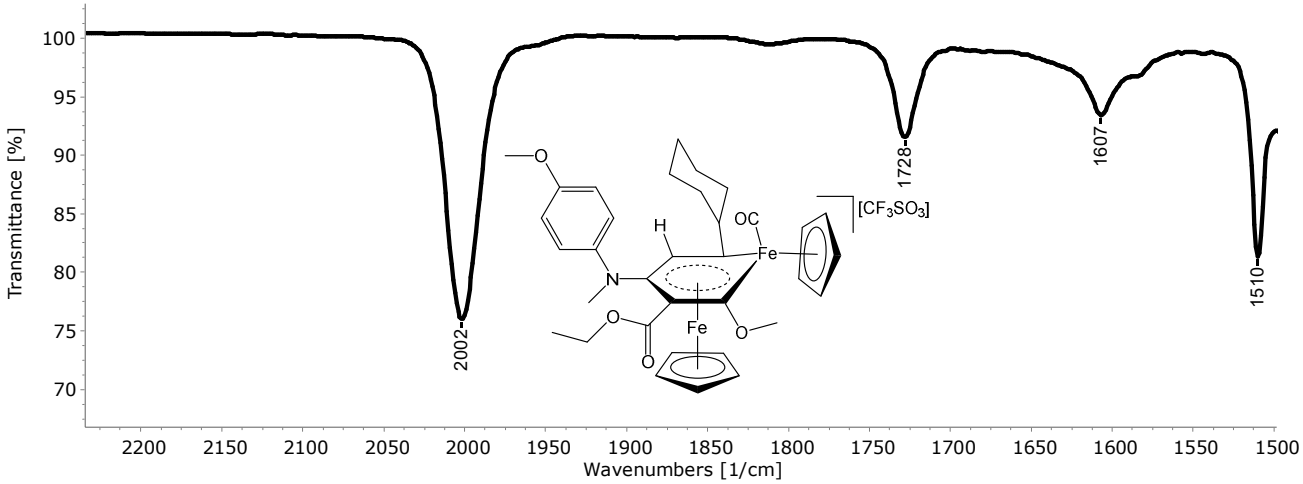

Figure S22. IR spectrum (CH_2Cl_2 solution) of **5b**.

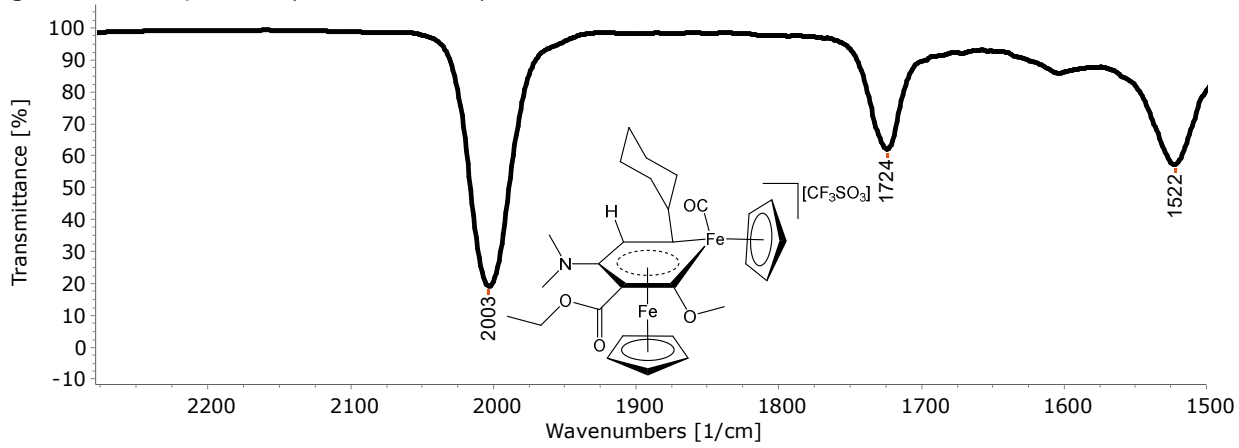

Figure S23. IR spectrum (CH_2Cl_2 solution) of **5c**

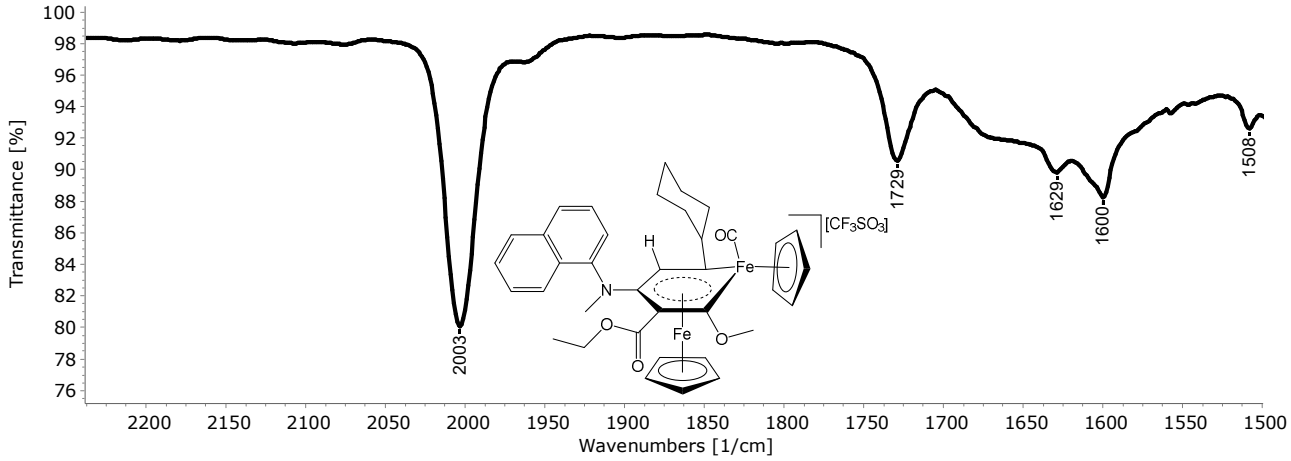

Figure S24. IR spectrum (CH_2Cl_2 solution) of **5aEt**

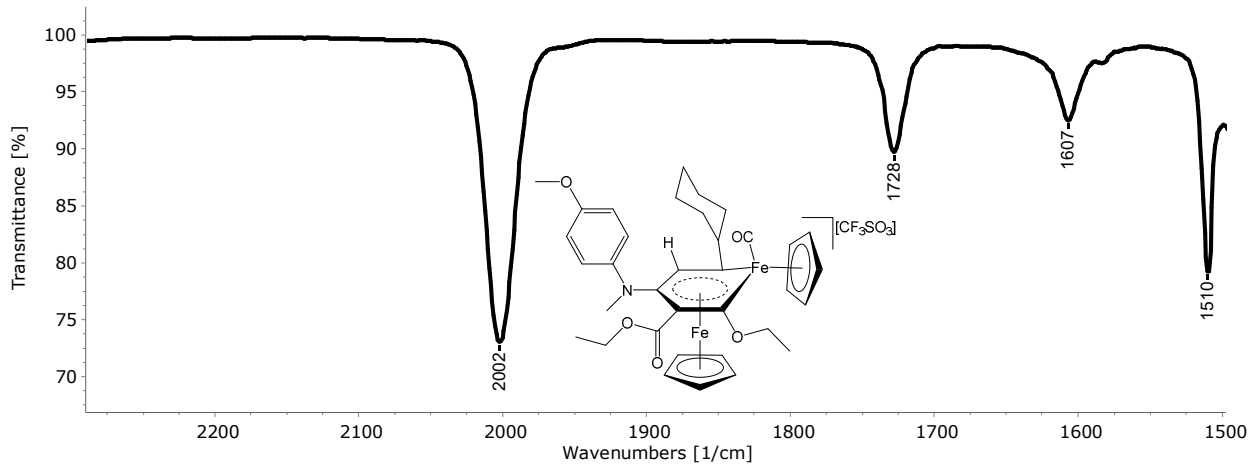

Figure S25. ^{1}H NMR spectrum (401 MHz, acetone-d_6) of **2b**

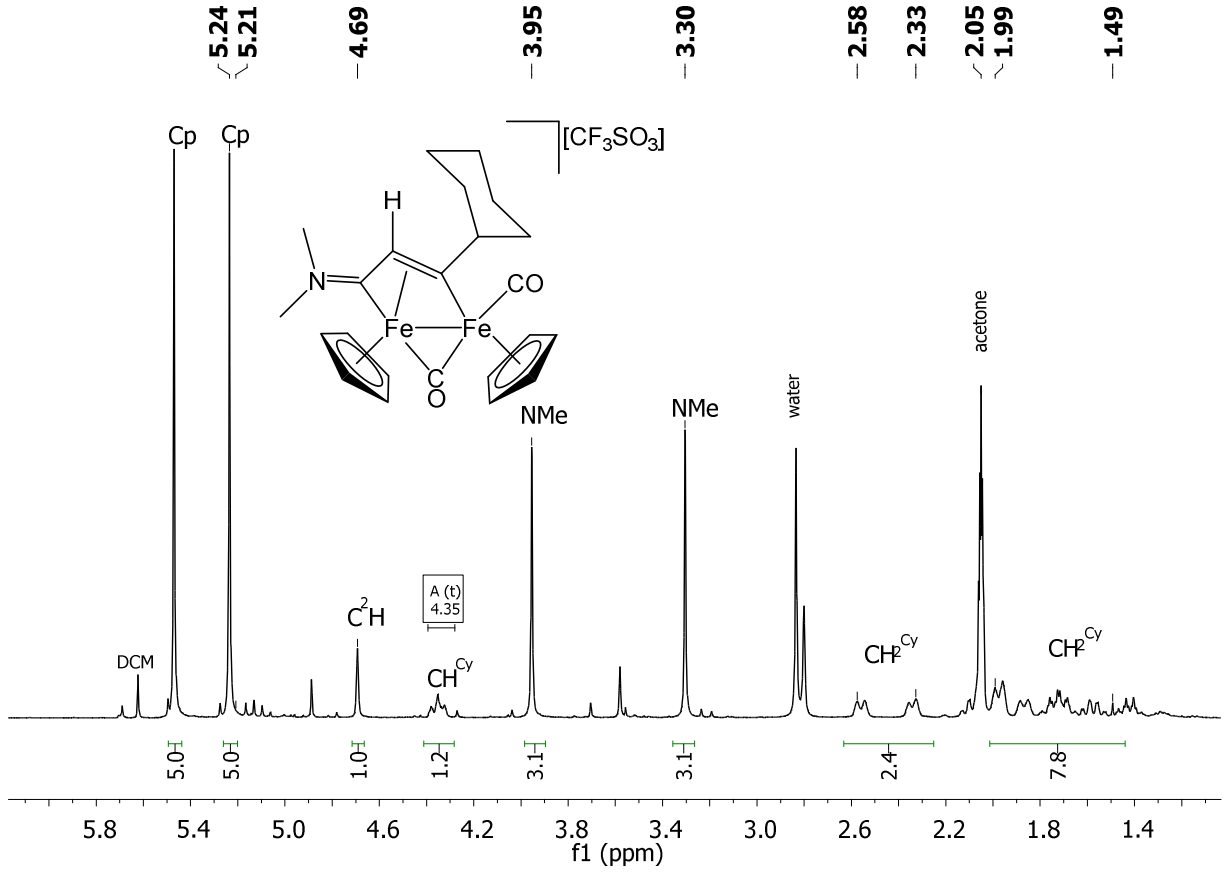

Figure S26. $^{13}C\{^{1}H\}$ NMR spectrum (101 MHz, acetone-d_6) of **2b**

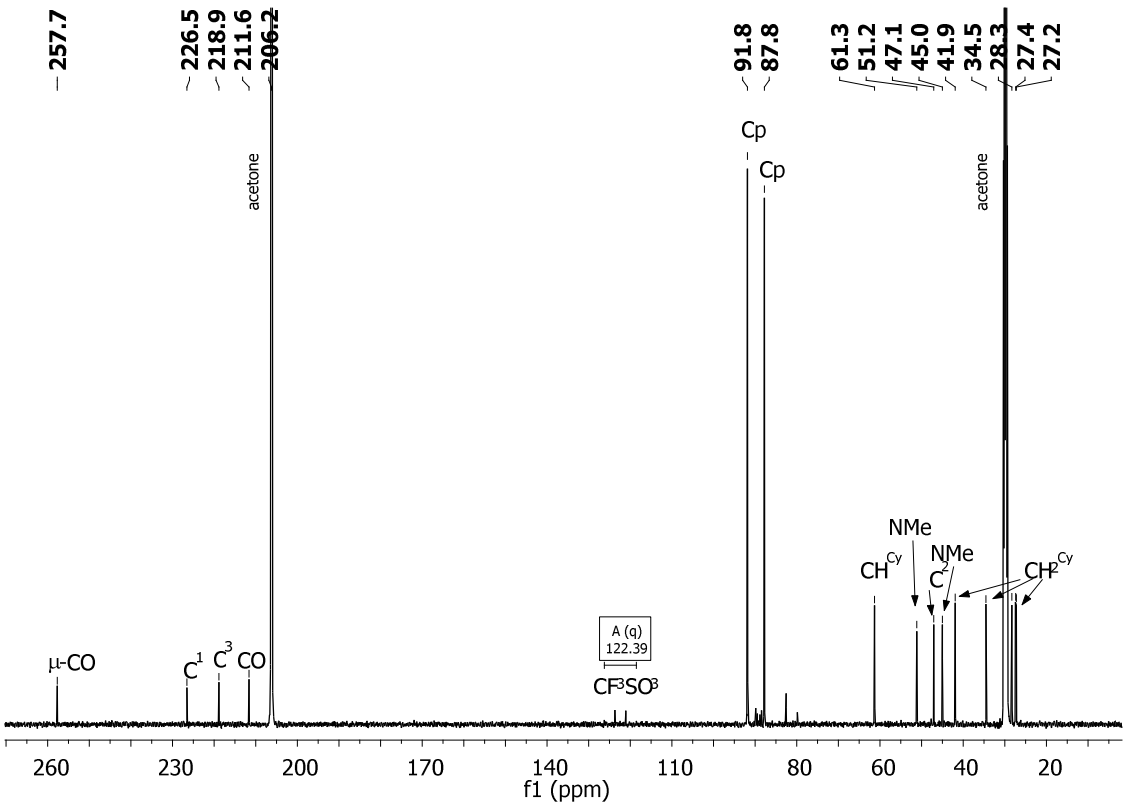

Figure S27. ^{1}H NMR spectrum (401 MHz, acetone-d_6) of **2c** (E and Z isomers)

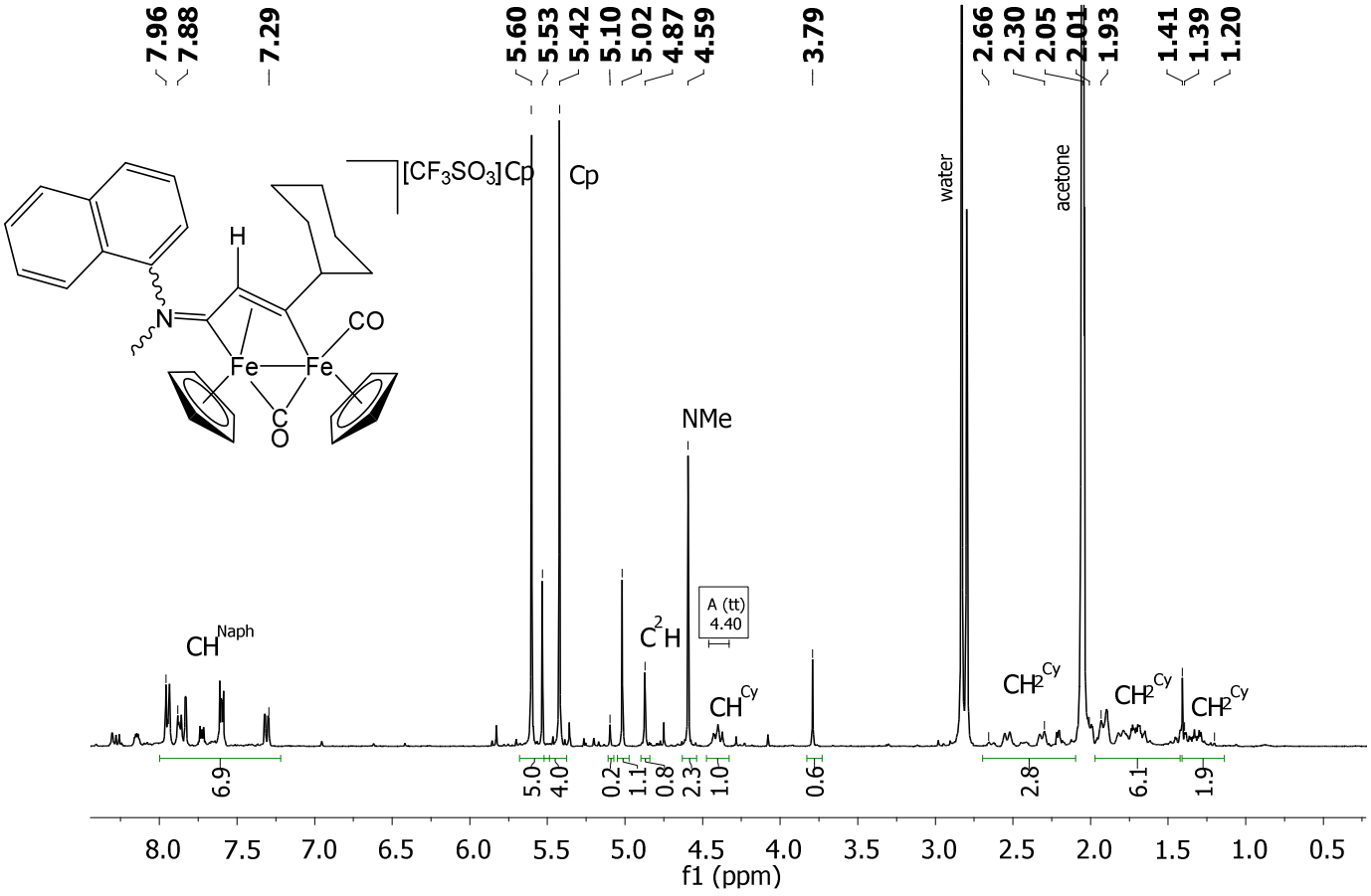

Figure S28. $^{13}C\{^{1}H\}$ NMR spectrum (101 MHz, acetone-d_6) of **2c**

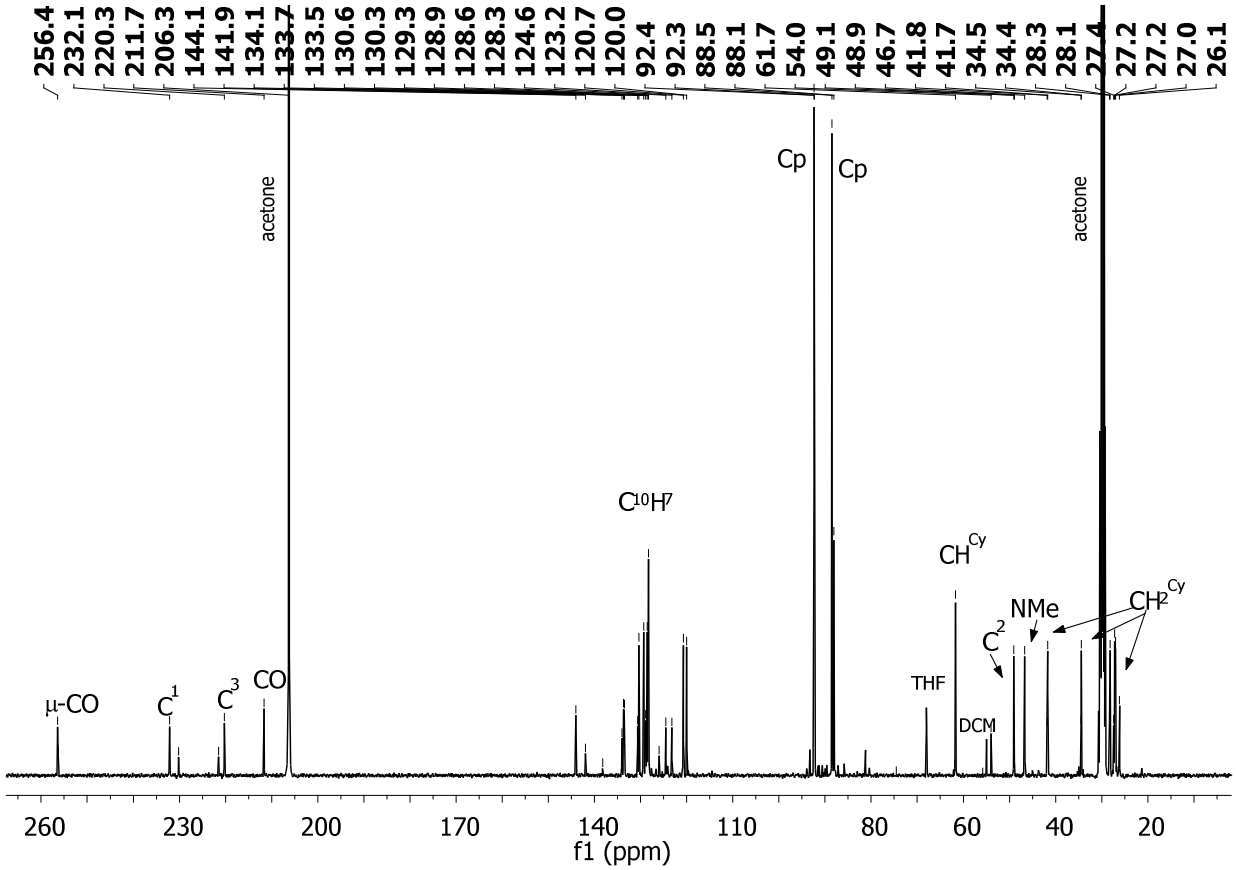

Figure S29. ^{1}H NMR spectrum (401 MHz, acetone-d_6) of **2d**

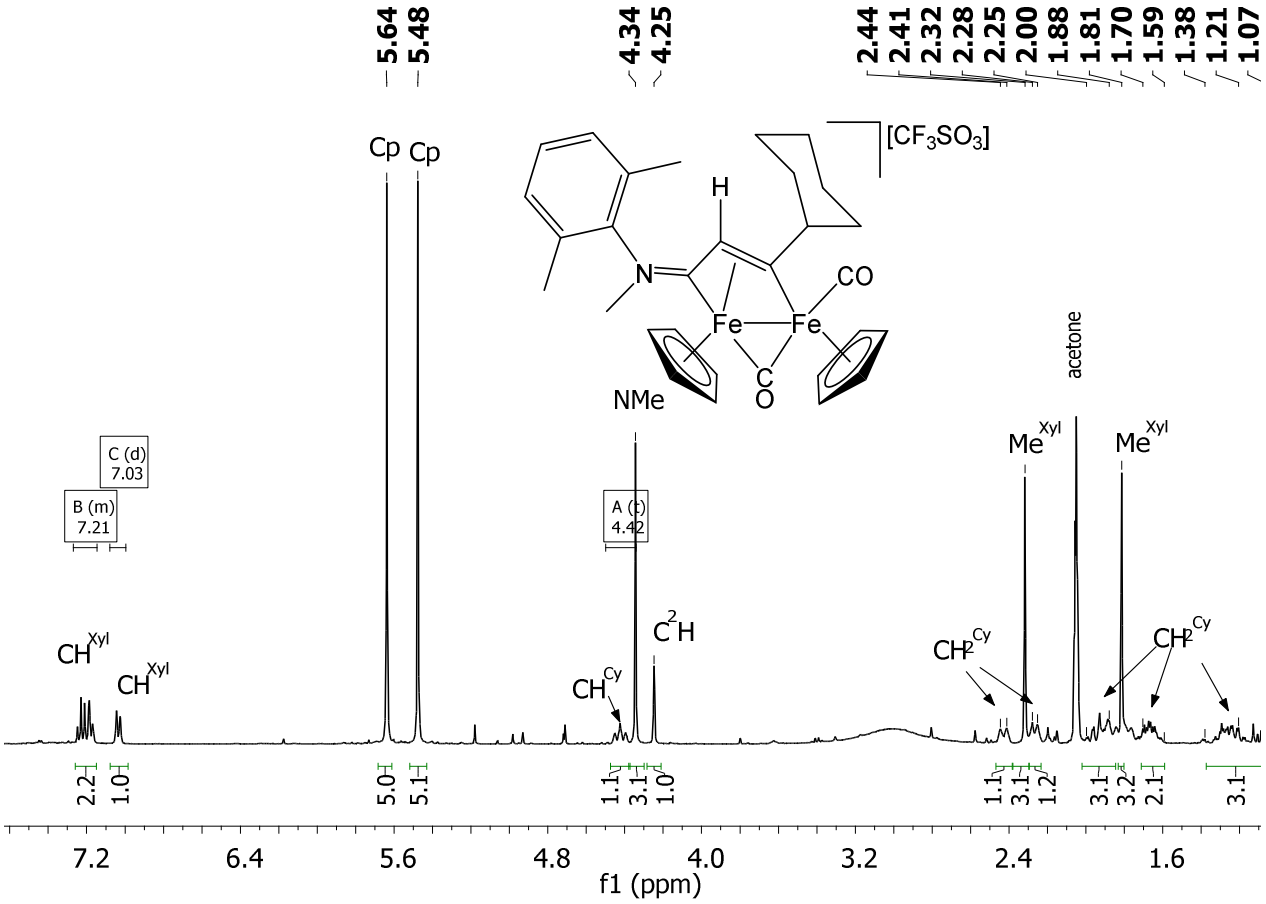

Figure S30. ^{13}C{^{1}H} NMR spectrum (101 MHz, acetone-d_6) of **2d**

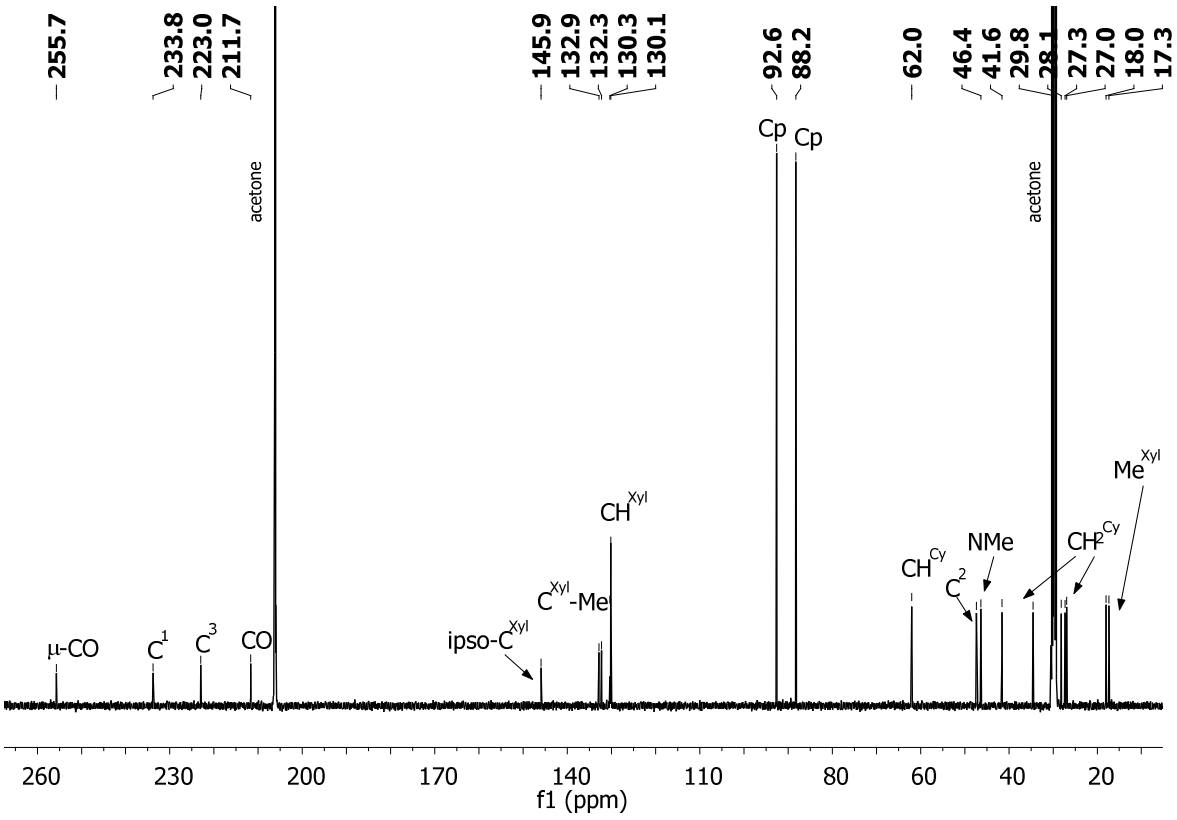

Figure S31. ^{1}H NMR spectrum (401 MHz, acetone-d_6) of **2a^{D}** (*E* and *Z* isomers)

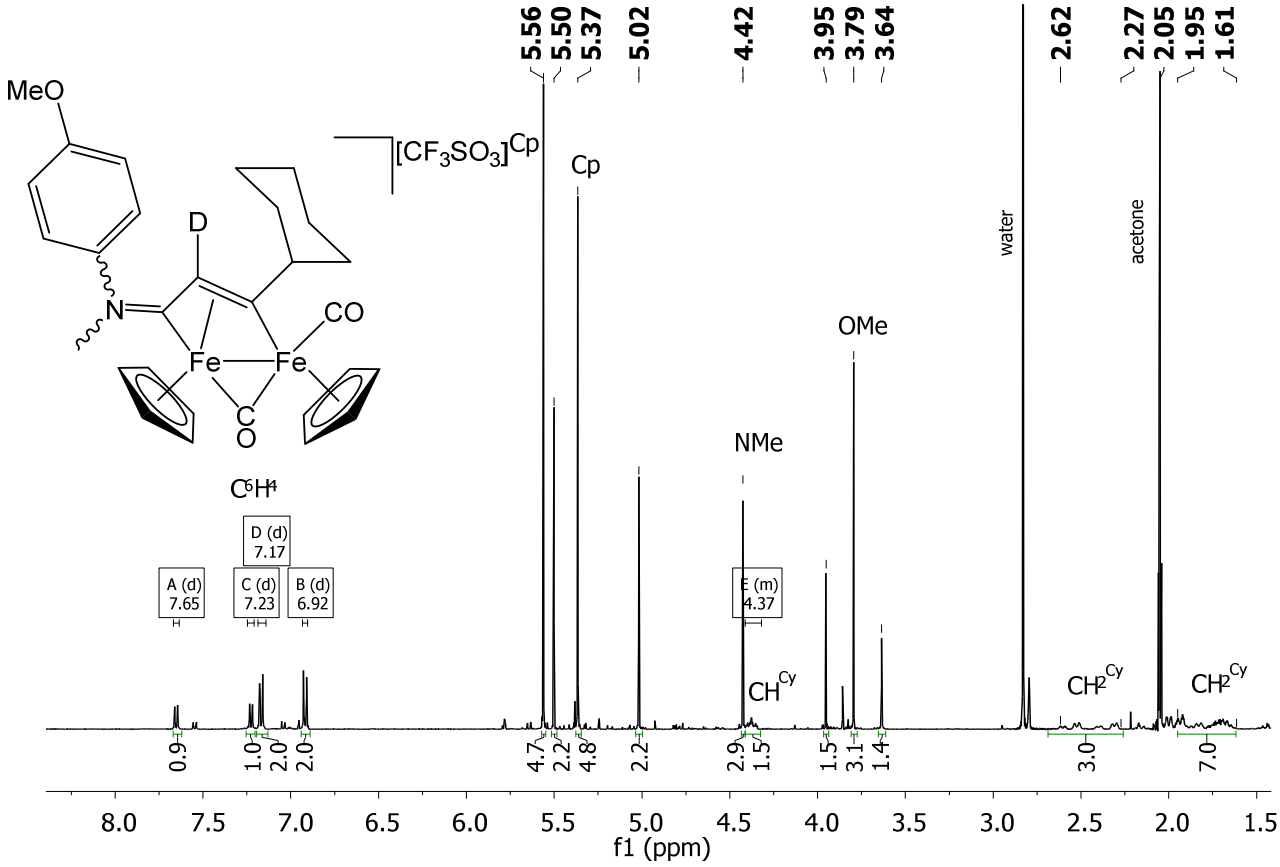

Figure S32. ^{1}H NMR spectrum (401 MHz, acetone-d_6) of **4a**

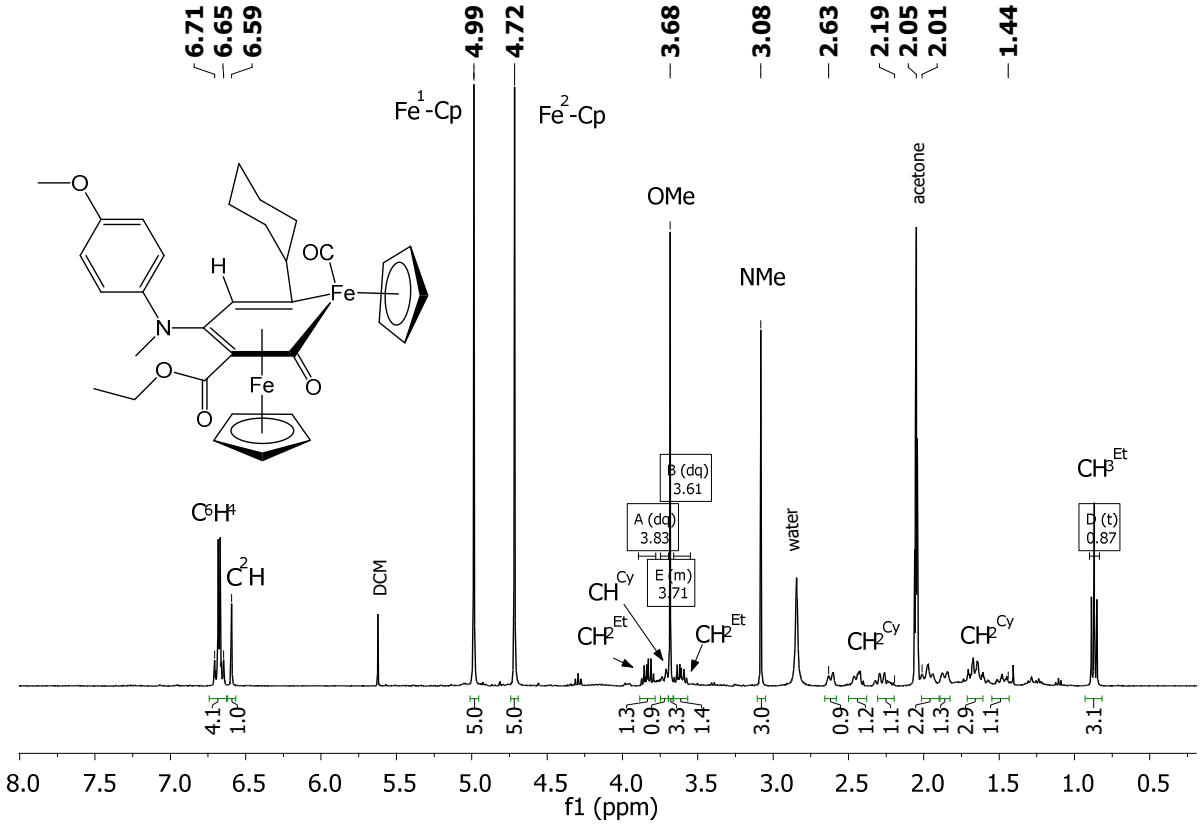

Figure S33. ^{13}C{^{1}H} NMR spectrum (101 MHz, acetone-d_6) of **4a**

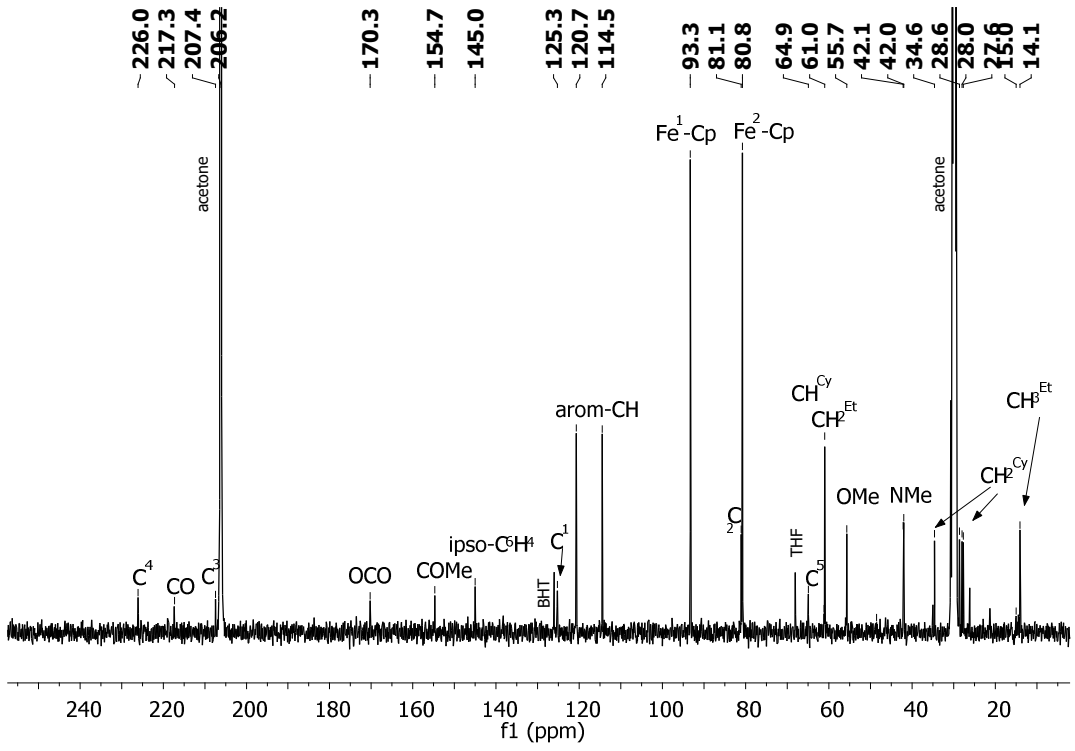

Figure S34. ^{1}H NMR spectrum (401 MHz, acetone-d_6) of **4b**

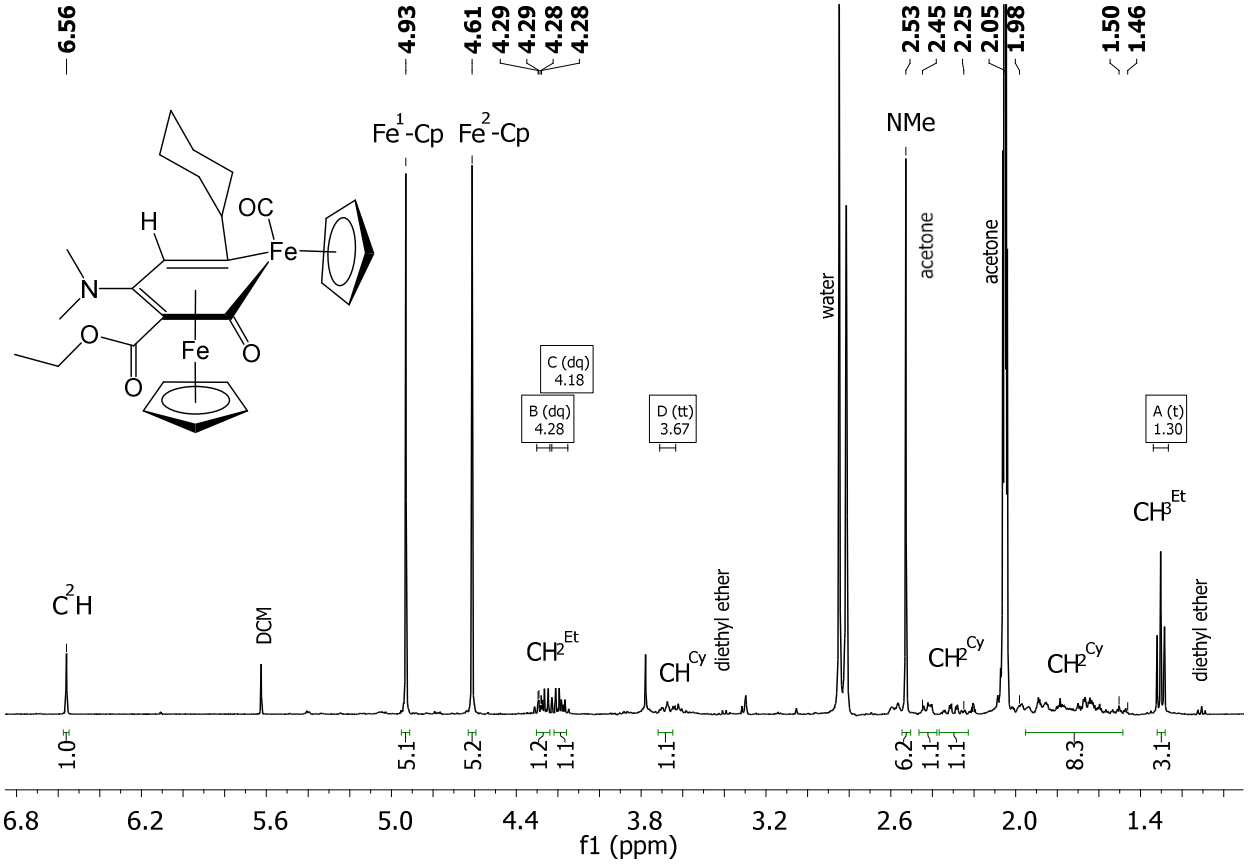

Figure S35. ^{13}C{^{1}H} NMR spectrum (101 MHz, acetone-d_6) of **4b**

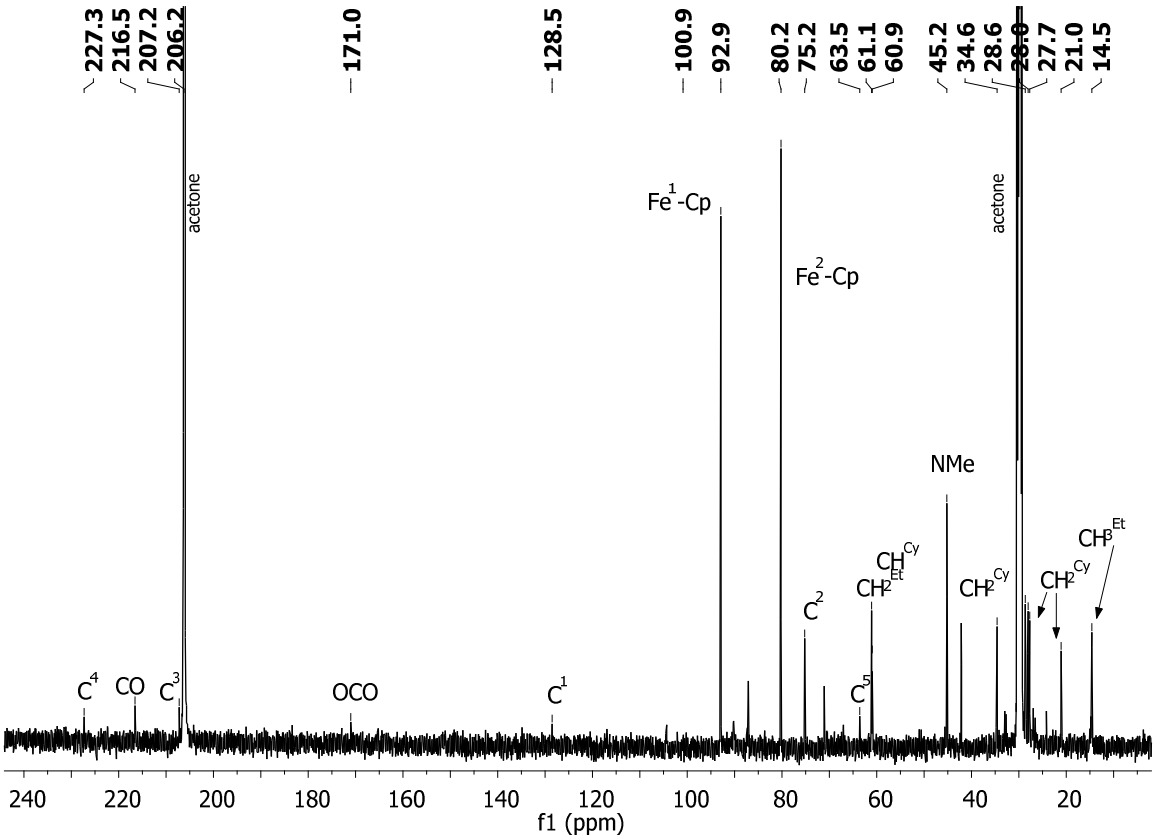

Figure S36. ^{1}H NMR spectrum (401 MHz, acetone-d_6) of **4c**

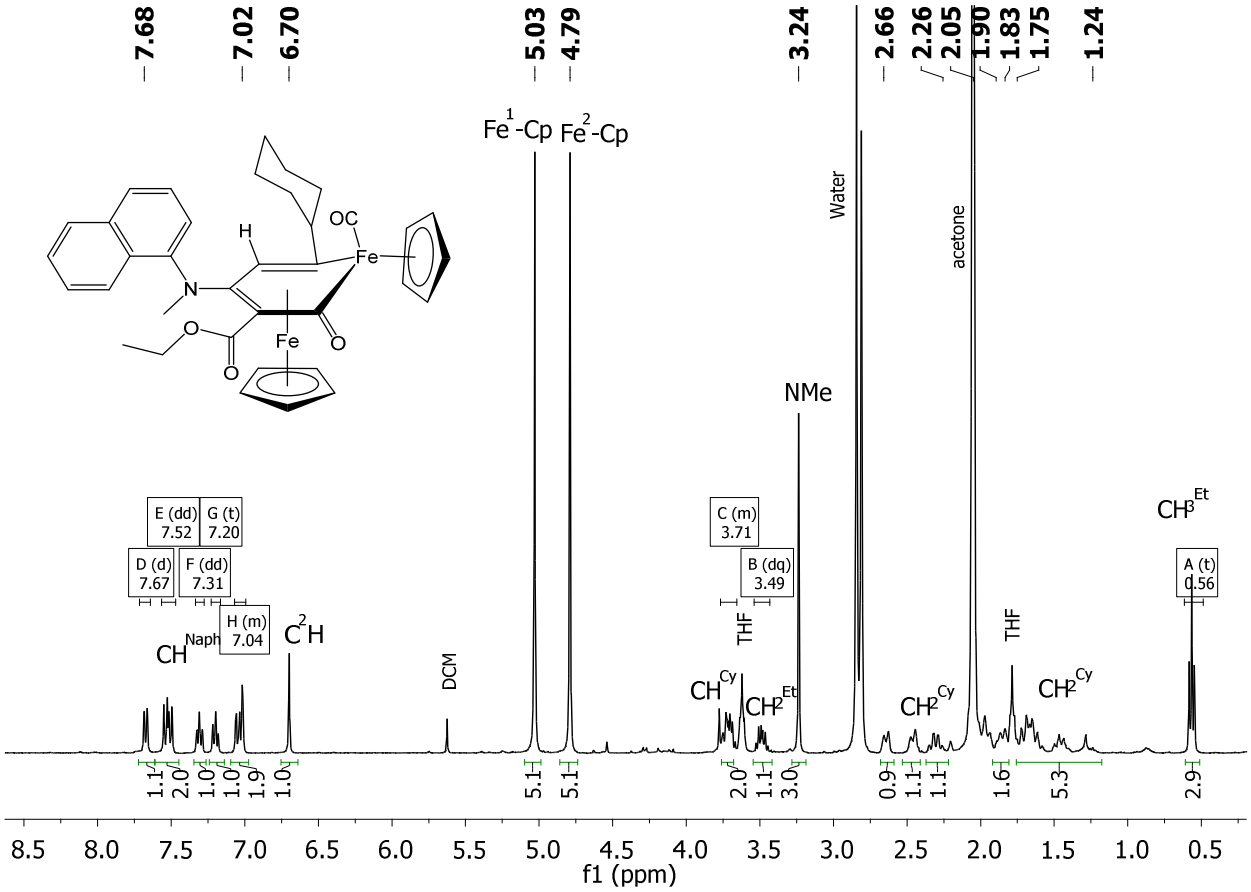

Figure S37. $^{13}C\{^{1}H\}$ NMR spectrum (101 MHz, acetone-d_6) of **4c**

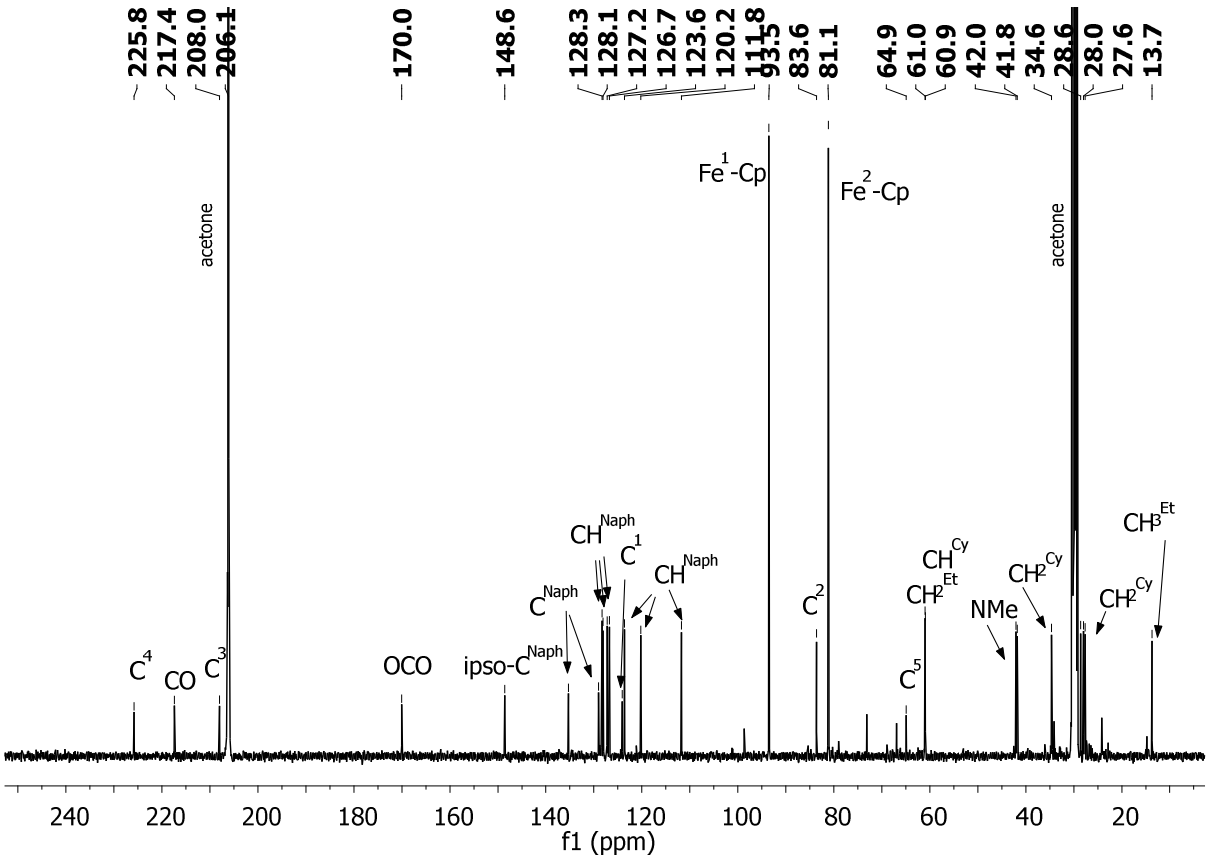

Figure S38. ^{1}H NMR spectrum (401 MHz, $CDCl_3$) of **3d**

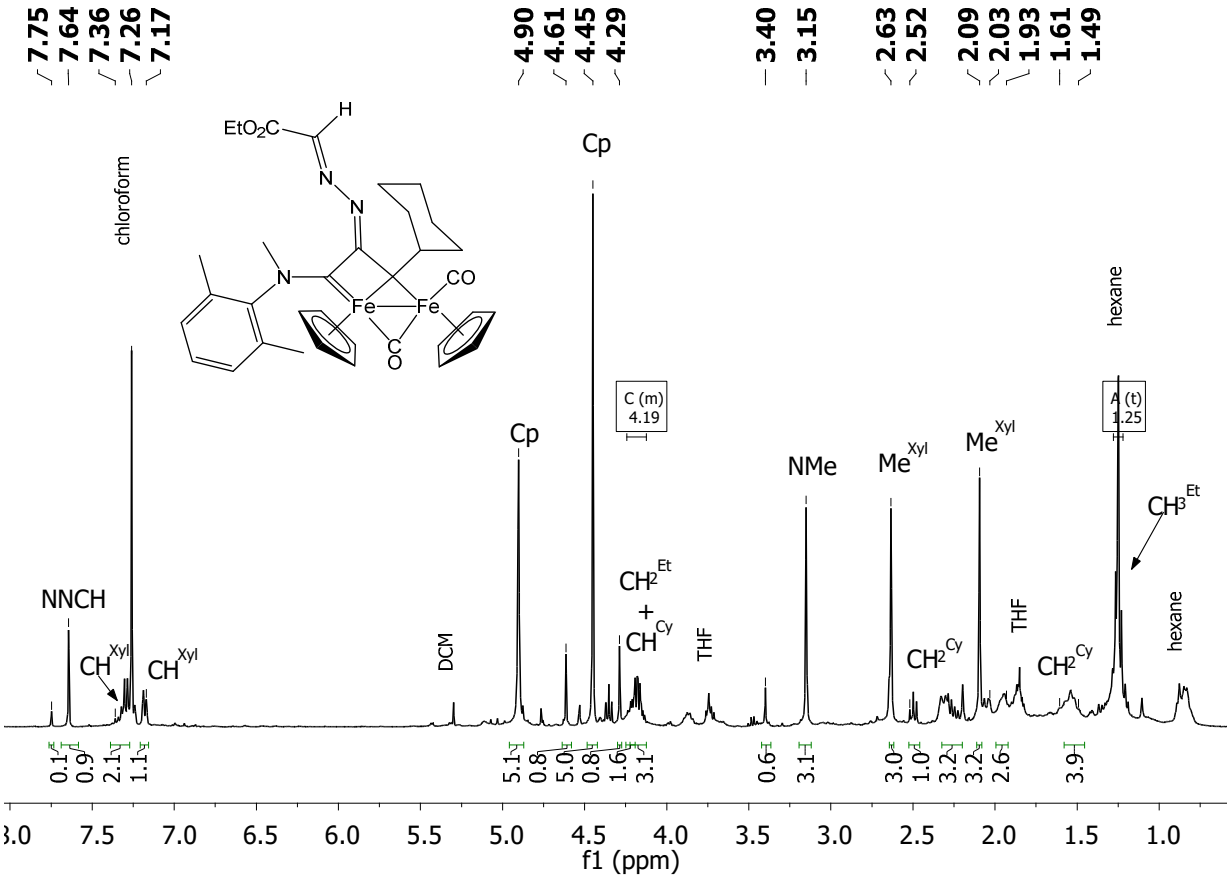

Figure S39. $^{13}C\{^{1}H\}$ NMR spectrum (101 MHz, $CDCl_3$) of **3d**

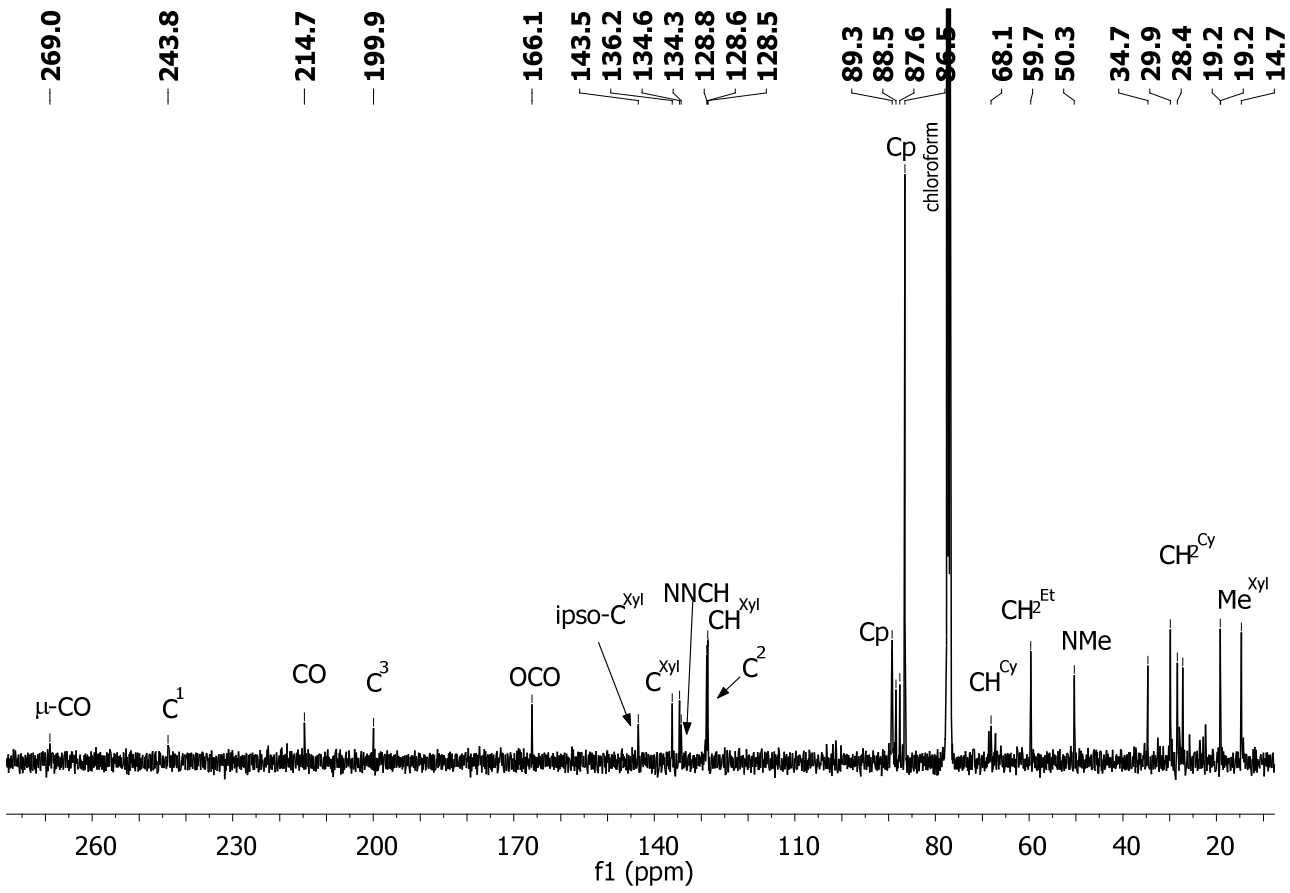

Figure S40. ^{1}H NMR spectrum (401 MHz, acetone-d_6) of **5a**

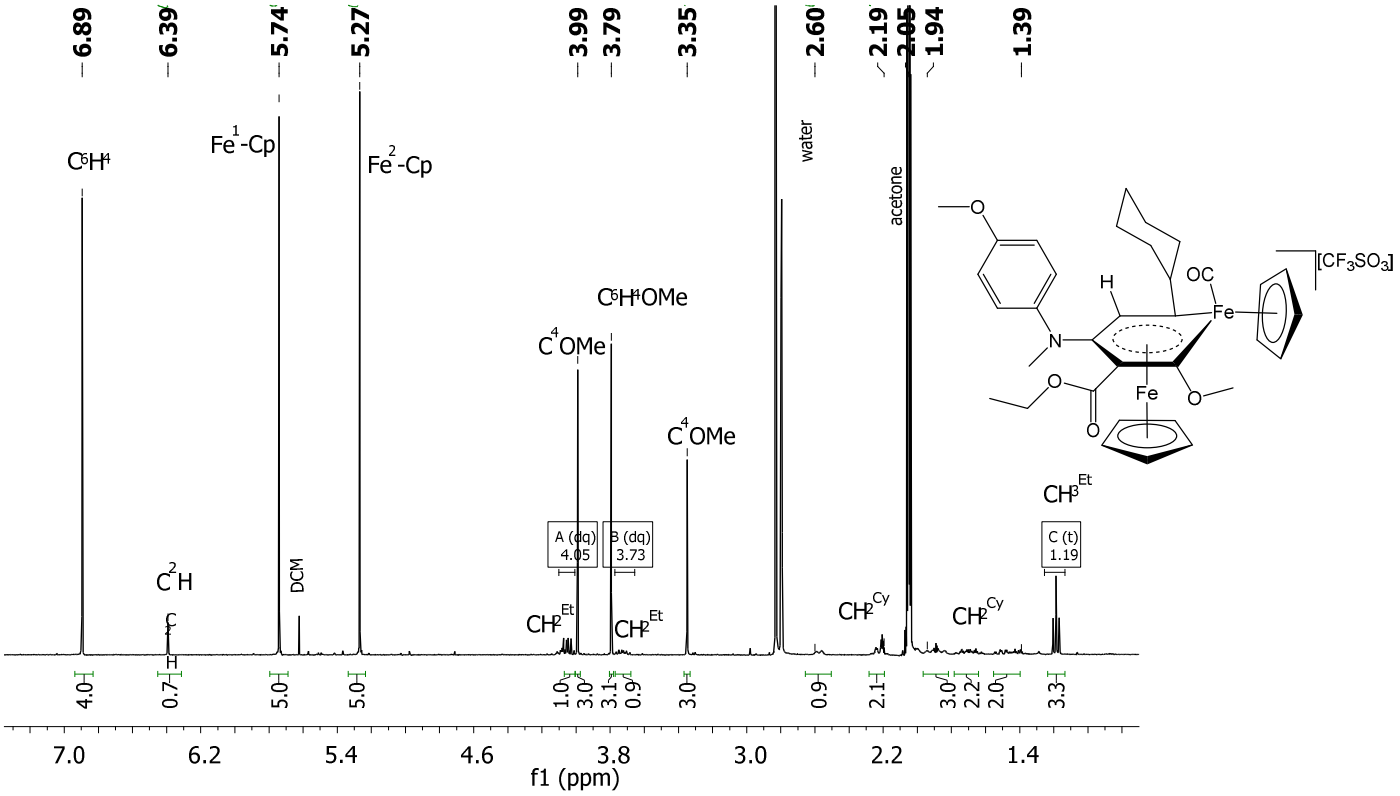

Figure S41. ^{13}C{^{1}H} NMR spectrum (101 MHz, acetone-d_6) of **5a**

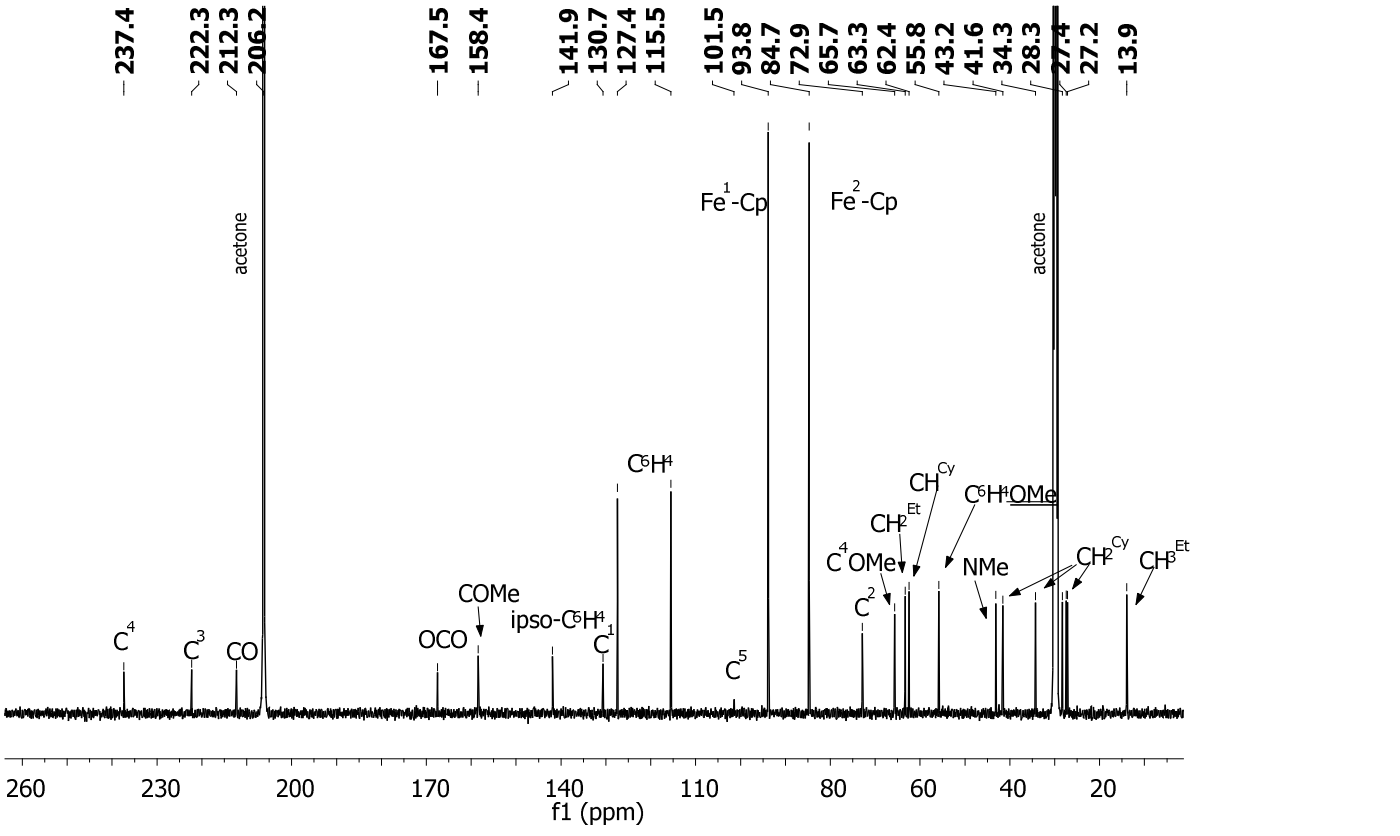

Figure S42. ^{1}H NMR spectrum (401 MHz, acetone-d_6) of **5b**

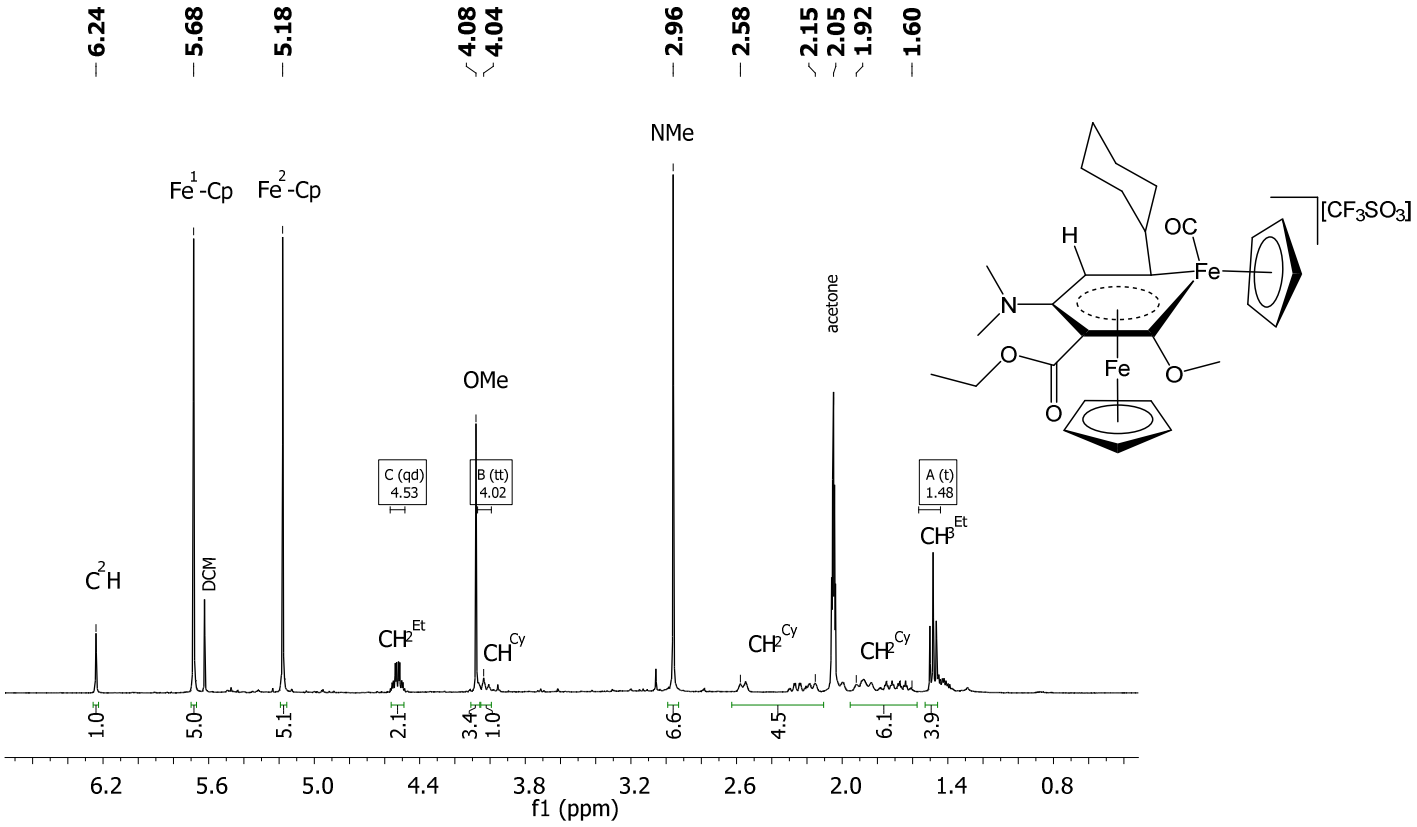

Figure S43. ^{13}C{^{1}H} NMR spectrum (101 MHz, acetone-d_6) of **5b**

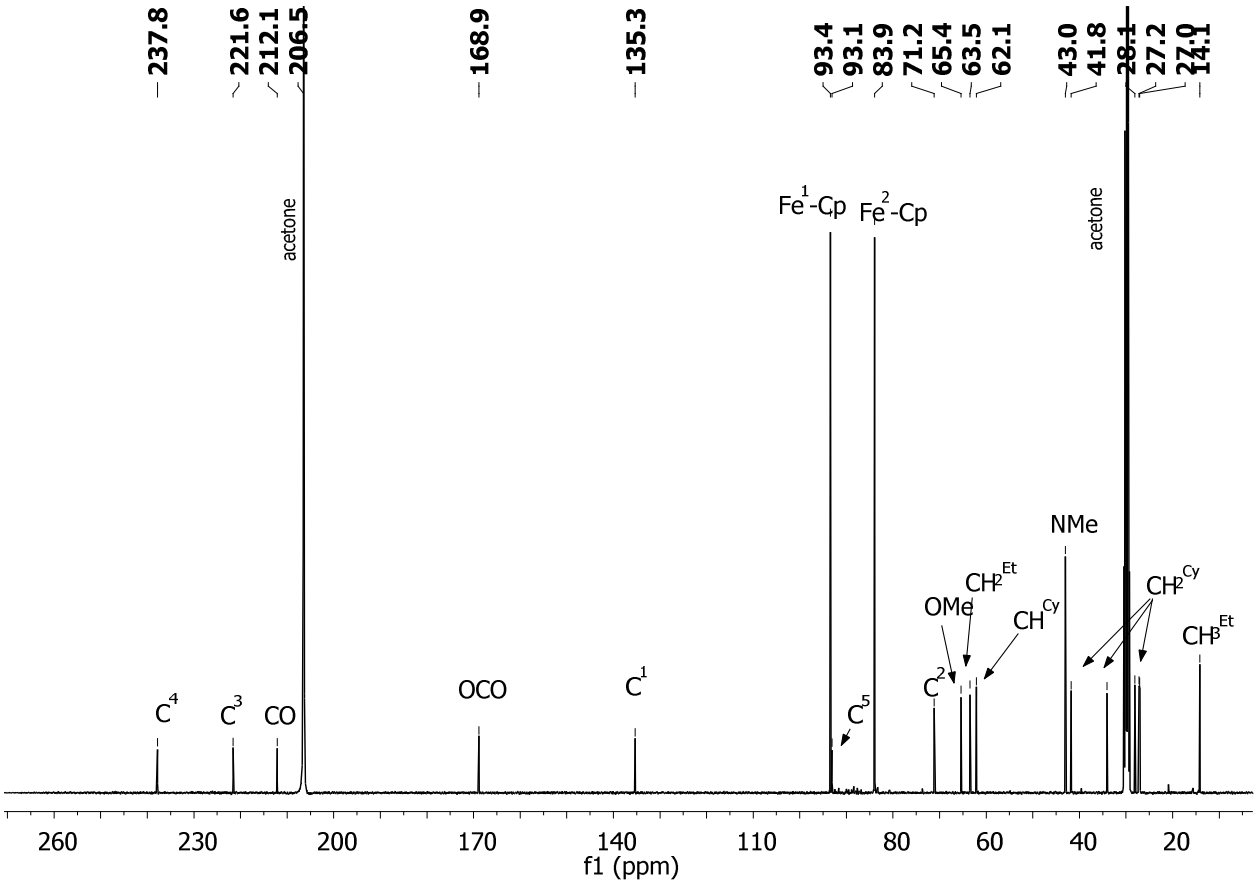

Figure S44. ^{1}H NMR spectrum (401 MHz, acetone-d_6) of **5c**

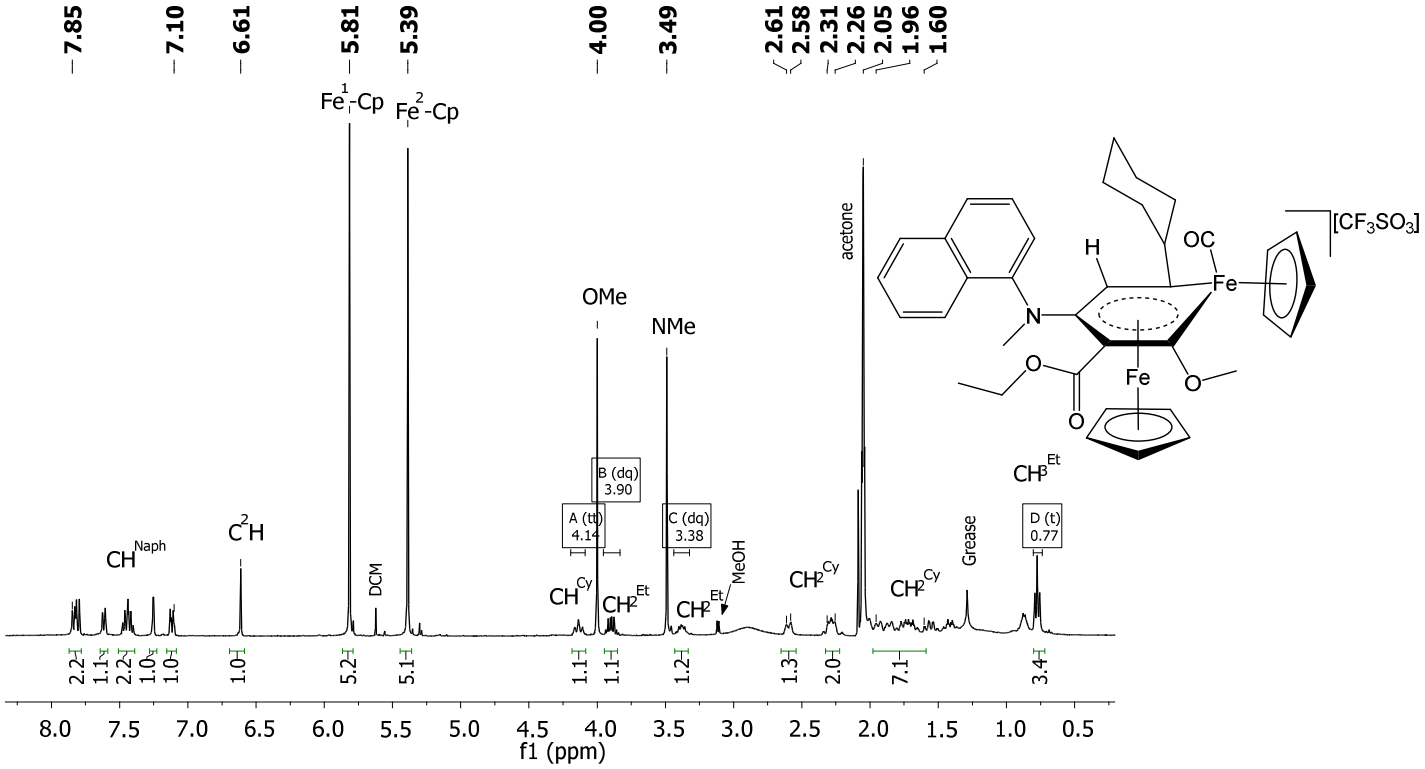

Figure S45. ^{13}C{^{1}H} NMR spectrum (101 MHz, acetone-d_6) of **5c**

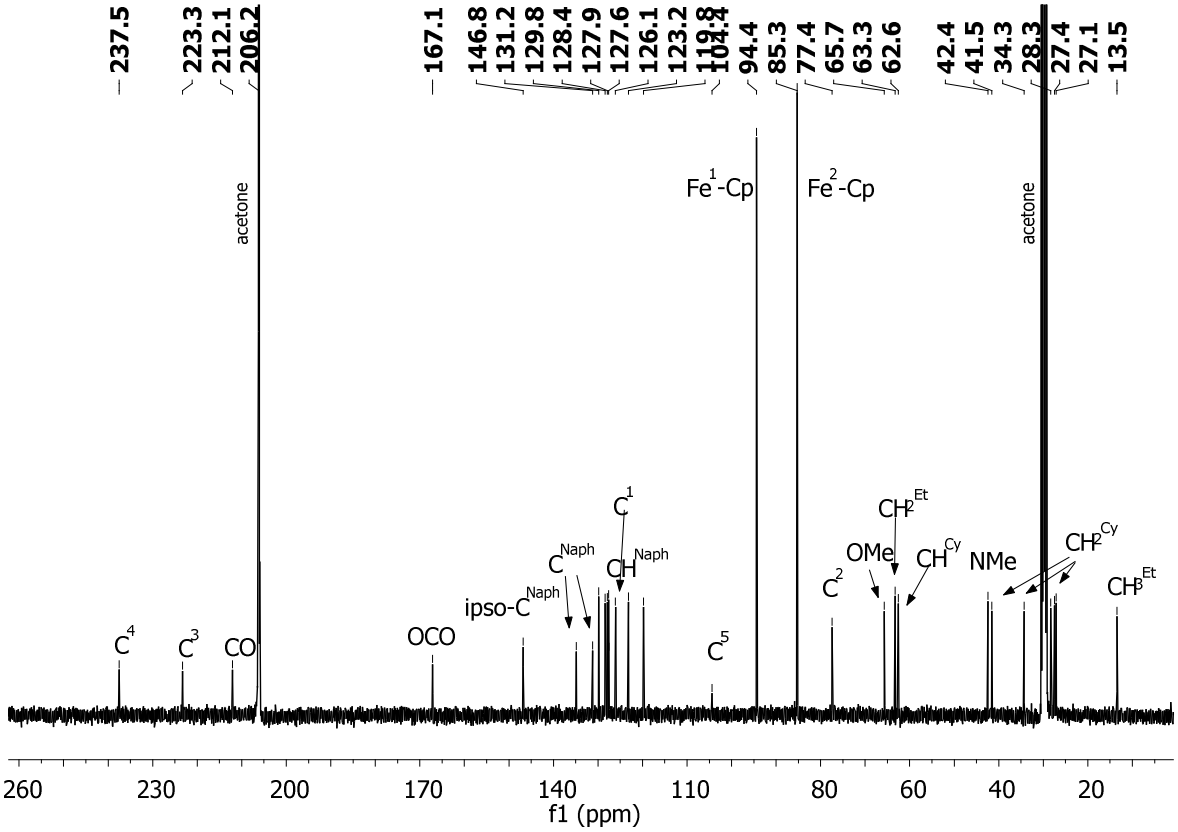

Figure S46. ^{1}H NMR spectrum (401 MHz, acetone-d_6) of **5aEt**

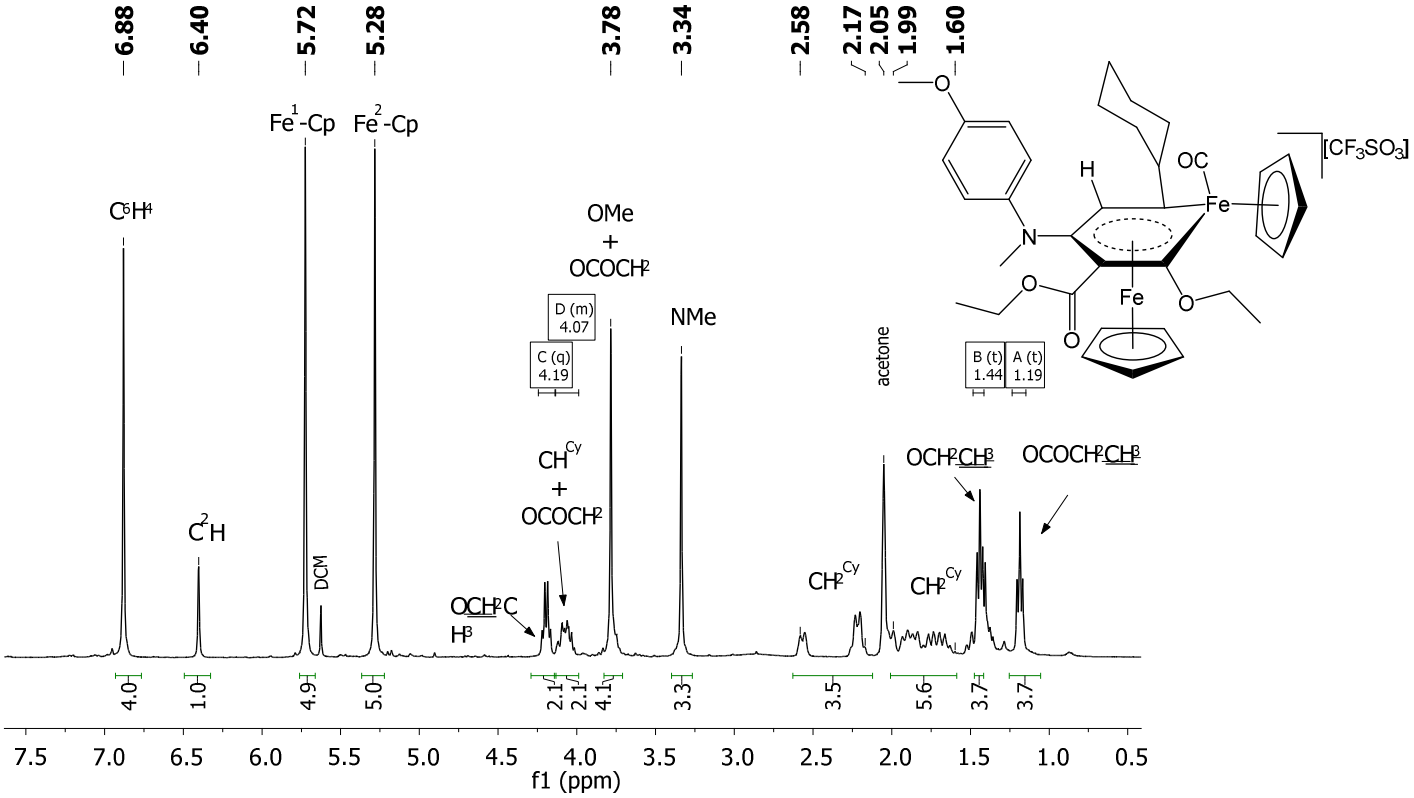

Figure S47. ^{13}C{^{1}H} NMR spectrum (101 MHz, acetone-d_6) of **5aEt**

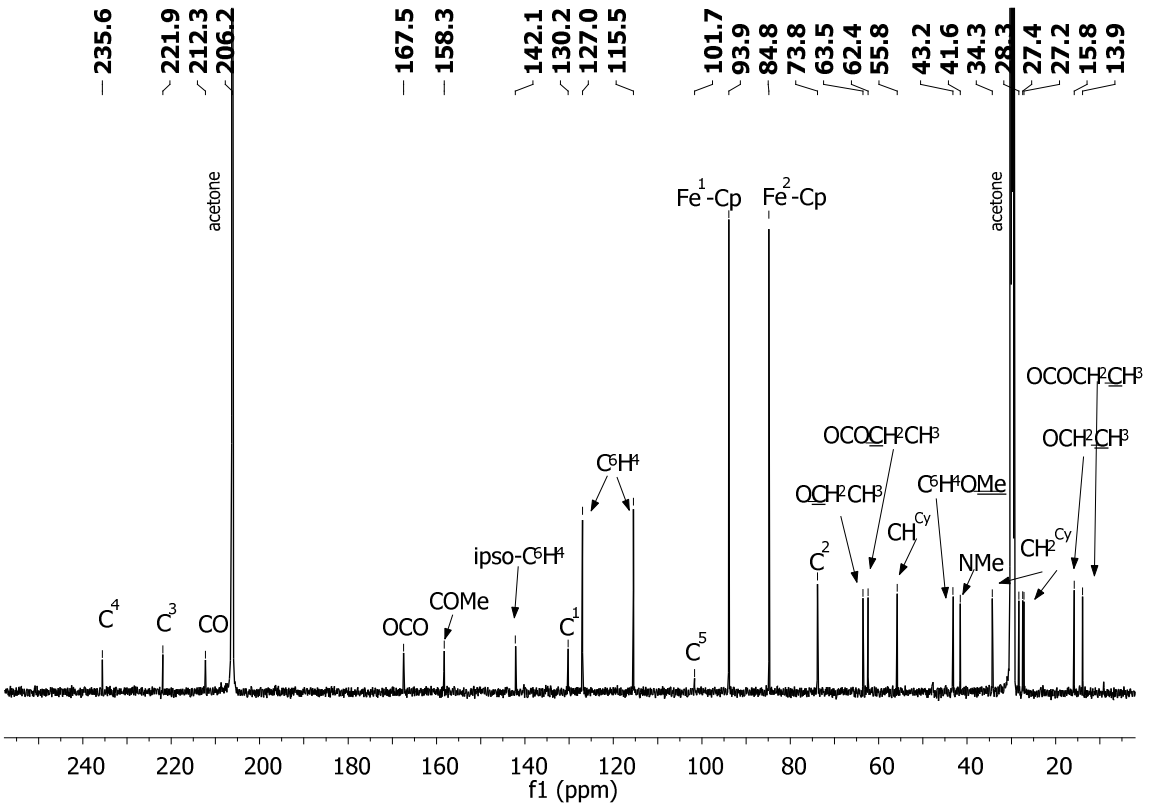

Figure S48. ^{1}H NMR spectrum (401 MHz, acetone-d_6) of **5a** as prepared from **2a^{D}**

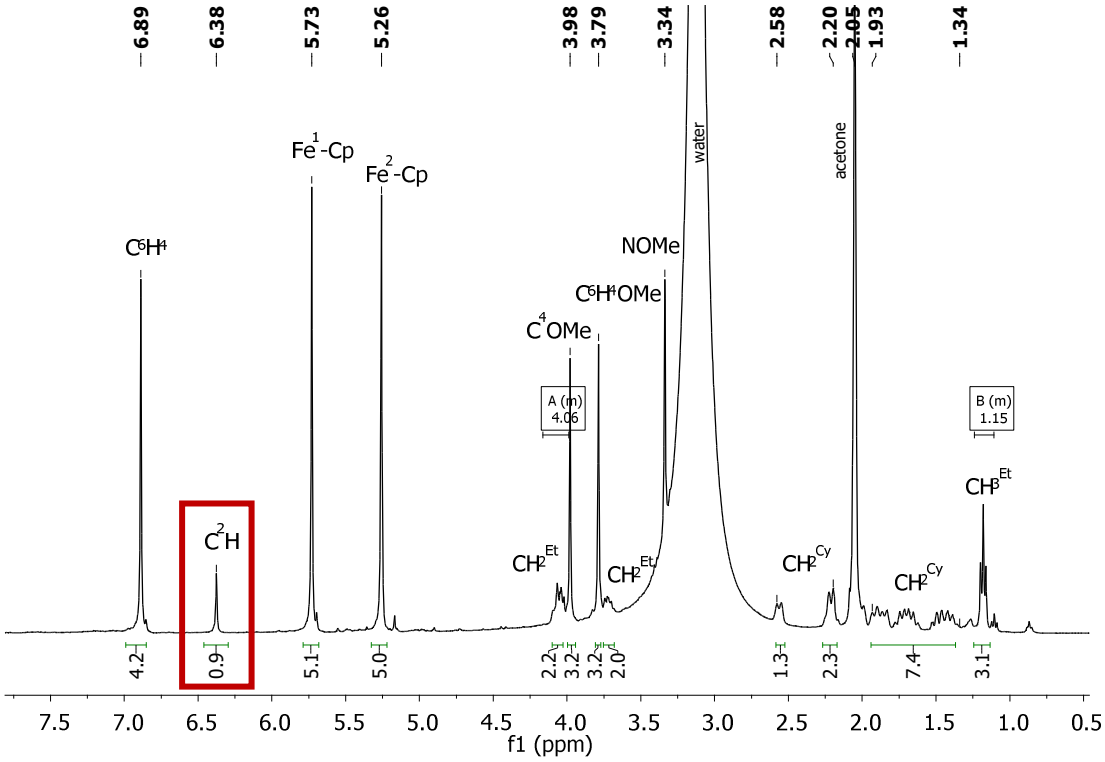

Figure S49. ESI-MS spectrum of **3d**

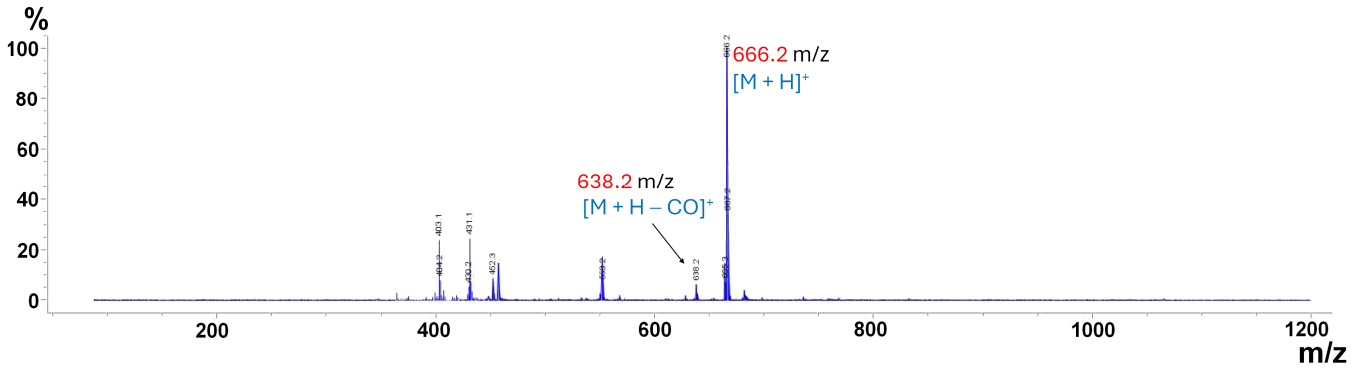

Figure S50. ESI-MS spectrum of **4a**

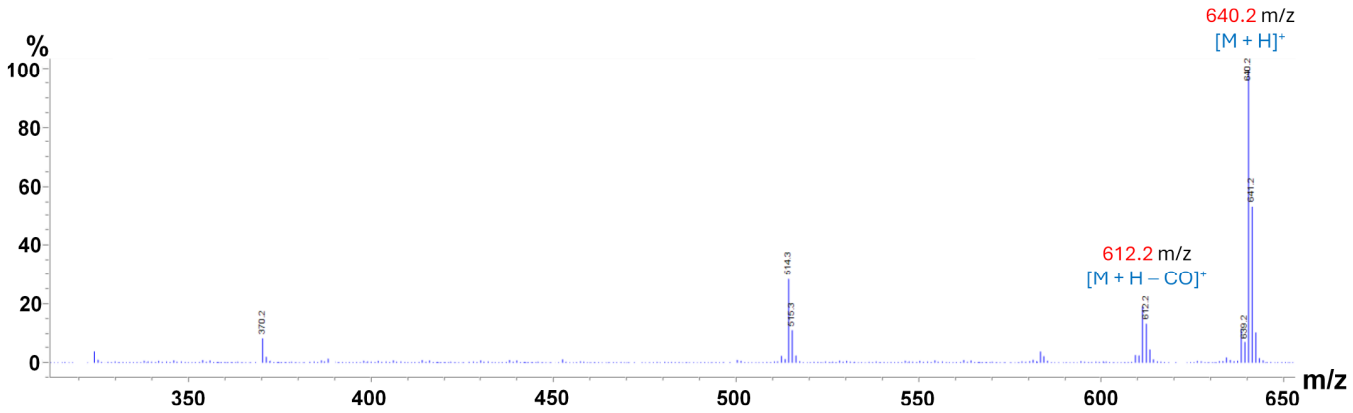

Figure S51. ESI-MS spectrum of **4b**

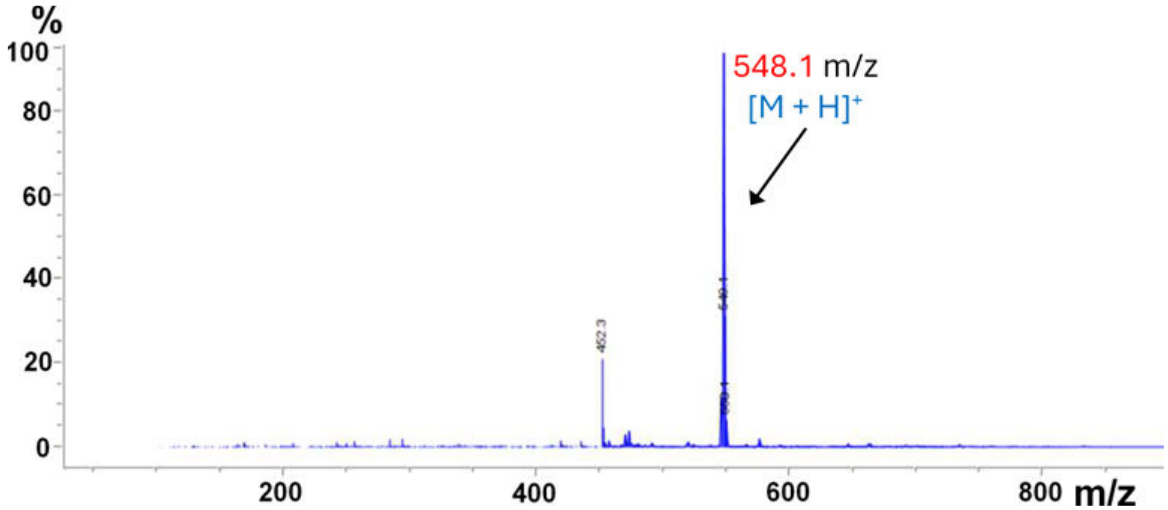

Figure S52. ESI-MS spectrum of **4c**

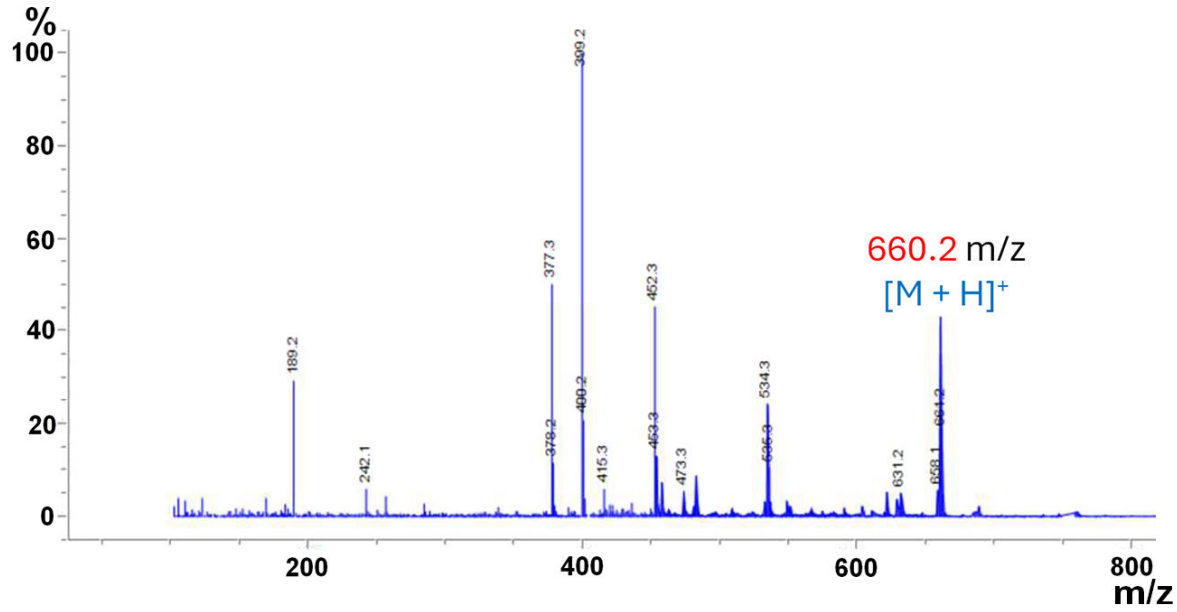

Figure S53. ESI-MS spectrum of **5a**

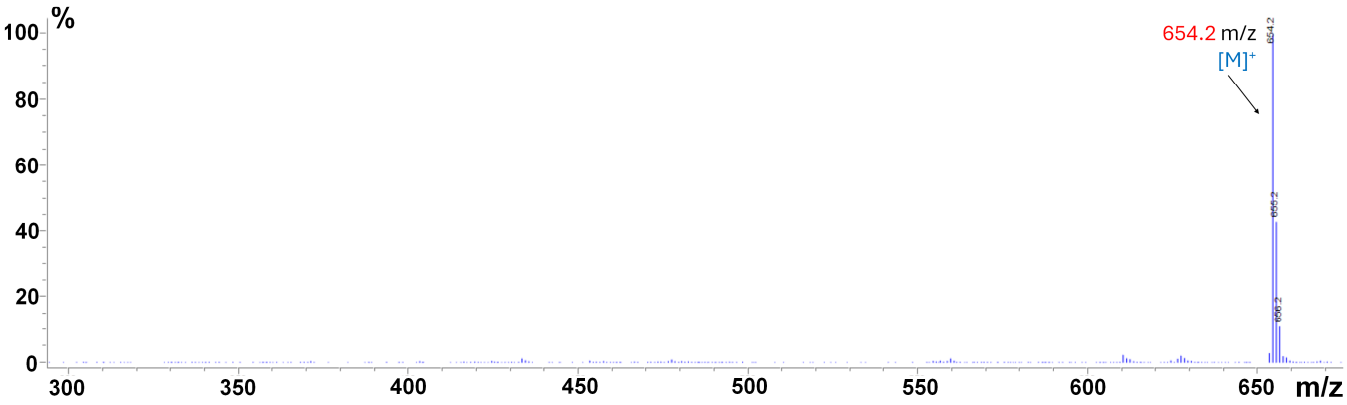

Figure S54. ESI-MS spectrum of **5b**

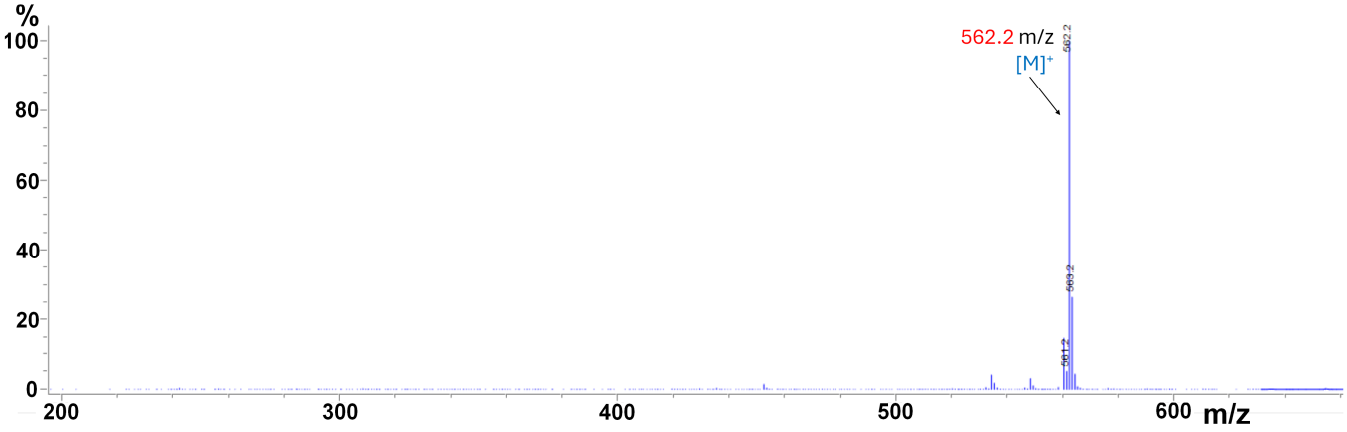

Figure S55. ESI-MS spectrum of **5c**

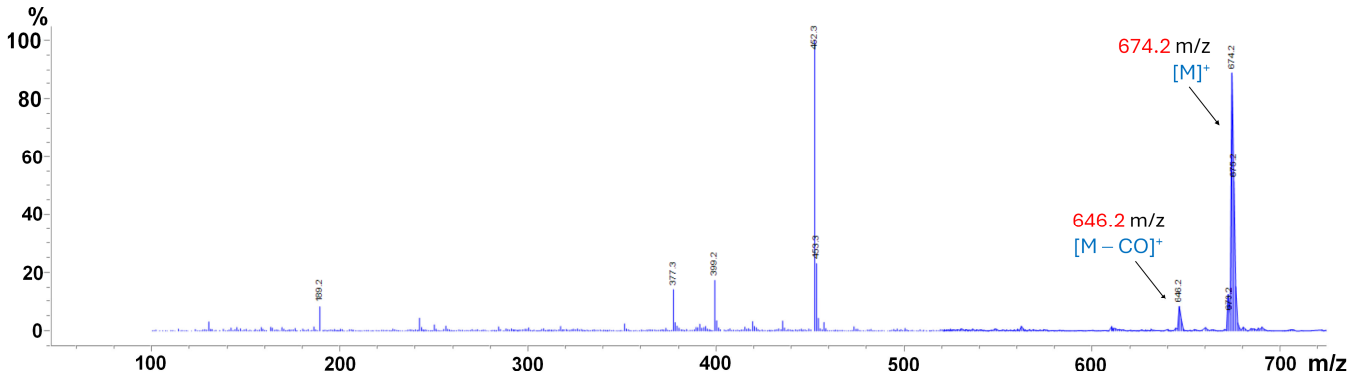

Figure S56. ESI-MS spectrum of **5aEt**

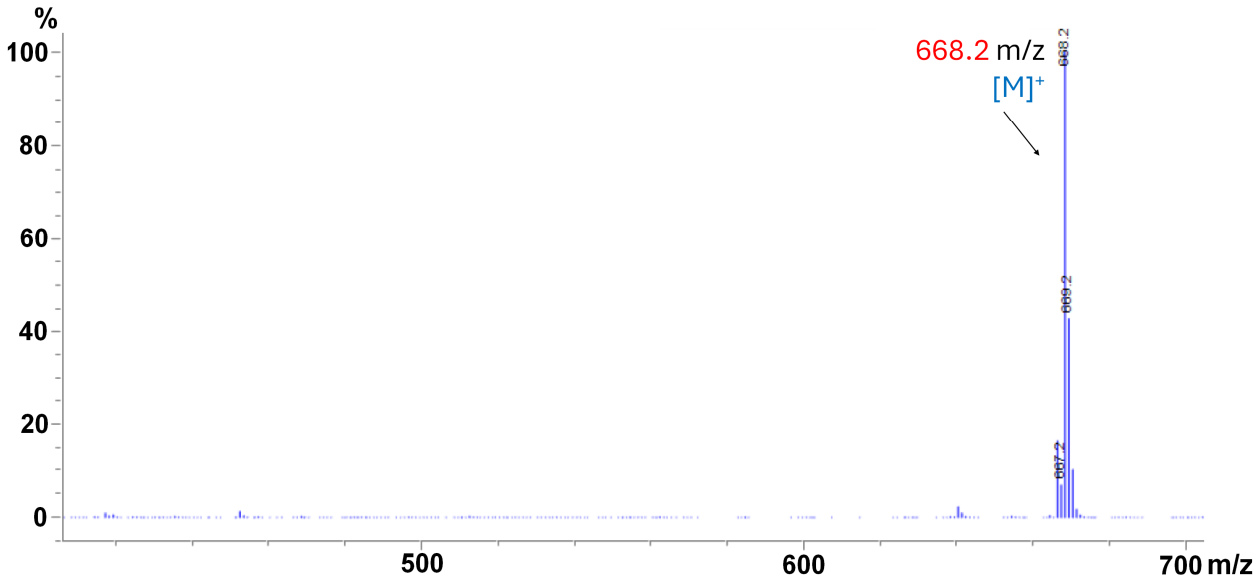

3. Computational studies

3.1. Computational details

Density functional theory (DFT) calculations were performed with the Gaussian 16 (rev A03) quantum-chemical software. The Becke's three parameters hybrid exchange-correlation functional (B3LYP) was used in conjunction with the def2-TZVP basis set for all calculations. Solvation effects were considered exploiting the polarizable continuum model (PCM). Moreover, Grimme's D3 dispersion correction was included using the Becke-Johnson damping scheme. Complete active space self-consistent field (CASSCF) calculations were carried out using the CFOUR suite of programs. The basis set used was the def2-SVP, and all calculations were performed in vacuo. The active space was selected according to the unrestricted natural orbital (UNO) procedure.

All molecular properties and parameters investigated in this work were computed on top of the optimized geometry obtained at the same level of theory.

Figure S57. Mercury views of the optimized structures of **4a** (left) and **5aEt** (right), in THF; H atoms have been omitted for clarity.

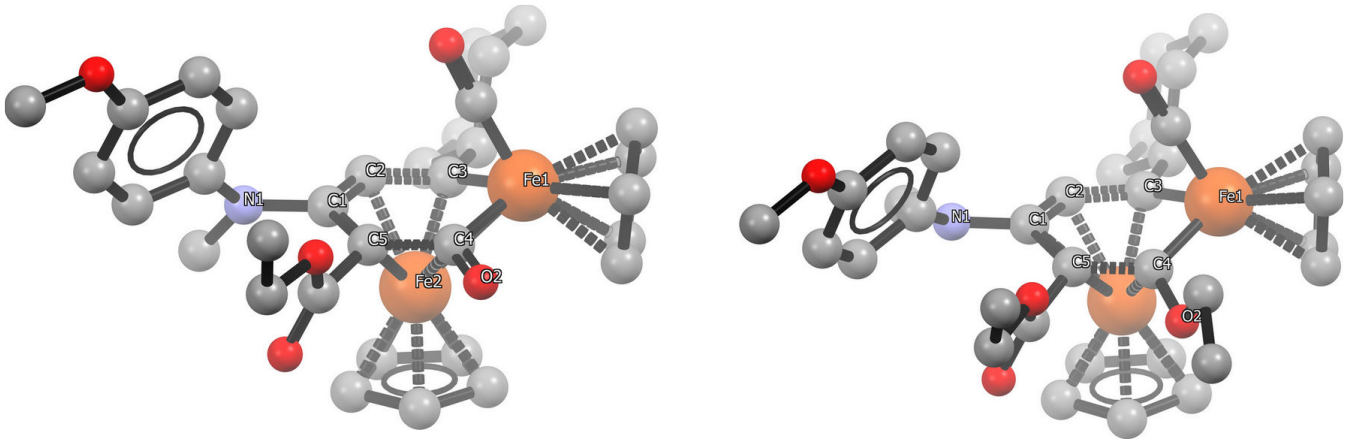

Table S3. Salient distances (Å) and angles (°) computed for **4a** and **5aEt**, and comparison with the corresponding experimental X-ray data

	4a	**4a^{EXP}**	**5aEt**	**5aEt^{EXP}**
Fe2-C1	2.147	2.1066(15)	2.275	2.218(3)
Fe2-C2	2.089	2.0724(14)	2.103	2.088(3)
Fe2-C3	2.033	2.0131(15)	2.042	2.027(3)
Fe1-Fe2	2.642	2.6251(5)	2.589	2.5708(6)
Fe1-C3	1.954	1.9530(14)	1.955	1.954(3)
Fe1-C4	1.958	1.9636(16)	1.923	1.915(3)
Fe2-C4	2.286	2.2478(15)	2.026	2.012(3)
C1-N1	1.417	1.4315(18)	1.365	1.387(4)
C1-C2	1.422	1.422(2)	1.428	1.429(4)
C2-C3	1.403	1.417(2)	1.404	1.408(4)
C1-C5	1.417	1.428(2)	1.441	1.436(4)
C5-C4	1.466	1.465(2)	1.422	1.431(4)
C4-O2	1.236	1.2435(18)	1.374	1.384(3)
C1-C2-C3	124.86	123.90(13)	127.08	126.8(3)
N1-C1-C2	117.08	117.74(12)	119.50	119.3(2)
Fe1-C4-Fe2	76.57	76.79(5)	81.90	81.73(11)

3.2. IR spectra

For system **4a**, harmonic frequencies were computed using DFT in dichloromethane, and the corresponding IR spectrum is shown in Figure S58. The main harmonic frequencies are listed In Table S4. The computed frequencies were scaled by a factor λ = 0.9727, which was obtained as:

$$\lambda = \frac{\nu}{\omega}$$

ω being the computed frequency and ν the experimental fundamental frequency for the (Fe^1)C-O stretching. Despite the limitations of the harmonic model approximation, we can reasonably assign key signals in the experimental spectrum. Specifically, the C-O stretching in the (Fe^1)CO and (EtO)C=O groups appears at 1958 and 1691 cm^{-1}, respectively. Moreover, the experimental signal at 1510 cm^{-1} likely corresponds to the C^4-O stretching, which is observed at 1507 cm^{-1} in the scaled simulated spectrum.

Figure S58. Simulated IR spectrum of **4a** in CH_2Cl_2.

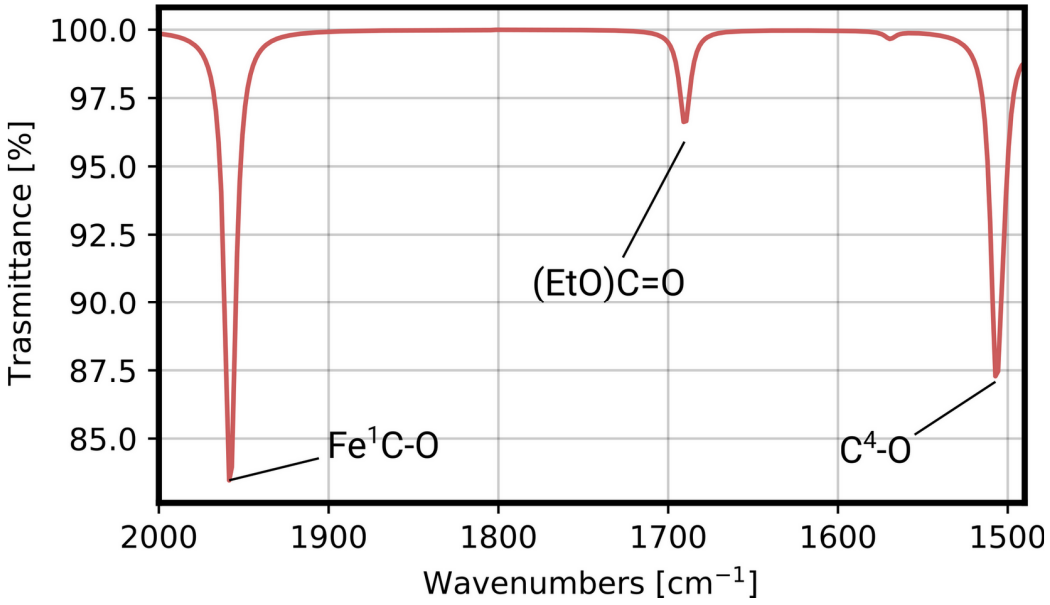

Table S4. Harmonic frequencies (in wavenumbers) for the principal stretching modes computed with DFT for **4a**. The computed scaling factor is 0.9727.

Atom group	[cm^{-1}]	[cm^{-1}]
(Fe^1)C-O	2013	1958
(OEt)C=O	1738	1691
C^4-O	1549	1507

The same analysis was carried out for system **5a**, and the computed IR spectrum is shown in Figure S59. The main harmonic frequencies are listed in Table S5. In this case, the scaling factor is 0.9714. In addition to the clear assignment of the (Fe^1)C-O signal, the absorption at 1728 cm^{-1} can be attributed to the (EtO)C=O stretching. The

low-intensity signals around 1607 cm^{-1} are ascribable to stretching modes of the 4-C_6H_4OMe moiety. The stretching of the C^1-N bond appears at 1480 cm^{-1} in the scaled simulated spectrum, therefore this signal is expected to fall outside the wavenumber range detected experimentally.

Figure S59. Simulated IR spectrum of **5a** in CH_2Cl_2.

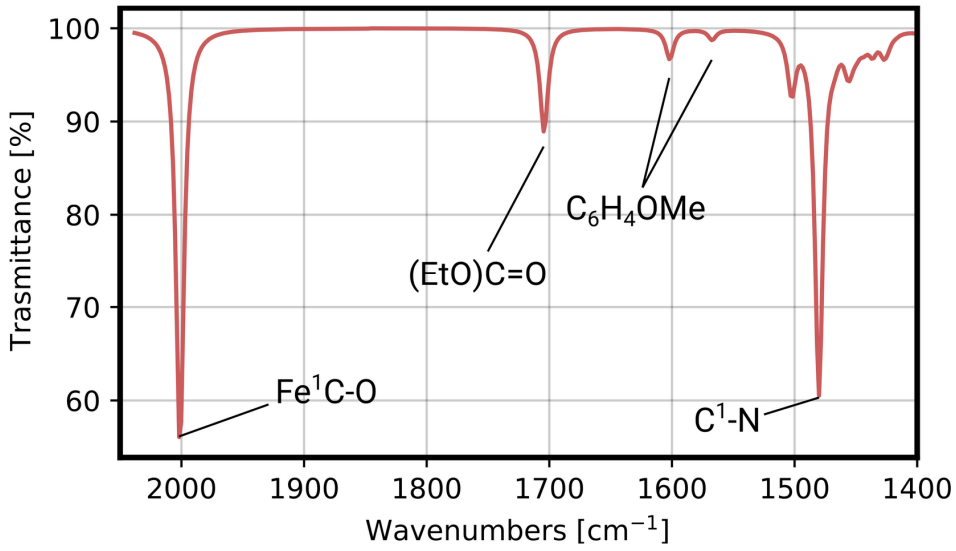

Table S5. Harmonic frequencies in wavenumbers for the principal stretching modes computed with DFT for **5a**. The computed scaling factor is 0.9714.

Atom group	**[cm^{-1}]**	**[cm^{-1}]**
(Fe^1)C-O	2060	2001
(OEt)C=O	1754	1704
C_6H_4OMe	1649	1602
C^1-N	1524	1480

Figure S60. Computed IR spectra of **4a** (left) and **5aEt** (right) and their corresponding redox pairs in CH_3CN. For **5aEt**, the computed $\Delta\nu_{CO}$ following the oxidation and reduction processes correspond to 36 cm^{-1} and 72 cm^{-1}, respectively.

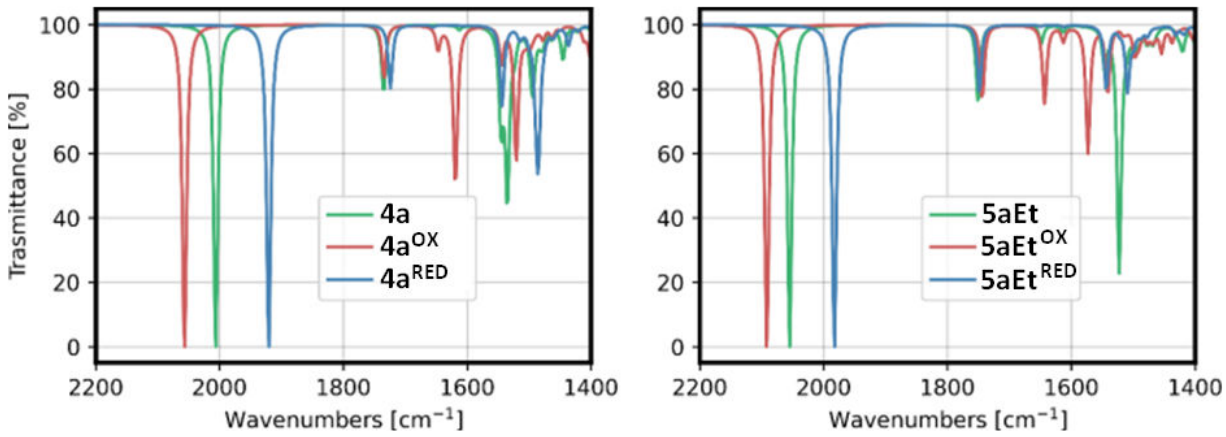

3.3. NMR spectra

In Tables S6 and S7, we report representative ^{1}H chemical shifts computed at both the DFT and CASSCF levels of theory, alongside experimental values. For CASSCF calculations, we considered all orbitals with occupation numbers ranging from 0.025 to 1.956 for **4a** and from 0.019 to 1.979 for **5aEt** as active, correlating 14 electrons in 14 orbitals for both molecular systems. Additionally, Tables S8 and S9 provide the computed ^{13}C chemical shift values for a selection of representative nuclei. DFT calculations were carried out using the def2-TZVP basis set in acetone (using PCM, ε_r= 20.493), while CASSCF calculations were conducted with the def2-SVP basis set in vacuum.

Table S6. ^{1}H chemical shifts (in ppm) for **4a** computed at the DFT and CASSCF levels of theory, compared with experimental data.

Nucleus	B3LYP	CASSCF(14,14)	Exp. (acetone-d_6)
4H, C_6H_4	6.84	6.20	6.71-6.65
1H, C^2H	6.13	5.72	6.59
10H, Cp	4.73, 4.14	4.00, 3.73	4.99, 4.72
1H, CH^{Cy}	4.05	4.14	3.71
3H, OMe	3.82	3.39	3.68
3H, NMe	3.21	2.77	3.08
10H, CH_2^{Cy}	2.09	2.08	2.63-2.19, 2.01-1.44
3H, CH_3^{Et}	0.74	0.70	0.87

Table S7. ^{1}H chemical shifts (in ppm) for **5aEt** computed at the DFT and CASSCF levels of theory, compared with experimental data.

Nucleus	B3LYP	CASSCF(14,14)	Exp. (acetone-d_6)
4H, C_6H_4	7.11	6.93	6.88
1H, C^2H	5.82	5.79	6.40
10H, Cp	4.37, 5.24	4.56, 4.04	5.72, 5.28
3H, $OCH_2C\underline{H}_3$	1.43	1.84	1.44
2H, $OC\underline{H}_2CH_3$	4.20	4.02	4.19
3H, NMe	3.31	2.79	3.34
10H, CH_2^{Cy}	2.00	2.05	2.58-2.17, 1.99-1.60
3H, $OCOCH_2C\underline{H}_3$	0.96	1.06	1.19

Table S8. ^{13}C chemical shifts (in ppm) for **4a** computed at the DFT and CASSCF levels of theory, compared with experimental data.

Nucleus	B3LYP	CASSCF(14,14)	Exp. (acetone-d_6)
C^1	137.7	127.1	125.3
C^2	85.9	89.2	81.1
C^3	253.4	243.8	217.3
C^4	269.2	275.4	226.0
C^5	74.7	66.0	64.9
Fe^1-Cp	96.6	80.6	93.3
Fe^2-Cp	81.7	72.6	80.8
OMe	58.1	50.7	55.7
NMe	43.3	38.7	42.1
CH^{Cy}	66.1	51.1	61.0
CH_3^{Et}	15.9	14.5	14.1

Table S9. ^{13}C chemical shifts (in ppm) for **5aEt** computed at the DFT and CASSCF levels of theory, compared with experimental data.

Nucleus	B3LYP	CASSCF(14,14)	Exp. (acetone-d_6)
C^1	145.2	144.0	130.2
C^2	72.4	66.9	73.8
C^3	269.2	244.9	221.9
C^4	278.9	257.9	235.6
C^5	111.0	104.7	101.7
Fe^1-Cp	96.3	87.4	93.9
Fe^2-Cp	85.0	76.0	84.8
$C_6H_4O\underline{Me}$	58.9	51.6	55.8
NMe	46.0	41.0	43.2
OCO	178.4	173.2	167.5
$OCOCH_2\underline{C}H_3$	15.6	13.9	13.9

3.4. Computational mechanistic study

Transition states and intermediates were optimized at the B3LYP/def2-TZVP (D3) level of theory with implicit THF solvation. The intrinsic reaction coordinate (IRC) method confirmed the connection between each transition state and its corresponding intermediates. Intermediates **I1** and **I1'** represent different conformers, differing in the orientation of the ethyl group within the CO_2Et substituent. **I2**, **I2'** and **I2''** are conformers related by rotation about the C^1-C^2 bond, which brings C^2 closer to Fe^1. Instead, **I2'''** is featured by C^5 closer to C^4.

Figure S61. Full reaction pathway for the rearrangement of the diiron bis-alkylidene complex **3b** to **4b**. See also the video "Reaction Mechanism". Attempts to isolate any intermediate experimentally were unsuccessful.

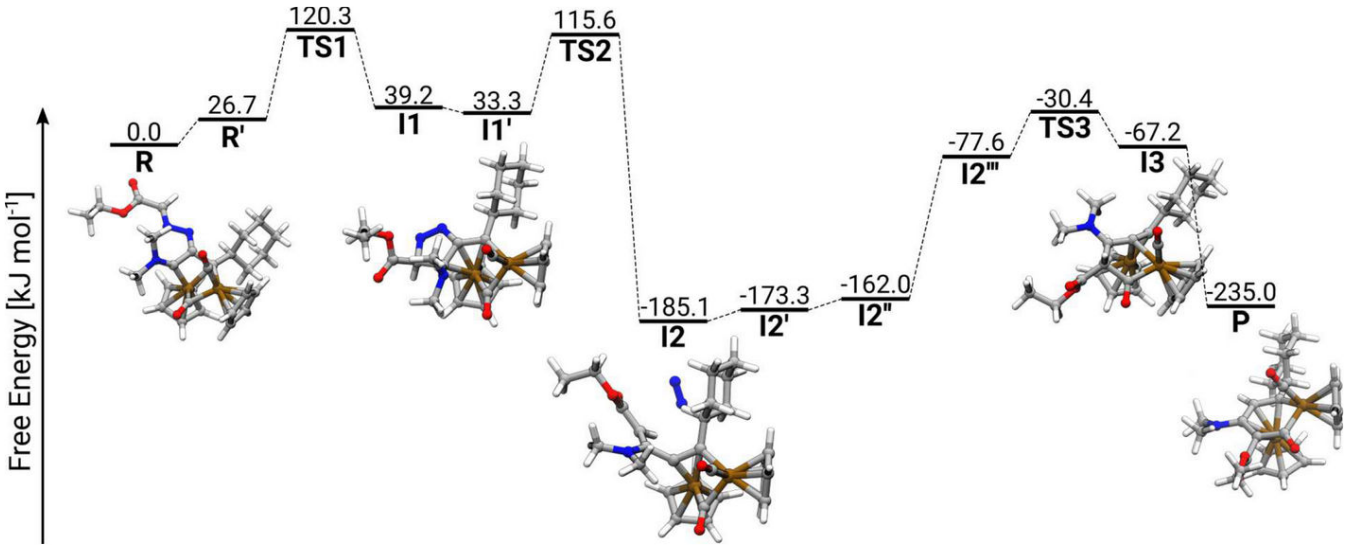

Figure S62. Mercury views of the optimized structures of the organometallic unit of **R** (**3b**), **P** (**4b**) and key reaction intermediates (**I1'**, **I2**, **I3**) in THF, referred to Figure S61; H atoms (except H5) omitted for clarity

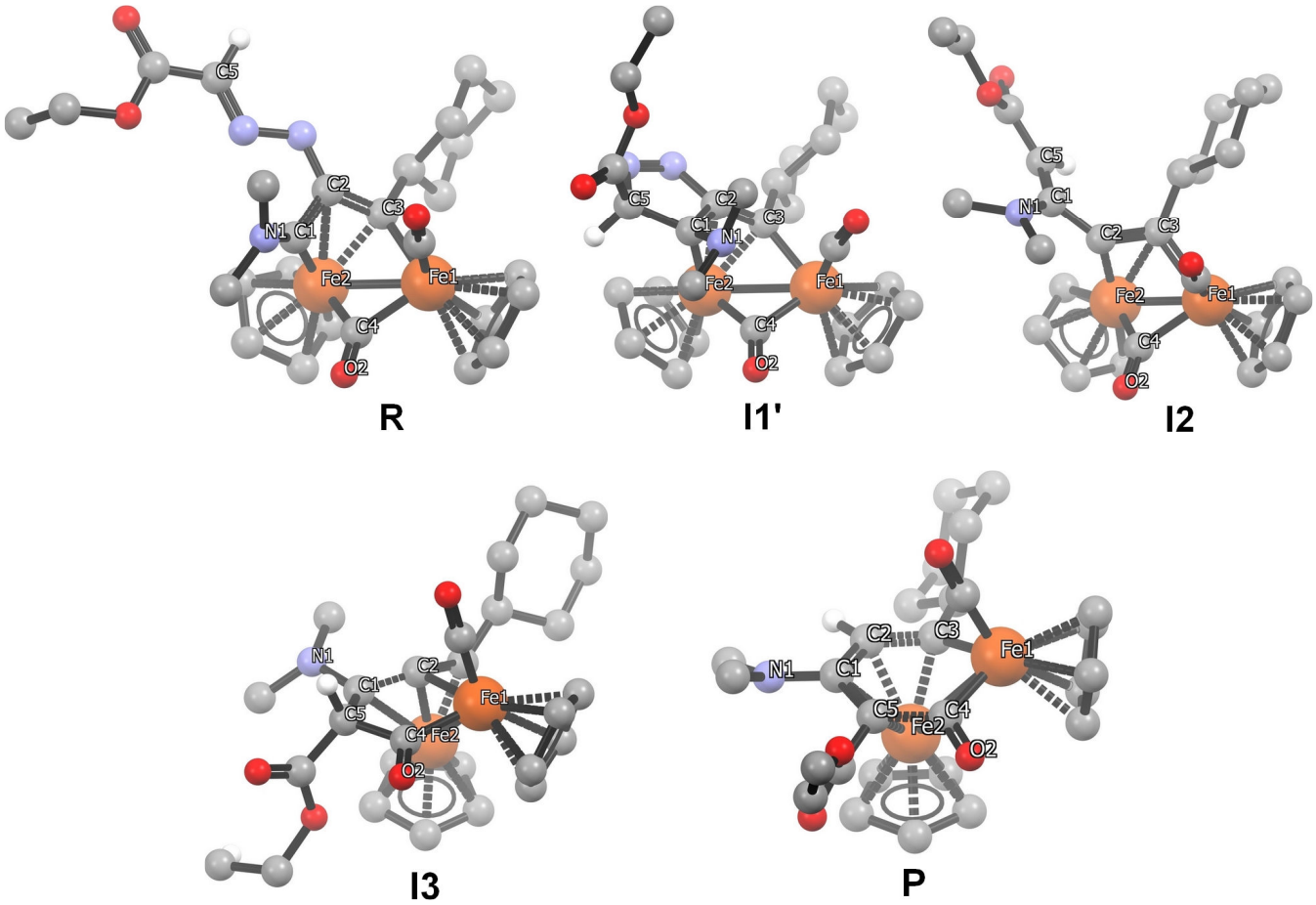

Table S10. Salient distances (Å) and angles (°) computed for **R** (**3b**), **P** (**4b**), **R'**, **I1**, **I1'**, **I2**, **I2'**, **I2''**, **I2'''**, **I3**

	R	R'	I1	I1'	I2	I2'	I2''	I2'''	I3	P
Fe2-C1	1.883	1.890	2.149	2.154	3.025	3.263	3.267	3.144	2.332	2.203
Fe2-C2	2.219	2.334	2.027	2.028	1.807	1.980	2.024	1.913	1.944	2.086
Fe2-C3	2.054	2.045	2.059	2.058	2.092	1.897	1.856	1.803	1.895	2.028
Fe1-Fe2	2.551	2.541	2.561	2.561	2.506	2.534	2.546	2.779	2.970	2.642
Fe1-C3	2.015	2.031	1.985	1.984	2.031	2.163	2.600	2.901	2.530	1.951
Fe1-C4	1.934	1.934	1.946	1.948	1.969	2.084	1.918	1.784	1.967	1.956
Fe2-C4	1.879	1.872	1.894	1.893	1.875	1.799	1.906	3.106	3.345	2.263
C1-N1	1.287	1.296	1.427	1.428	1.356	1.359	1.360	1.391	1.410	1.378
C1-C2	1.441	1.448	1.441	1.440	1.466	1.456	1.485	1.479	1.376	1.432
C2-C3	1.441	1.454	1.426	1.427	1.366	1.332	1.339	1.373	1.329	1.403
C1-C5	==	==	1.547	1.545	1.381	1.383	1.377	1.371	1.512	1.427
C5-C4	==	==	==	==	==	==	==	==	1.570	1.468
C4-O2	1.176	1.178	1.172	1.172	1.174	1.177	1.176	1.141	1.213	1.238
C1-C2-C3	111.12	108.22	129.43	129.65	135.47	140.82	133.57	129.01	144.91	126.10
N1-C1-C2	131.84	129.28	124.39	125.30	115.03	120.26	118.46	115.29	120.84	118.22
Fe1-C4-Fe2	83.97	83.74	83.66	83.65	81.31	81.14	83.46	62.57	61.70	77.15

Figure S63. Energy diagram illustrating intermediates and transition states involved in the **I3** to **P** rearrangement mediated by ethyl diazoacetate. These calculations were carried out using the same DFT level of theory with the def2-SVP basis set.

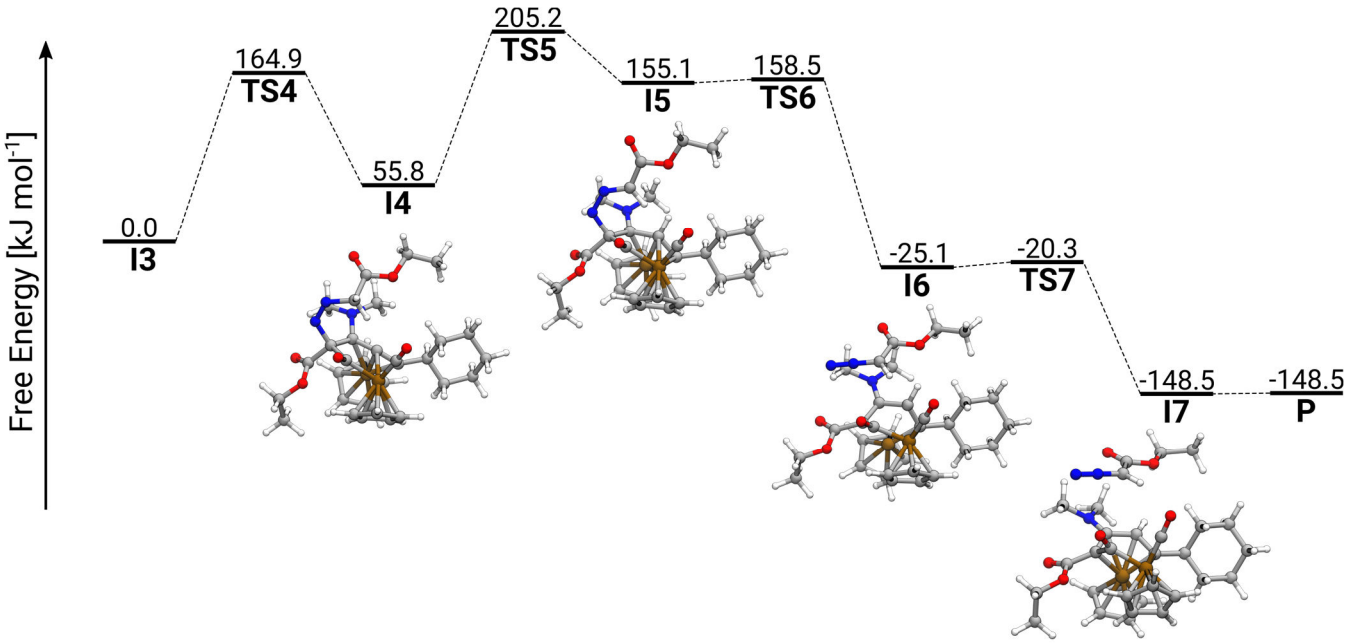

Figure S64. Mercury views of the optimized structures of the organometallic unit of **I4**, **I5, I6** and **I7** in THF, referred to Figure S63; H atoms (except those involved in H transfer) omitted for clarity

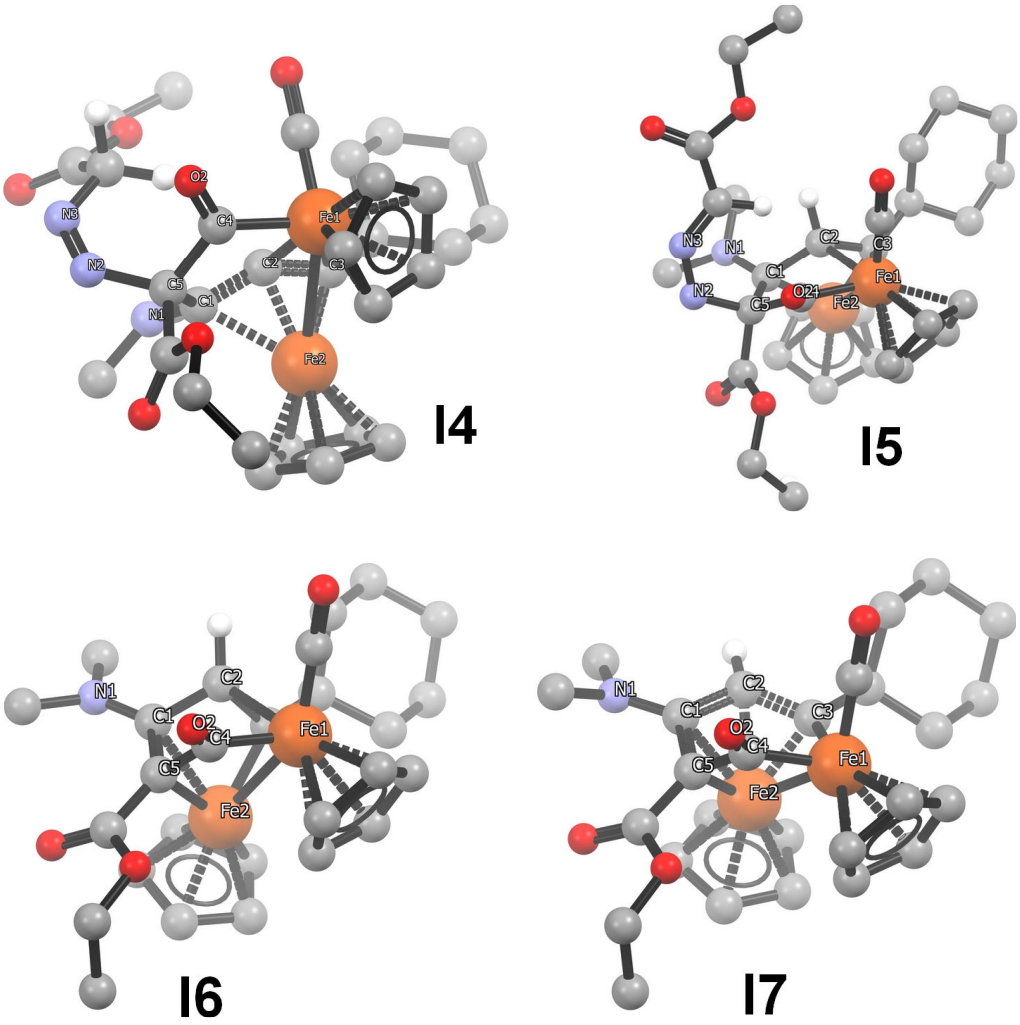

Table S11. Salient distances (Å) and angles (°) computed for **I4**, **I5**, **I6** and **I7**

	I4	**I5**	**I6**	**I7**
Fe2-C1	2.217	2.083	2.310	2.15
Fe2-C2	1.944	2.069	2.567	2.07
Fe2-C3	1.943	1.827	1.966	1.95
Fe1-Fe2	2.936	2.819	2.846	2.71
Fe1-C3	2.248	2.065	2.168	2.03
Fe1-C4	1.989	2.003	1.926	1.91
Fe2-C4	3.596	3.500	3.077	2.89
C1-N1	1.410	1.359	1.357	1.37
C1-C2	1.394	1.538	1.494	1.44
C2-C3	1.329	1.430	1.388	1.42
C1-C5	1.542	1.547	1.422	1.45
C5-C4	1.589	1.566	1.510	1.50
C4-O2	1.205	1.198	1.212	1.22
C5-N2	1.509	1.526	3.849	4.165
N2-N3	1.232	1.279	1.131	1.131
C1-C2-C3	146.26	128.36	110.85	124.1
N1-C1-C2	120.38	114.77	117.24	121.4
Fe1-C4-Fe2	54.71	53.63	64.64	64.9

3.5. Electronic structure and aromaticity analysis

3.5.1. Electron density and NBO analysis

Figure S65. DFT calculated total electron density (isovalue = 0.09) for **4a** (left) and **5aEt** (right), in THF

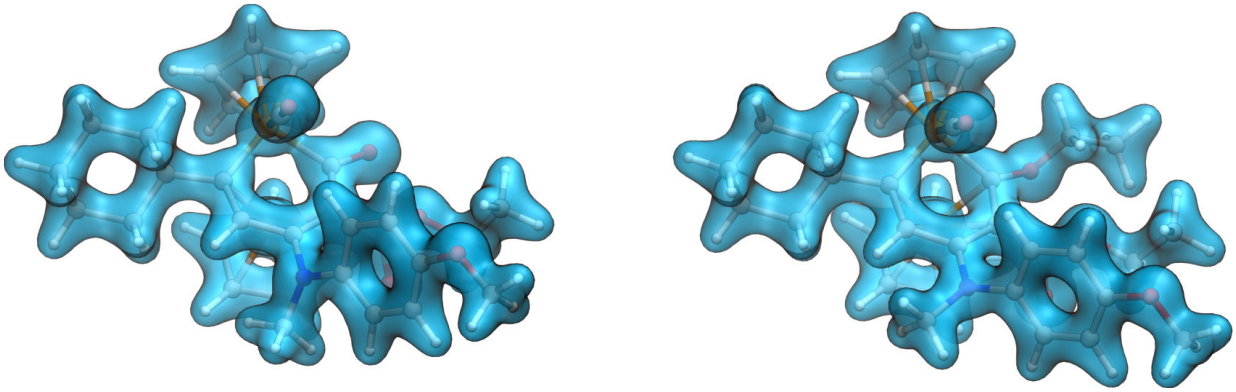

Figure S66. Natural bond orbitals (NBO) for the Fe^1-C^3 and Fe^1-C^4 bonds in **4a**

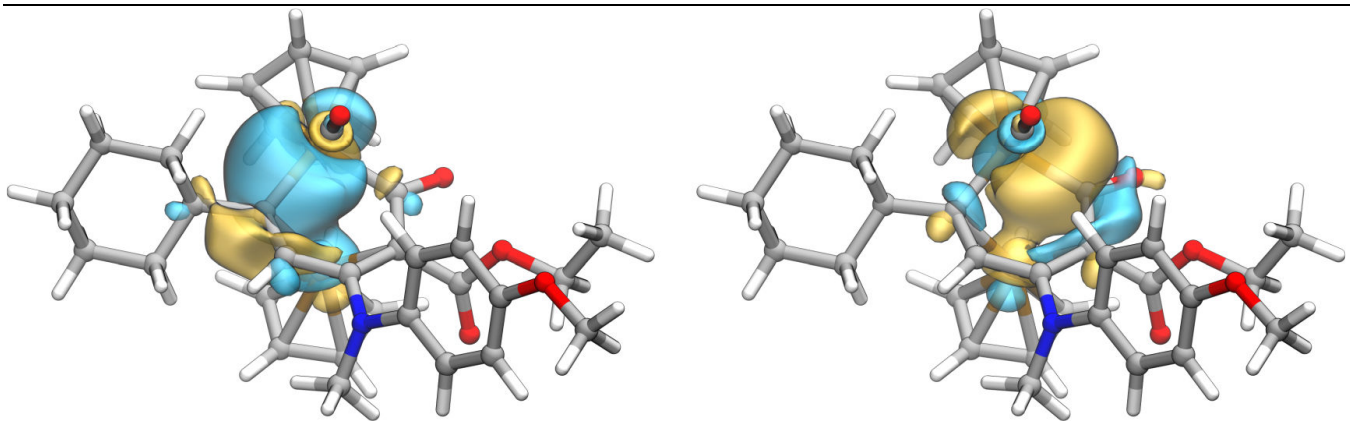

According to the natural bond analysis, the Fe^1-C^3 NBO of **4a** is composed of a hybrid $sp^{1.9}$ orbital on C^3 and a hybrid $sp^{1.2}d^{3.2}$ orbital on Fe^1, while the Fe^1-C^4 NBO is formed of a hybrid $sp^{1.7}$ orbital on C^4 and a $sp^{1.1}d^{3.4}$ on Fe^1. For **5aEt**, the Fe^1-C^3 NBO is composed of a hybrid $sp^{1.9}$ orbital on C^3 and a hybrid $sp^{1.2}d^{3.4}$ orbital on Fe^1. Instead, the Fe^1-C^4 NBO consists of a hybrid $sp^{1.5}$ orbital on C^4 and a $sp^{1.3}d^{3.3}$ one on Fe^1.

Figure S67. Frontier molecular orbitals for **4a** and its oxidized and reduced forms

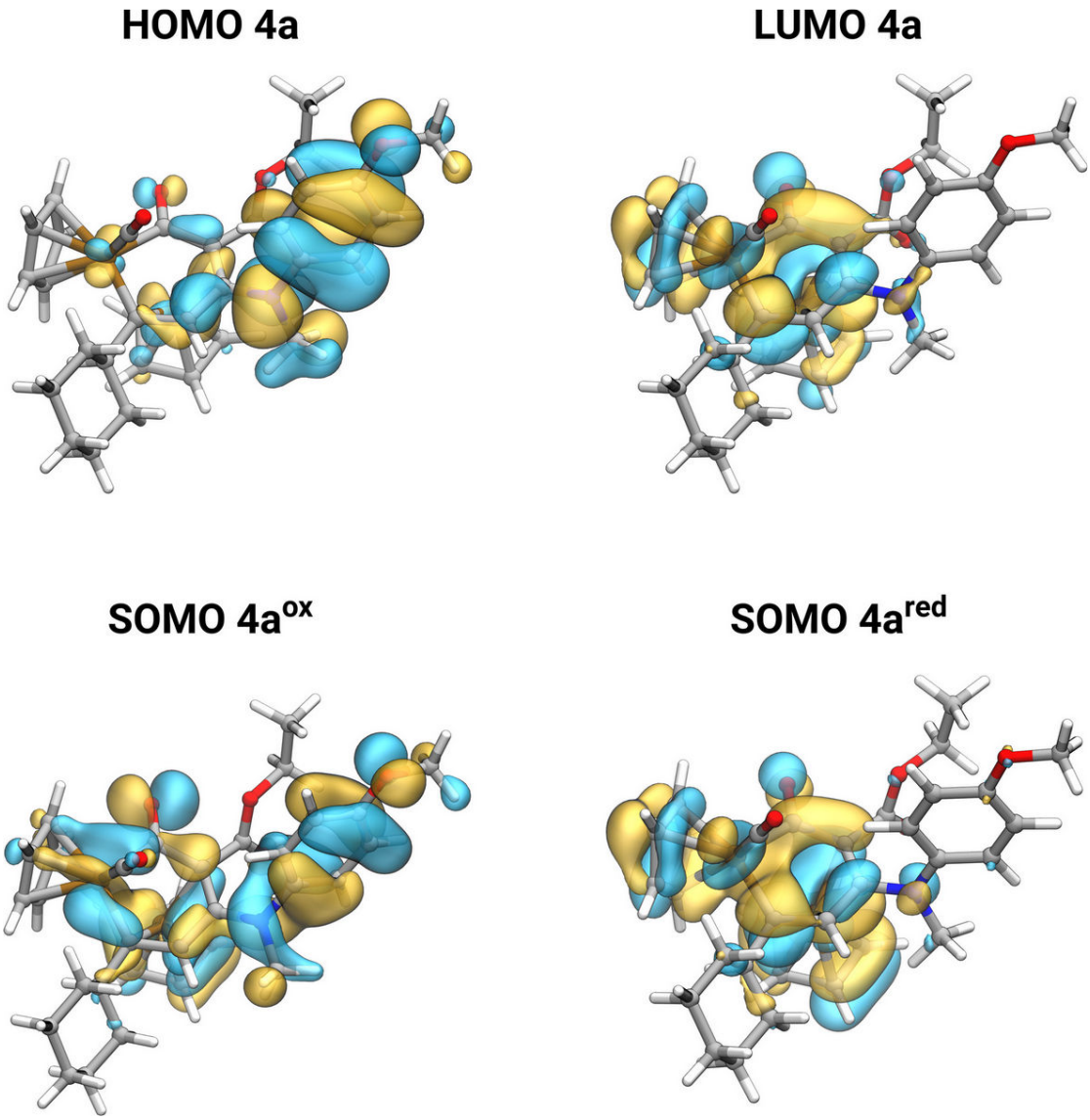

Figure S68. Mercury views of the optimized structures of the reduced and oxidized forms of **4a** and **5aEt**

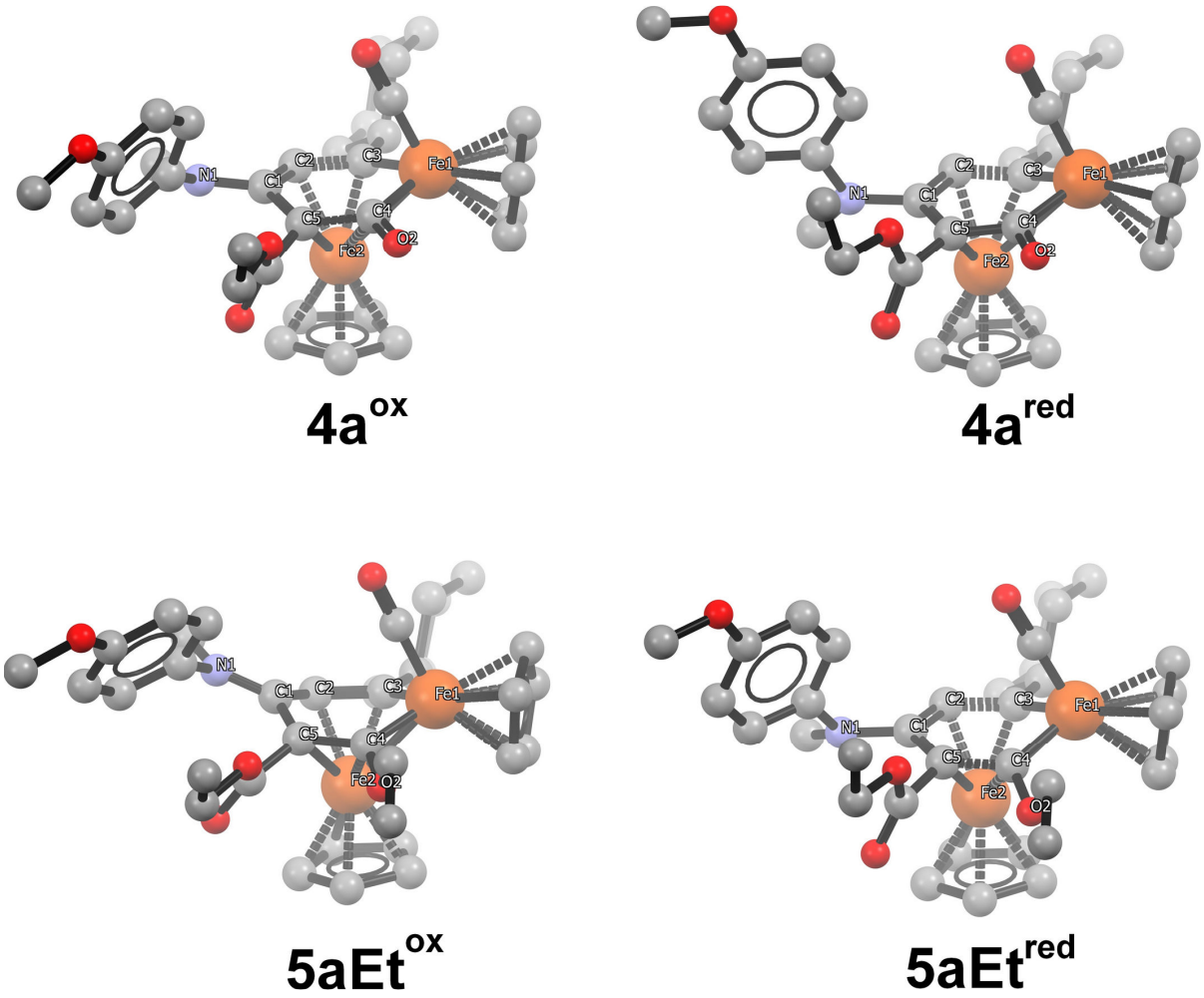

Table S12. Salient distances (Å) and angles (°) computed for the reduced and oxidized forms of **4** and **5aEt**

	5aEt^{ox}	**5aEt^{red}**	**4a^{ox}**	**4a^{red}**
Fe2-C1	2.450	2.111	2.288	2.034
Fe2-C2	2.119	2.094	2.076	2.075
Fe2-C3	2.142	2.109	2.074	2.086
Fe1-Fe2	2.657	2.820	2.698	2.970
Fe1-C3	1.949	1.971	1.948	2.001
Fe1-C4	1.925	1.928	1.974	1.951
Fe2-C4	2.135	2.096	2.458	2.545
C1-N1	1.318	1.409	1.351	1.433
C1-C2	1.452	1.421	1.448	1.420
C2-C3	1.400	1.403	1.403	1.400
C1-C5	1.464	1.431	1.443	1.428
C5-C4	1.415	1.414	1.481	1.461
C4-O2	1.355	1.402	1.219	1.249
C1-C2-C3	125.05	125.29	125.86	122.01
N1-C1-C2	120.44	121.05	118.44	119.32
Fe1-C4-Fe2	81.59	88.89	74.09	81.50

3.5.2. Current strength

To determine the appropriate window for the integration of the magnetically induced current density, we performed a current profile analysis. The plots, shown in Figure S69 for **4a** and **5aEt**, display the diatropic, paratropic, and total current profiles for each compound. The vertical bar denotes the position of the C^1-C^2 bond through which the integration is carried out. Therefore, negative x values correspond to points inside the ferrabenzene ring, while positive x values correspond to points outside the ring. The plots exhibit the characteristic shape of an aromatic ring, with the diatropic part dominating on the outside. The increase in the diatropic contribution at x values around -3 bohr is due to the atomic currents on the Fe^1 atom, while the oscillations starting from 3 bohr onwards are likely due to the proximity of the ligands, in particular the methyl group bound to the nitrogen atom.

Figure S69. Current profiles for **4a** and **5aEt**

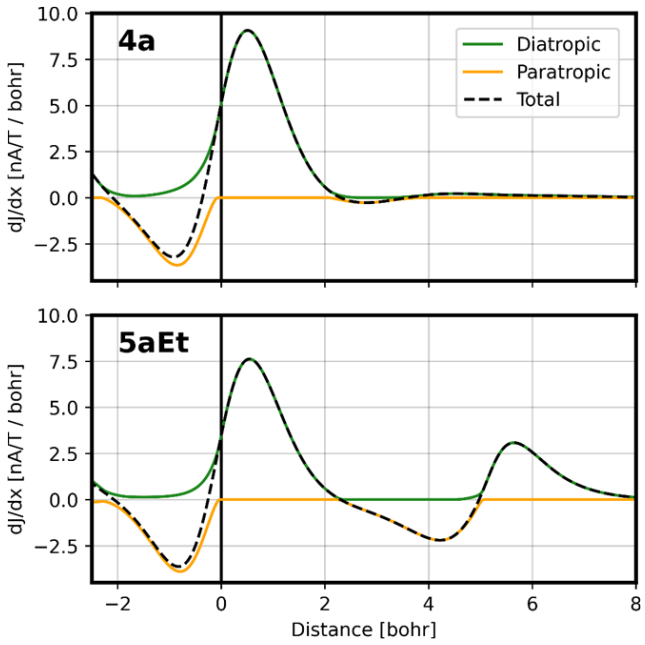

4. Electrochemistry

Cyclic voltammetry (CV) measurements were carried out with a PalmSens4 instrument interfaced to a computer employing PSTrace5 electrochemical software. Anhydrous CH_3CN (Merck) was stored under argon over 3Å molecular sieves. $[N^nBu_4]PF_6$ (Fluka, electrochemical grade) was used without further purification. CV measurements were carried out under argon using 0.1 mol dm^{-3} $[N^nBu_4]PF_6$ in CH_3CN as the supporting electrolyte. The working and the counter electrodes consisted of a Pt disk sealed in a PEEK tube and a Pt gauze, respectively. A leakless miniature Ag/AgCl/KCl (3.4 mol dm^{-3}) electrode (eDAQ) was employed as a reference. The three-electrode home-built cell was pre-dried by heating under vacuum and filled with argon. The Schlenk-type construction of the cell maintained anhydrous and anaerobic conditions. The solution of the supporting electrolyte, prepared under argon, was introduced into the cell, and the CV of the solvent was recorded. The analyte was then introduced, and voltammograms were recorded. Controlled potential coulometry was performed in an H-shaped cell with anodic and cathodic compartments separated by a sintered-glass disk. The working macroelectrode was a platinum gauze; a Pt foil was used as the counter electrode and the reference was the leakless miniature Ag/AgCl/KCl (3.4 mol dm^{-3}) electrode. Hydrodynamic voltammetry with the renewal of the diffusion layer made use of rotating disk electrode Metrohm 628-10, consisting of platinum disk surrounded with an insulating Teflon . Under the present experimental conditions, the one-electron oxidation of ferrocene in CH_3CN occurred at E° = +0.42 V *vs* Ag/AgCl. IR-SEC measurements were carried out using an OTTLE cell[10] equipped with CaF_2 windows, platinum mini-grid working and auxiliary electrodes, and a silver wire pseudo-reference electrode. During the micro-electrolysis procedures, the electrode potential was controlled by a PalmSens4 instrument interfaced to a computer employing PSTrace5 electrochemical software. Argon-saturated $CH_3CN/[N^nBu_4]PF_6$ 0.1 mol dm^{-3} solutions of the analyzed compound were used. The *in-situ* SEC experiments were performed by collecting IR spectra at fixed time intervals during oxidation or reduction, obtained by continuously increasing or lowering the initial working potential at a scan rate of 1.0 or 2.0 mV s^{-1}.

Figure S70. CV recorded at a Pt electrode in a CH_3CN solution of **5aEt**. $[N^nBu_4]PF_6$ (0.1 mol dm^{-3}) as supporting electrolyte. Scan rate: 0.1 V s^{-1}. The arrow indicates the direction of the scan

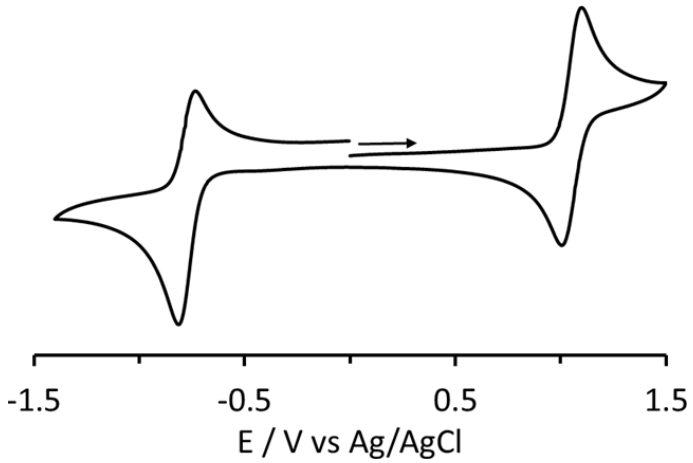

Figure S71. IR spectra of a CH_3CN solution of **5aEt** recorded in an OTTLE cell during the progressive decrease of the working electrode (WE) potential from to –0.7 to –1.1 V (*vs* Ag pseudo reference electrode; scan rate 2 mV s^{-1}). $[N^nBu_4]PF_6$ (0.1 mol dm^{-3}) as the supporting electrolyte. The absorptions of the solvent and supporting electrolyte have been subtracted

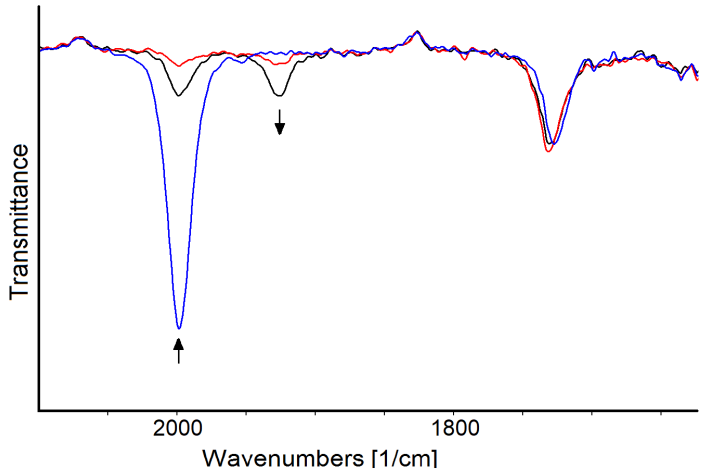

Figure S72. CV recorded at a Pt electrode in a CH_3CN solution of **4a**. $[N^nBu_4]PF_6$ (0.1 mol dm^{-3}) as supporting electrolyte, from –1.4 to +0.8 V (black line) and from –0.4 to –1.9 V (red line). Scan rate: 0.1 V s^{-1}. The arrows indicate the direction of the scan

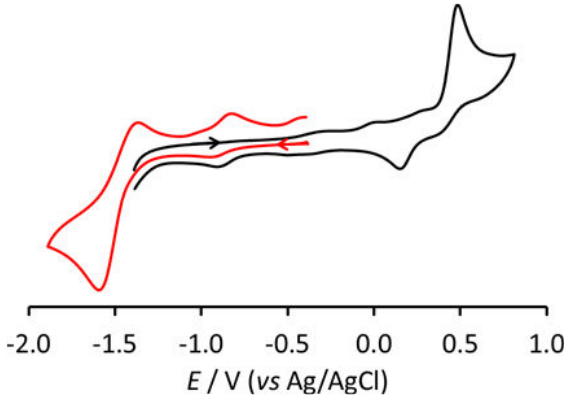

Figure S73. IR spectra of a CH_3CN solution of **4a** recorded in an OTTLE cell during a) the progressive decrease of the WE potential from to –0.9 to –1.5 V (*vs* Ag pseudo reference electrode; scan rate 2 mV s^{-1}); b) the progressive back oxidation; c) IR spectra of a CH_3CN solution of **4a** recorded in an OTTLE cell before (pink line) and after (blue line) the reduction and back-oxidation steps. $[N^nBu_4]PF_6$ (0.1 mol dm^{-3}) as the supporting electrolyte. The absorptions of the solvent and supporting electrolyte have been subtracted

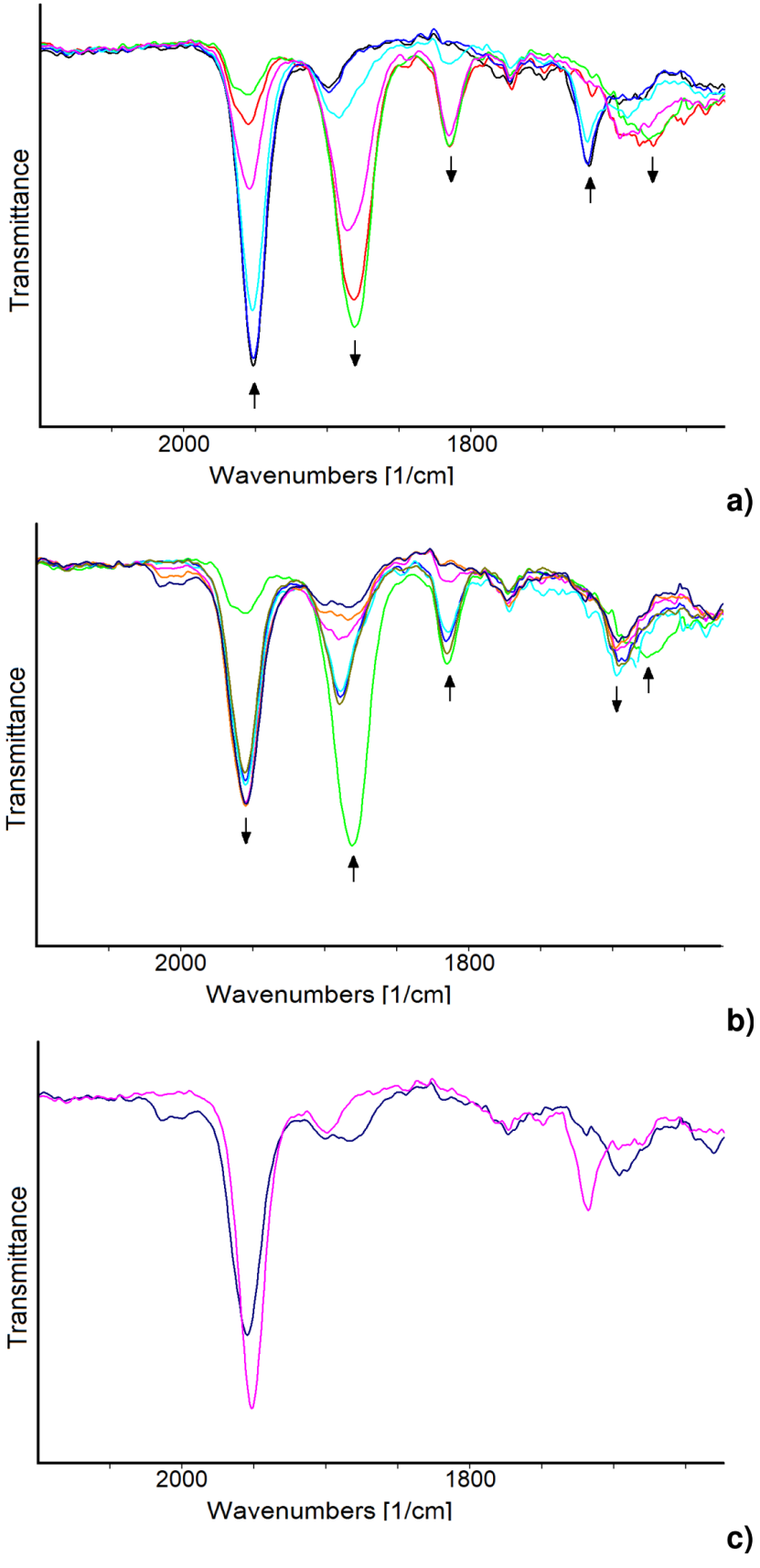

5. Aqueous characterization

5.1. Octanol/water partition coefficients (Log P_{ow}). Partition coefficients (P_{ow}), defined as $P_{ow} = c_{org}/c_{aq}$, where c_{org} and c_{aq} are molar concentrations of the compound in the organic and aqueous phases, respectively, were determined by the shake-flask method combined with UV-Vis spectroscopy, according to a previously described procedure.[11,12] All operations were carried out at room temperature (*ca*. 23 °C). For UV-Vis quantification, the wavelength corresponding to a well-defined absorption band of each iron complex (within the 310-350 nm range) was selected. Stock solutions (*ca.* 3 mg) were prepared in water-saturated octanol (≈ 4 mL), with the addition of 50-80 µL of acetone to aid initial dissolution. The solution was then diluted with water-saturated octanol (≈ 8 mL) to achieve an absorbance at λ_{max} in the range of 1.0 - 1.2, and the UV-Vis spectrum was recorded (providing A^0_{org}). An aliquot of the solution (1.5 mL) was transferred into a test tube, and an equal volume (1.5 mL) of octanol-saturated water was added. The mixture was vigorously stirred for 30 minutes and subsequently centrifuged (2500 rpm, 5 min). The UV-Vis spectrum of the organic phase after partition was recorded (A^f_{org}). The partition coefficient was calculated using the equation: $P_{ow} = A^f_{org}/(A^0_{org} - A^f_{org})$. The procedure was performed in triplicate for each sample, starting from the same stock solution. Naphthoquinone was used as a reference compound (Log P_{ow} = 1.8 ± 0.2; literature: 1.71).[13] The results are summarized in Table S13 and are reported as mean values ± standard deviation.

5.2. D_2O solubility. A suspension of the selected iron complex (3-5 mg) in a D_2O solution (0.7 mL) containing dimethylsulfone (Me_2SO_2, 6.98 x 10^{-4} M) as an internal standard[14] was vigorously stirred at *ca.* 23 °C for 1 h. The resulting mixture (a saturated solution of the iron complex in D_2O with Me_2SO_2 + undissolved solid) was filtered through Celite, and the filtrated solution was transferred into an NMR tube and analyzed by ^{1}H NMR spectroscopy (delay time = 10 s; number of scans = 32). An integral value 1.0 was assigned to the C^2H signal of each iron complex. The concentration (= solubility, **S**) was then calculated using the equation: $\mathbf{S = C_s \times (6 / I_s)}$ (where $\mathbf{C_s}$ is the concentration of Me_2SO_2, and $\mathbf{I_s}$ is the integral of the Me_2SO_2 signal at δ = 3.10 ppm, corresponding to **6** protons). Solubility data are compiled in Table S13, and the corresponding ^{1}H NMR spectra are shown in Figures S74-S76. The NMR signals of the iron complexes are listed below.

5a. ^{1}H NMR (D_2O): δ/ppm = 6.89 (s, 4H, C_6H_4); 6.26 (s, 1H, C^2H); 5.54, (s, 5H, Cp); 5.09 (s, 5H, Cp); 3.85 (s, 3H, $C^4O\underline{Me}$); 3.78, (s, 3H, $C_6H_4O\underline{Me}$); 2.93 (s, 3H, NMe).

5b. ^{1}H NMR (D_2O): δ/ppm = 6.13 (s, 1H, C^2H); 5.49 (s, 5H Cp); 5.02 (s, 5H Cp); 3.96 (s, 3H, C^4OMe); 3.80 (t, $^3J_{HH}$ = 12.3, 1H, CH^{Cy})*; 2.79 (s, 6H NMe_2); 1.44 (t, $^3J_{HH}$ = 7.1 Hz, 3H, CH_3^{Et}).

5aEt. ^{1}H NMR (D_2O): δ/ppm = 6.87 (s, 4H, C_6H_4); 6.28 (s, 1H, C^2H); 5.52, (s, 5H, Cp); 5.11 (s, 5H, Cp); 3.77 (s, 3H, $C_6H_4O\underline{Me}$), 2.92 (s, 3H, NMe); 1.36 (t, $^{3}J_{HH}$ = 7.0 Hz, 3H, CH_3^{Et}).

5.3. NMR stability studies in DMSO and aqueous solutions

5.3.1. DMSO-d_6. Each iron complex was dissolved into a DMSO-d_6 solution (0.7 mL) containing Me_2SO_2 (5.7 x 10^{-3} M) as an internal standard. The final concentrations of the complexes were 5.7 x 10^{-3} M (**5a**), 8.7 x 10^{-3} M (**5b**), 5.5 x 10^{-3} M (**5aEt**), respectively. The resulting solutions were analyzed by ^{1}H NMR spectroscopy (delay time = 10 s; number of scans = 32) and then kept at room temperature (*ca.* 23 °C). Additional ^{1}H NMR spectra were recorded after 2h, 24h, and 48h. The percentage of residual complex at each time point was calculated by comparing the integrals of the Me_2SO_2 reference signal (δ = 2.99 ppm) at time zero and after incubation. The C^2H signal of the complex was set to an integral value of 1.0. Stability data are compiled in Table S14. The ^{1}H NMR signals of the complexes at time zero are listed below, and the corresponding spectra are shown in Figures S77-S79.

5a. ^{1}H NMR (DMSO-d_6): δ/ppm = 6.85 (d, $^{3}J_{HH}$ = 9.0 Hz, 2H, C_6H_4); 6.76 (d, $^{3}J_{HH}$ = 8.9 Hz, 2H, C_6H_4); 6.21 (s, 1H, C^2H); 5.67 (s, 5H, Fe^1-Cp), 5.20 (s, 5H, Fe^2-Cp); 3.92 (dq, $^{2}J_{HH}$ = 10.7 Hz, $^{3}J_{HH}$ = 7.2 Hz, 1H, CH_2^{Et}); 3.86 (m, 1H, CH_2^{Et}); 3.82 (s, 3H, C^4OMe); 3.71 (s, 3H, $C_6H_4O\underline{Me}$); 3.60 (m, 1H, CH^{Cy}); 3.21 (s, 3H, NMe); 2.37-1.35 (m, 10H, CH_2^{Cy}) 1.08 (t, 3H, $^{3}J_{HH}$ = 7.1 Hz, CH_3^{Et}).

5b. ^{1}H NMR (DMSO-d_6): δ/ppm = 6.01 (s, 1H, C^2H); 5.61 (s, 5H, Fe^1-Cp), 5.10 (s, 5H, Fe^2-Cp); 4.42 (m, 2H, CH_2^{Et}); 3.92 (s, 3H, OMe); 3.81 (m, 1H, CH^{Cy}); 2.99 (s, 6H, NMe); 2.36-1.57 (m, 8H, CH_2^{Cy}); 1.39 (t, $^{3}J_{HH}$ = 7.1 Hz, 3H, CH_3^{Et}); 1.36-1.32 (m, 2H, CH_2^{Cy}).

5aEt. ^{1}H NMR (DMSO-d_6): δ/ppm = 6.83 (d, $^{3}J_{HH}$ = 9.0 Hz, 2H, C_6H_4); 6.74 (d, $^{3}J_{HH}$ = 9.0 Hz, 2H, C_6H_4); 6.23 (s, 1H, C^2H); 5.65 (s, 5H, Fe^1-Cp), 5.21 (s, 5H, Fe^2-Cp); 4.09-3.84 (m, 4H, CH_2^{Et}); 3.70 (OMe); 3.62 (m, 1H, CH^{Cy}); 3.20 (s, 3H, NMe); 2.37-1.57 (m, 8H, CH_2^{Cy}); 1.43-1.37 (m, 2H, CH_2^{Cy}); 1.36 (t, 3H, $^{3}J_{HH}$ = 6.9 Hz, $OCH_2C\underline{H_3}$); 1.08 (t, 3H, $^{3}J_{HH}$ = 7.1 Hz, $OCOCH_2C\underline{H_3}$).

5.3.2. DMEM-d / DMSO-d_6. Powdered DMEM cell culture medium (1000 mg/L glucose and L-glutamine, without sodium bicarbonate and phenol red; D2902 - Merck) was dissolved in D_2O at a concentration of 10 mg/mL, following the manufacturer's instructions. The resulting deuterated medium ("DMEM-d") was supplemented with 3-(trimethylsilyl)propionic-2,2,3,3-d_4 acid sodium salt (TSP-d_4; 7.35 x 10^{-3} M) as an internal standard[15] and a NaH_2PO_4 / Na_2HPO_4 buffer (0.15 M, pD = 7.5[16]), then stored at 4 °C under N_2 atmosphere. Each iron complex was separately dissolved in DMSO-d_6 and diluted with the DMEM-d solution, to achieve a final DMEM-d/DMSO-d_6 ratio of 2:1 (v/v), in a total volume of 0.75 mL. The final concentrations of the complexes were 2.4 x 10^{-3} (**5a**), 3.8 x 10^{-3} (**5b**), 1.0 x 10^{-3} (**5aEt**), respectively. The mixtures were stirred at ≈ 23 °C for 5 min, filtered through Celite, transferred into NMR tubes, and analyzed by ^{1}H NMR spectroscopy (delay time = 10 s; number of scans = 32).

Subsequently, the samples were incubated at 37 °C for 48h. Additional ^{1}H NMR spectra were recorded after cooling to room temperature and filtering again through Celite. The percentage of residual complex was calculated by comparing the integrals of the reference TSP-d_4 signal (δ = 0.0 ppm) at time zero and after 48 hours, with the integral of the $C^{2}H$ signal normalized to 1.0. Stability data are compiled in Table S13, and the corresponding ^{1}H NMR spectra are shown in Figures S80-S82.

Table S13. Solubility in D_2O (^{1}H NMR spectroscopy, Me_2SO_2 as internal standard, room temperature); partition coefficients (Log P_{ow}, UV-Vis spectroscopy, room temperature); residual percentage of complexes in DMEM-d/DMSO-d_6 mixture (2:1 *v/v*) after 48h incubation at 37 °C (^{1}H NMR spectroscopy, TSP-d_4 as internal standard).

Complex	Solubility (mol·L^{-1})	Log P_{ow}	Stability in DMEM-d / DMSO-d_6 (%)
5a	5 x 10^{-5}	0.64 ± 0.03	80
5b	7 x 10^{-4}	0.11 ± 0.03	89
5aEt	4 x 10^{-5}	0.71 ± 0.09	76

Table S14. Residual percentage of the complexes at specified time intervals in DMSO-d_6 solutions stored at room temperature, determined by ^{1}H NMR spectroscopy. Me_2SO_2 was used as an internal standard.

Complex	2h	24h	48h
5a	99	95	92
5b	100	98	97
5aEt	97	97	94

Figure S74. ^{1}H NMR spectrum (501 MHz, D_2O) of **5a** for D_2O solubility determination; the green box marks the C^2H signal of **5a** (δ = 6.26 ppm), which was set to an integral value of 1.0, while the orange box marks the Me_2SO_2 standard signal (δ = 3.10 ppm). Inset: integration of the Me_2SO_2 standard signal

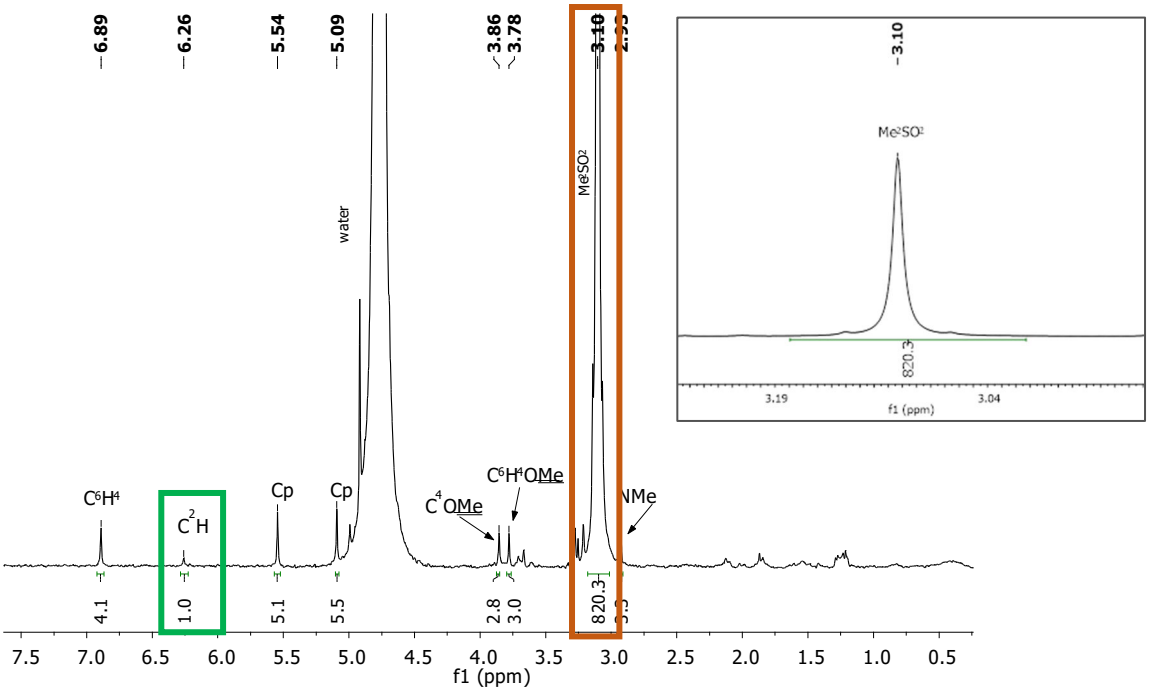

Figure S75. ^{1}H NMR spectrum (501 MHz, D_2O) of **5b** for D_2O solubility determination; the green box marks the C^2H signal of **5b** (δ = 6.13 ppm), which was set to an integral value of 1.0, while the orange box marks the Me_2SO_2 standard signal (δ = 3.10 ppm). Inset: integration of the Me_2SO_2 standard signal

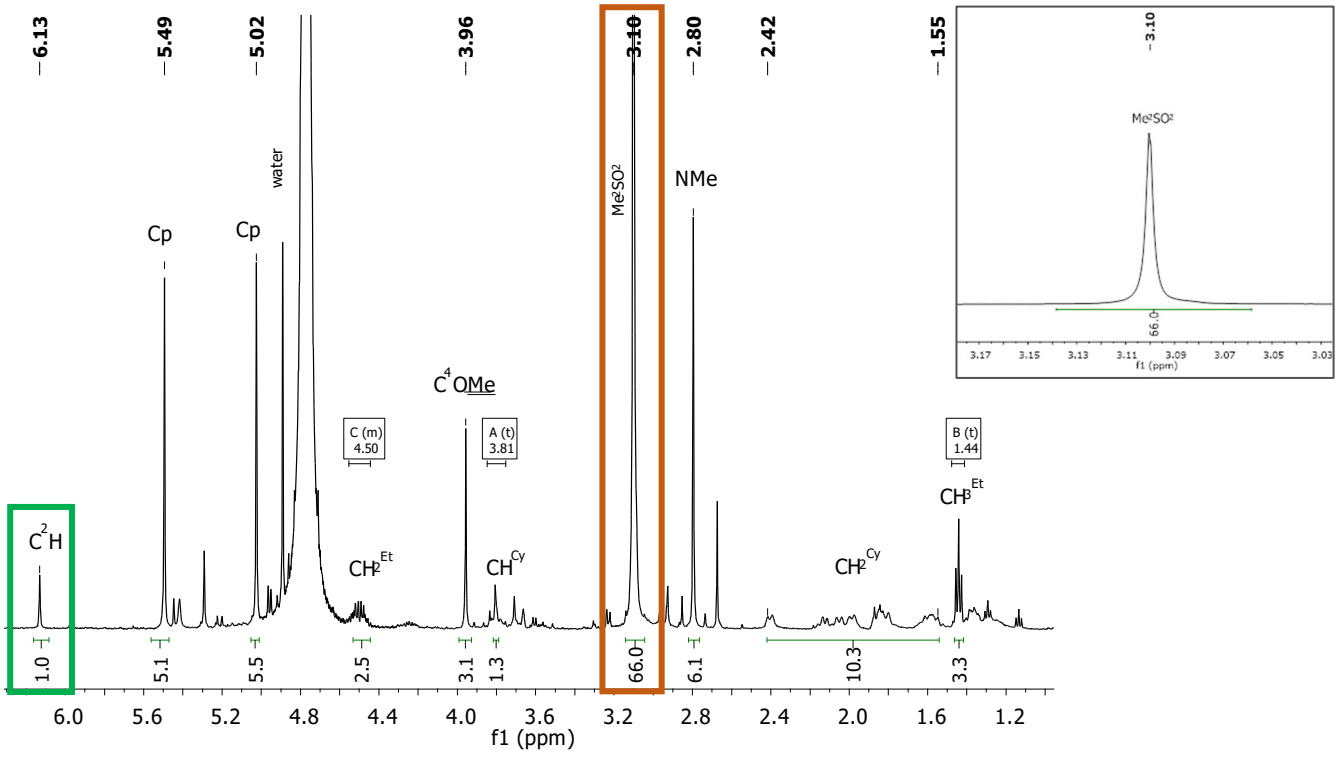

Figure S76. ^{1}H NMR spectrum (501 MHz, D_2O) of **5aEt** for D_2O solubility determination; the green box marks the C^2H signal of **5aEt** (δ = 6.28 ppm), which was set to an integral value of 1.0, while the orange box marks the Me_2SO_2 standard signal (δ = 3.10 ppm). Inset: integration of the Me_2SO_2 standard signal

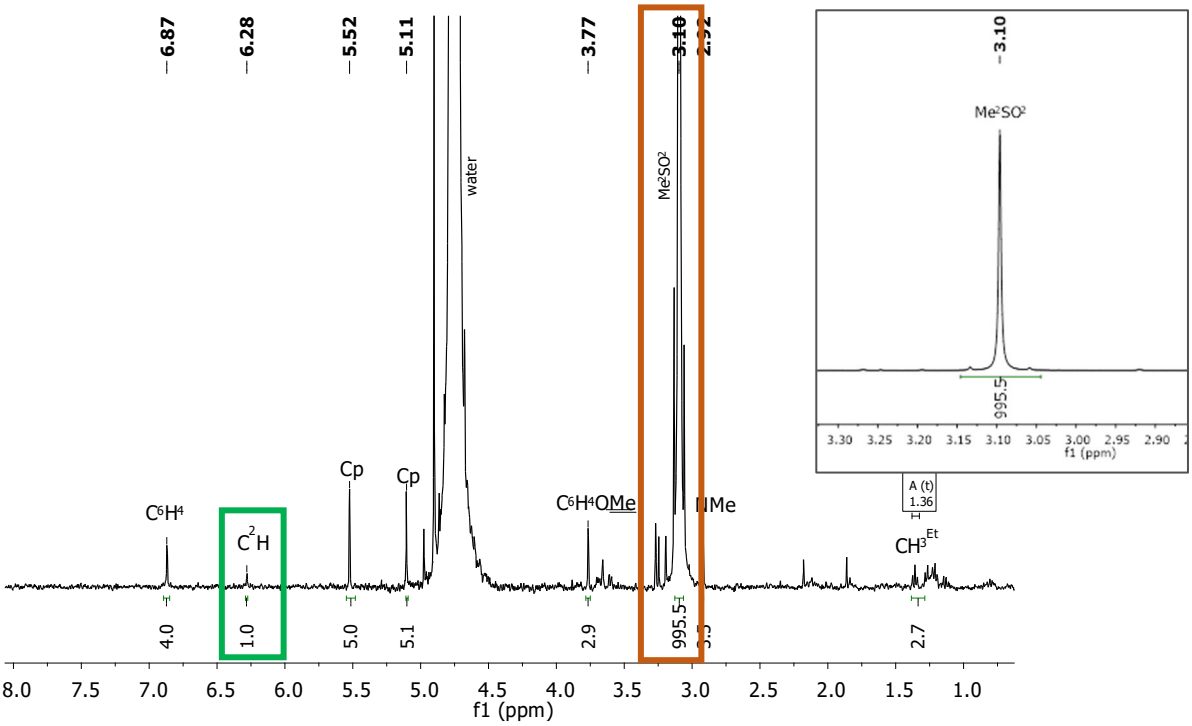

Figure S77. ^{1}H NMR spectrum (501 MHz, DMSO-d_6) of **5a** with Me_2SO_2 as internal standard (δ = 2.99 ppm), recorded at time zero

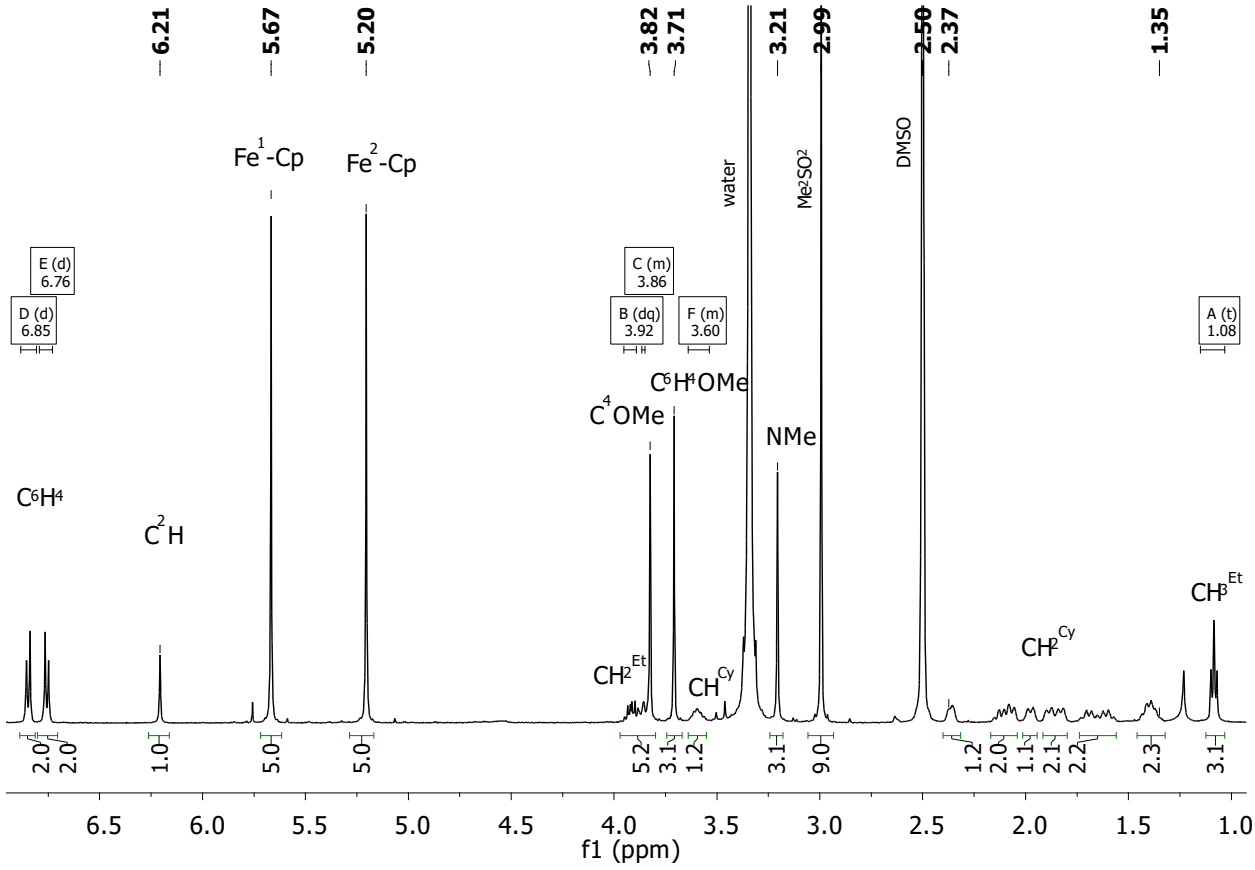

Figure S78. ^{1}H NMR spectrum (501 MHz, DMSO-d_6) of **5b** with Me_2SO_2 as internal standard (δ = 2.99 ppm), recorded at time zero

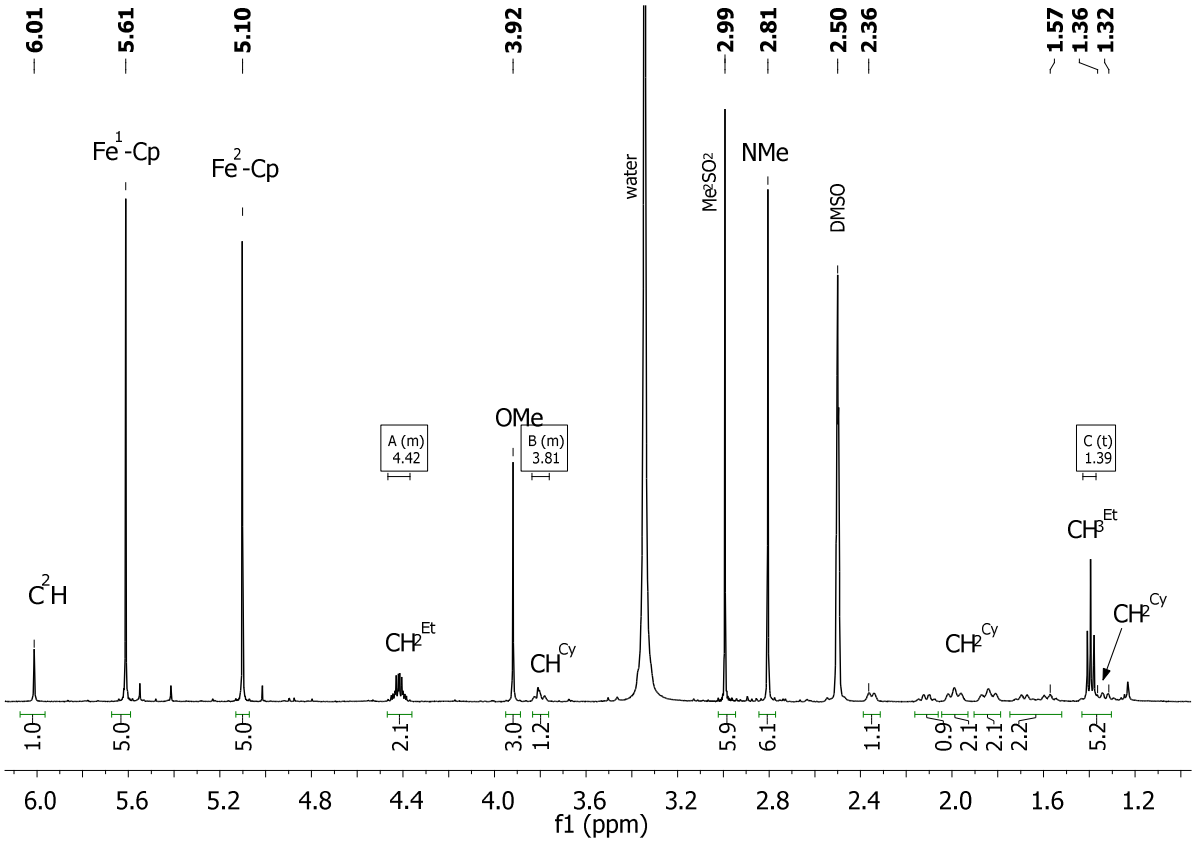

Figure S79. ^{1}H NMR spectrum (501 MHz, DMSO-d_6) of **5aEt** with Me_2SO_2 as internal standard (δ = 2.99 ppm), recorded at time zero

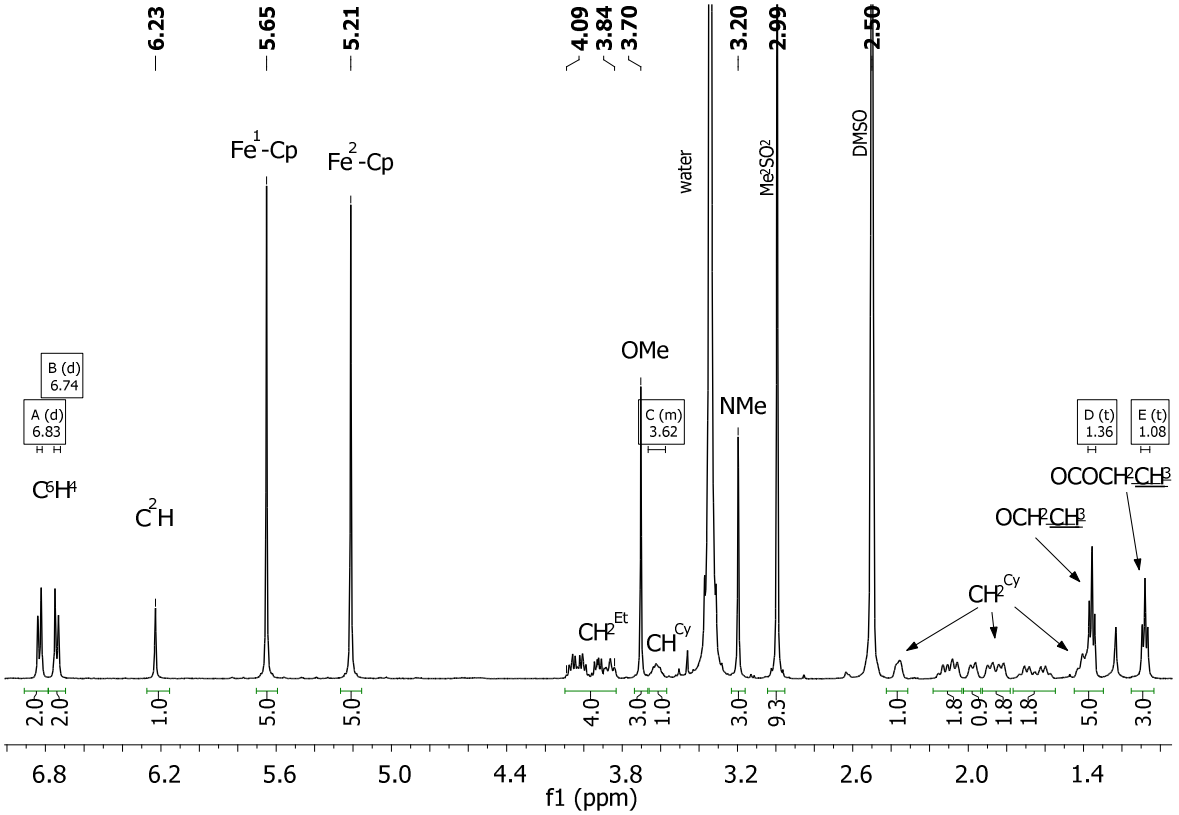

Figure S80. Comparative view of ^{1}H NMR spectra of **5a** (501 MHz, DMEM-d/DMSO-d_6 2:1 v/v). **A)** Spectrum recorded at 0 h; **B)** Spectrum recorded after 48 h incubation at 37 °C. The green box marks the $C^{2}H$ signal of **5a** (δ = 6.26 ppm), set to an integral value of 1.0. The orange box marks the TSP-d_4 standard signal (δ = 0.00 ppm). The stability of **5a** was estimated by comparing the integrals for the standard signal at 0 h and 48 h.

A)

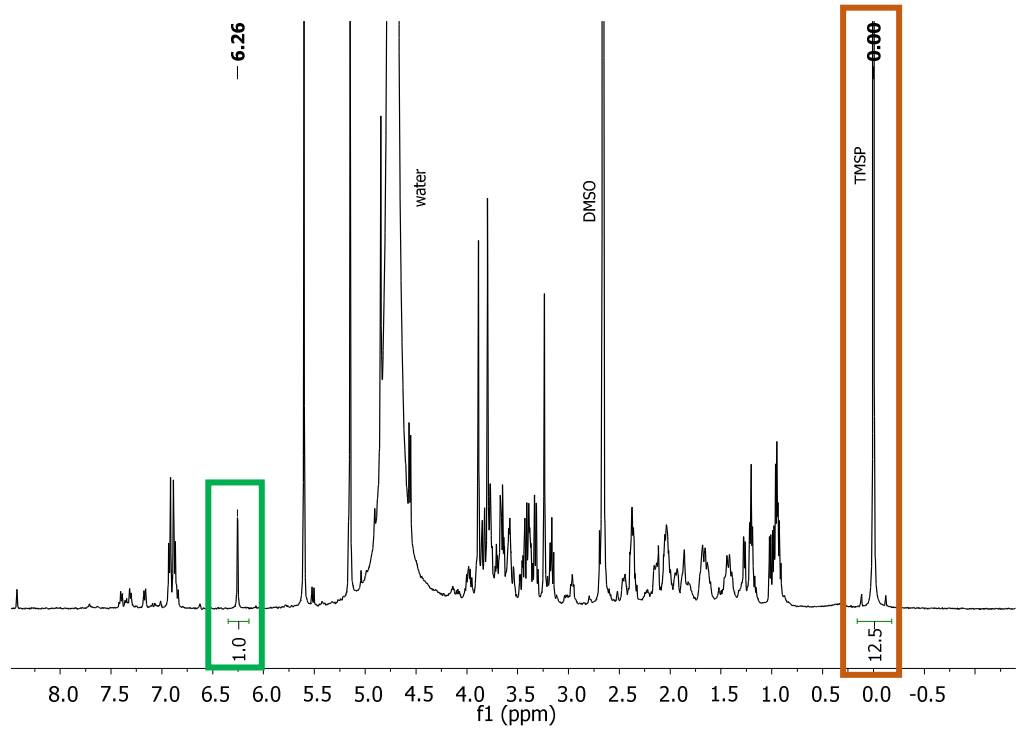

B)

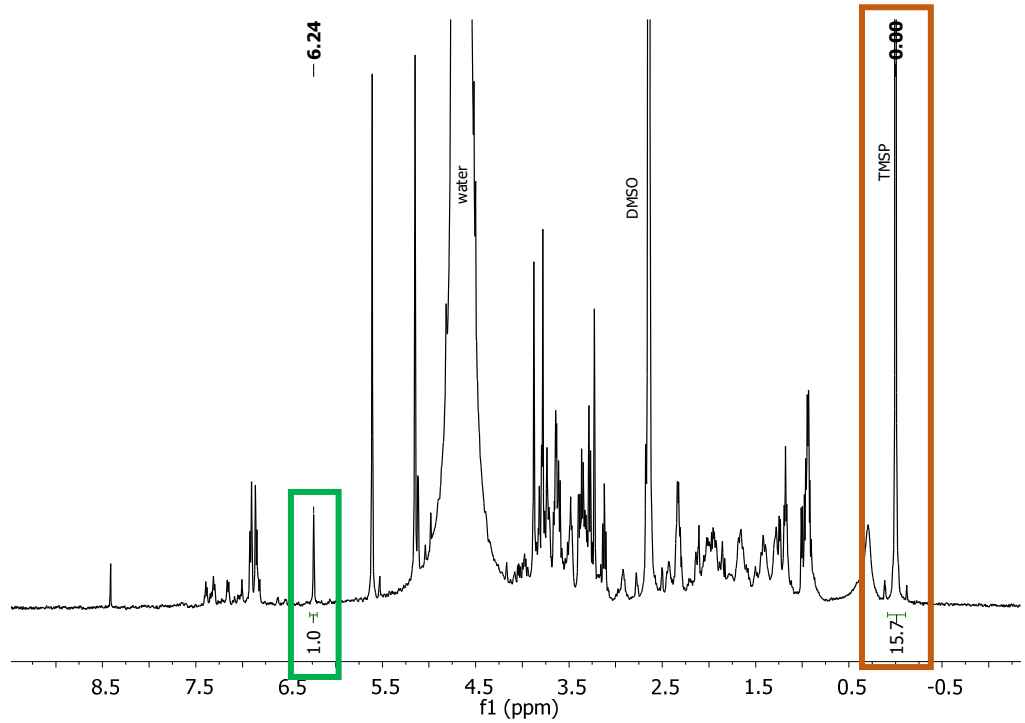

Figure S81. Comparative view of ^{1}H NMR spectra of **5b** (501 MHz, DMEM-d/DMSO-d_6 2:1 v/v). **A)** Spectrum recorded at 0 h; **B)** Spectrum recorded after 48 h incubation at 37 °C. The green box marks the $C^{2}H$ signal of **5b** (δ = 6.12 ppm), set to an integral value of 1.0. The orange box marks the TSP-d_4 standard signal (δ = 0.00 ppm). The stability of **5b** was estimated by comparing the integrals for the standard signal at 0 h and 48 h.

A)

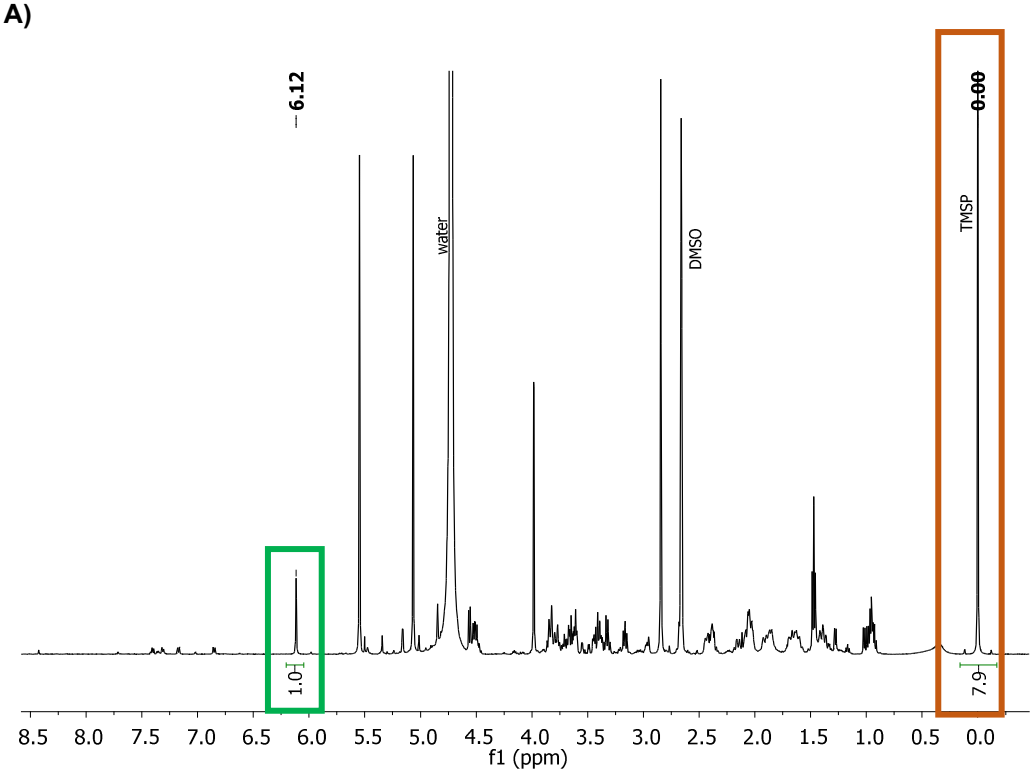

B)

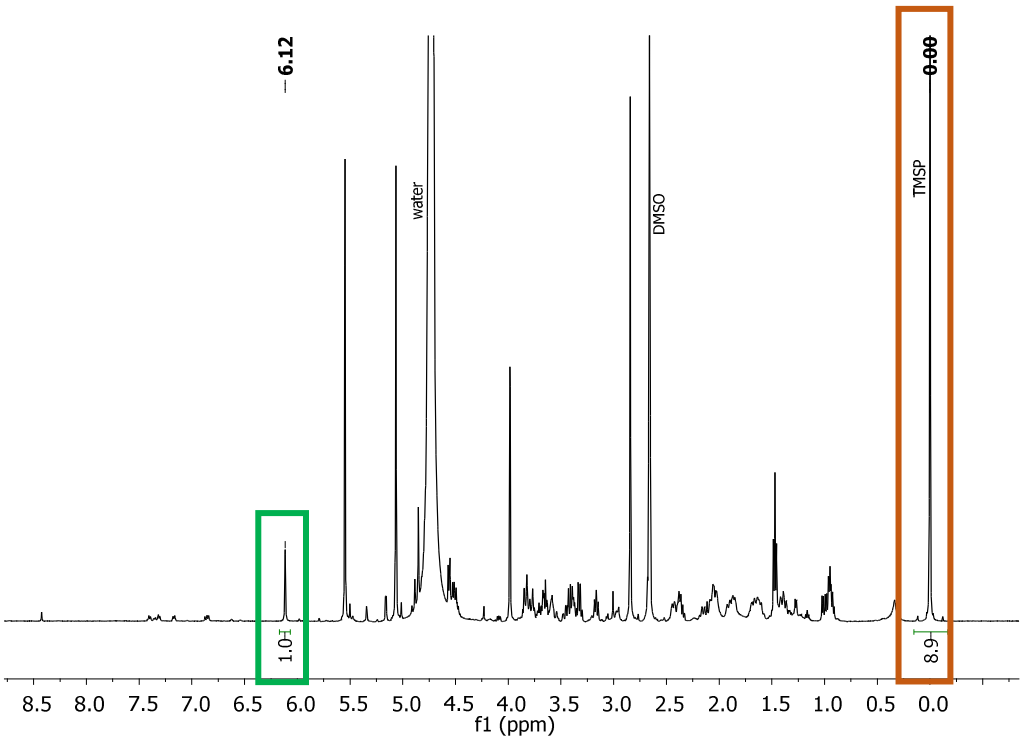

Figure S82. Comparative view of ^{1}H NMR spectra of **5aEt** (501 MHz, DMEM-d/DMSO-d_6 2:1 v/v). **A)** Spectrum recorded at 0 h; **B)** Spectrum recorded after 48 h incubation at 37 °C. The green box marks the $C^{2}H$ signal of **5aEt** (δ = 6.28 ppm), set to an integral value of 1.0. The orange box marks the TSP-d_4 standard signal (δ = 0.00 ppm). The stability of **5aEt** was estimated by comparing the integrals for the standard signal at 0 h and 48 h.

A)

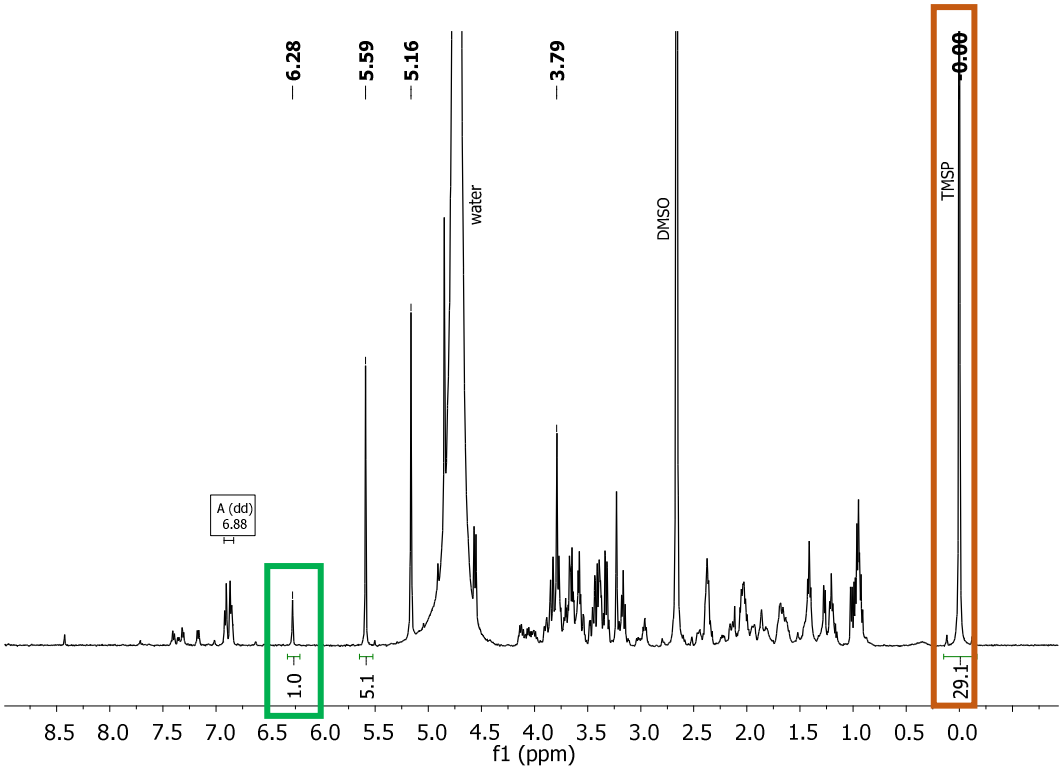

B)

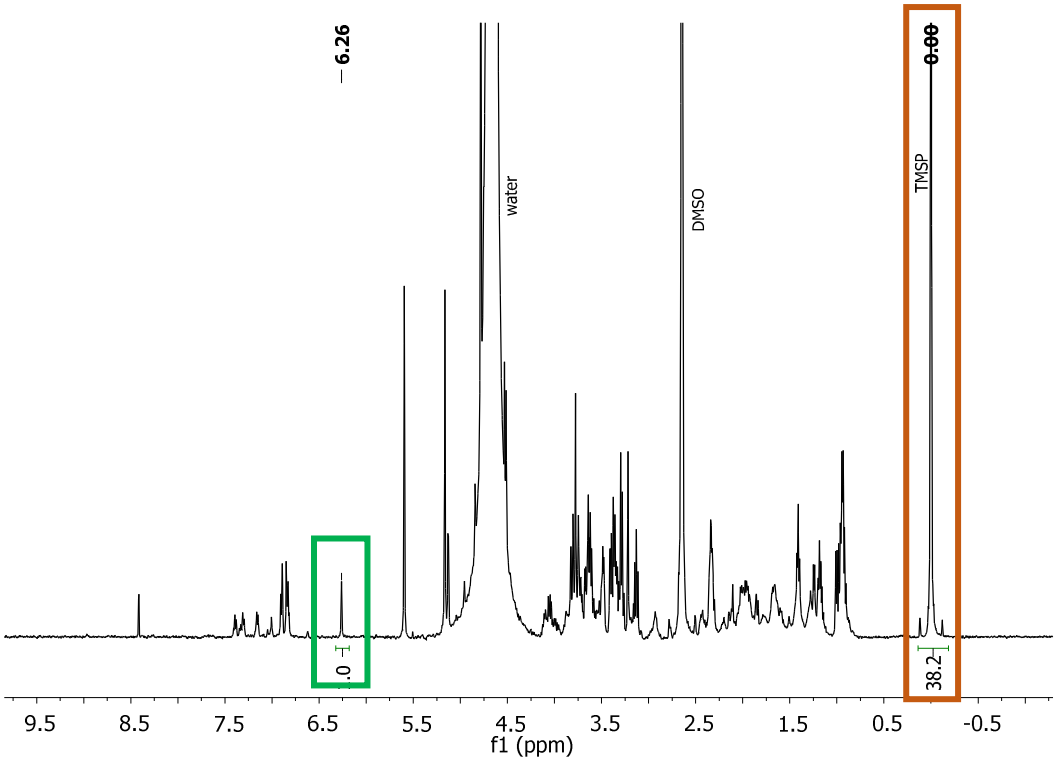

5.4. NMR study of the 5aEt / GSH system

A solution of **5aEt** in DMSO-d_6 (10 mM) was mixed with a solution of glutathione (GSH) in D_2O (25 mM), in a 1:2 volume ratio, affording a final mixture (V_{tot} = 0.75 mL) containing a 5:1 molar ratio of GSH to **5aEt** (final **5aEt** concentration = 3.3 mM). ^1H NMR spectra were recorded for this solution, for an analogous solution of **5aEt** lacking GSH, and for a solution of GSH in D_2O (scans = 16, delay time = 10 s). The samples were then kept at 37 °C in the dark. After 48 h, the three solutions were filtered through cotton, and ^1H NMR spectra were recorded again.

Figure S83A. ^1H NMR spectra (7.0 – 1.5 ppm range) of mixtures

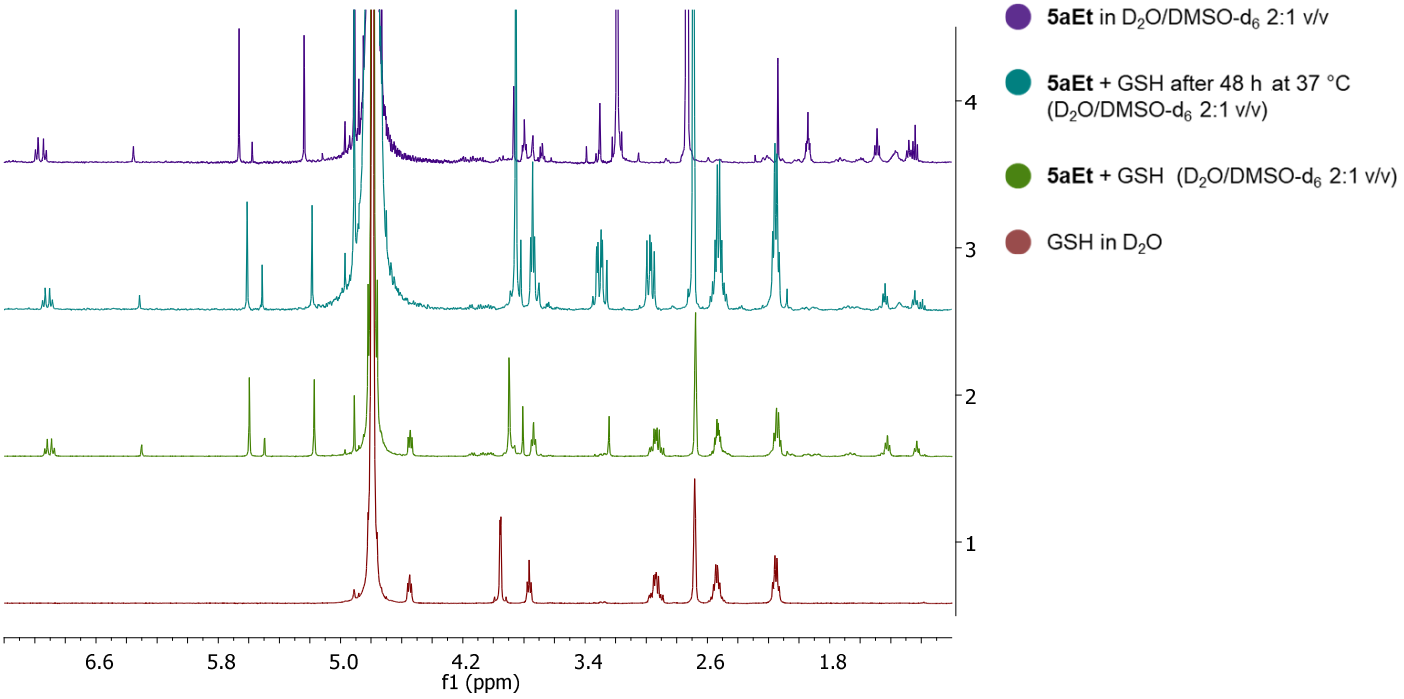

Figure S83B. ^1H NMR spectra (5.0 – 1.0 ppm range) of mixtures

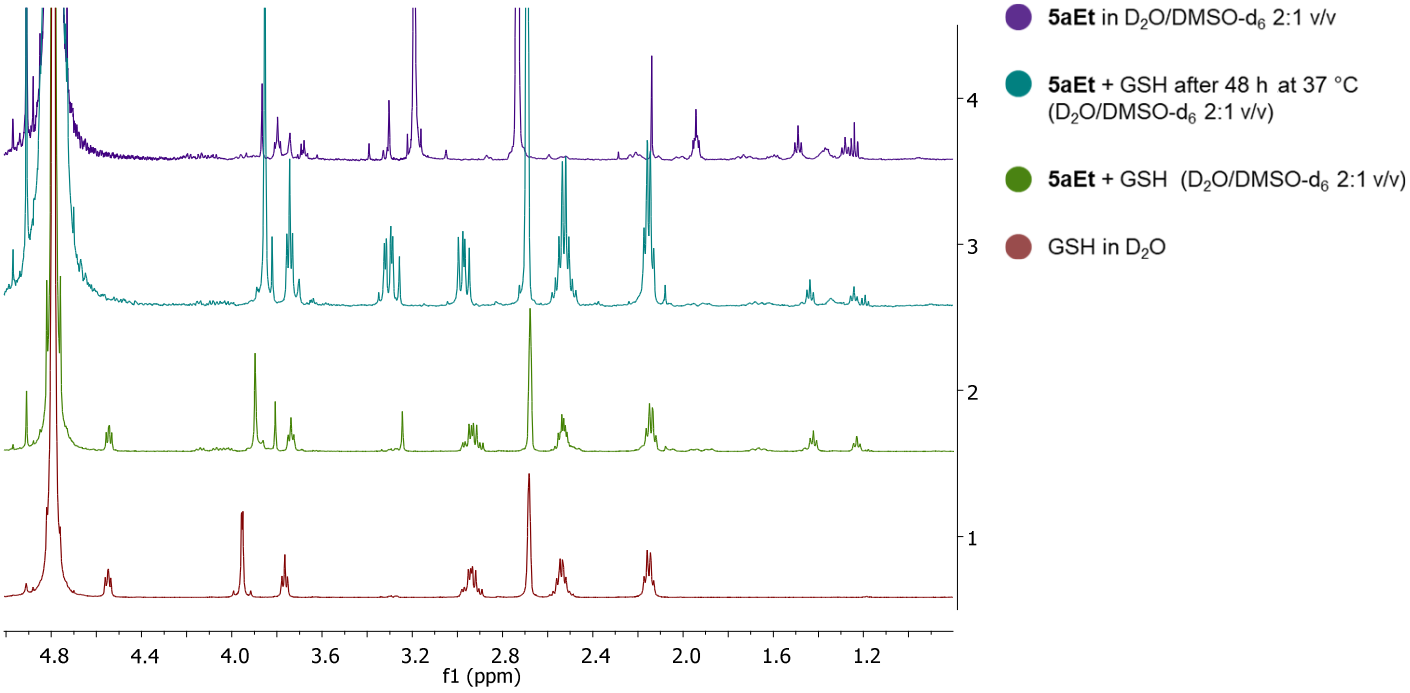

Figure S83C. Comparative view of the ^{1}H NMR spectra of GSH + **5aEt** (5:1 ratio in DMSO-d_6 / D_2O 2:1 v/v) after 48h incubation at 37 °C (top) and at time zero (bottom)

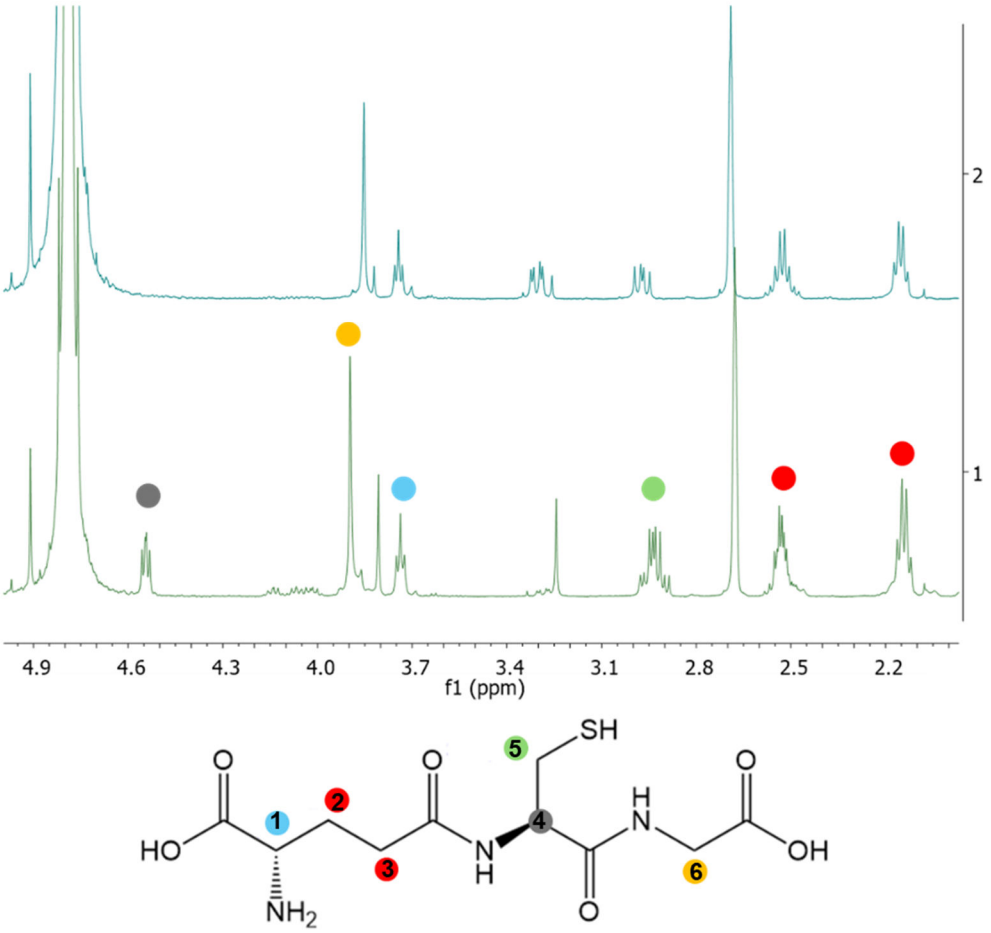

Overall, the obtained spectra indicate no interaction between **5aEt** and GSH after 48 h, since the ferrabenzene complex undergoes degradation analogous to that observed in the absence of GSH. However, partial oxidation of GSH to GSSG can be noticed, likely caused by the oxidizing effect of DMSO.[17] Variations in the GSH signals are highlighted in Figure S83C. Specifically, while the signals of $H^{1\text{-}3}$ (blue and red) remain unvaried and the signal of H^{6} (yellow) shows only a slight shift, the multiplet assigned to H^{5} (green) is split into two double triplets and the H^{4} signal (grey) disappears entirely (presumably either overlapped with the residual water signal or involved in deuterium exchange).

5.5. UV-Vis stability studies

Compounds **5a**, **5b**, and **5aEt** were incubated with nicotinamide adenine dinucleotide (NADH, 180 µM in water), glutathione (GSH, 5 mM in water) and 10% fetal calf serum (FBS), to evaluate their stability under biologically relevant conditions. Each compound was first prepared as a 10 mM stock solution in DMSO, and then diluted with the corresponding medium (H_2O, NADH, GSH, or 10% FBS) to achieve a final concentration of 100 µM. Samples were incubated at 37 °C in the dark and analyzed by UV–Vis spectroscopy at 0.5, 1, 2, 4, 24, 48, and 72 h. NADH and GSH concentrations were selected to mimic physiologically relevant intracellular and extracellular environments, respectively. As a preliminary step, the UV–Vis spectra of GSH, NADH, 10% FBS, and the individual complexes (**5a**, **5b**, and **5aEt**) in water were recorded as references (Figure S84). The intrinsic stability of the complexes, GSH, NADH, and FBS was then monitored over 72 h (Figure S85). The UV–Vis spectra of **5a**, **5b**, and **5aEt** in H_2O demonstrated minor changes during the incubation, indicating good intrinsic stability (Table S16). GSH exhibited no UV absorption above 300 nm, FBS showed no significant spectral changes over 72 h, and NADH remained stable for the first 24 h, but displayed signs of degradation at 48 h and 72 h. When incubated with 5 mM GSH and 10% FBS, all complexes exhibited only minor spectral variations over 72 h, suggesting limited or no reactivity under the investigated conditions (Figures S86-S88). However, a gradual decrease in absorbance was observed in the presence of NADH, indicating potential interaction or partial degradation.

Figure S84. a) UV–vis absorption spectra of 180 µM NADH, 5 mM GSH, and 10% FBS aqueous solutions. b) UV–vis absorption spectra of complexes in H_2O (100 µM)

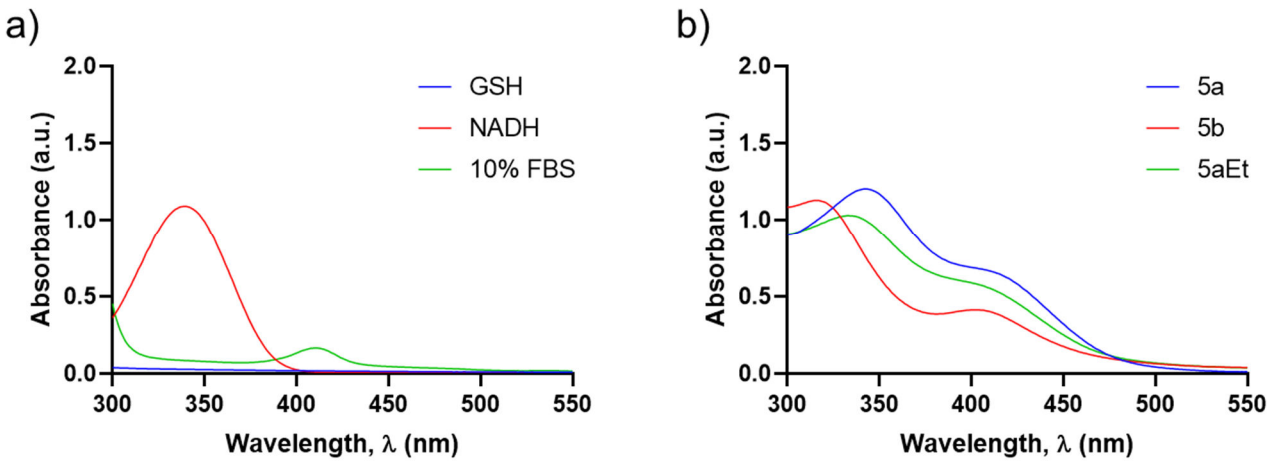

Figure S85. UV–vis absorption spectra of 180 μM NADH, 5 mM GSH, and 10% FBS, recorded over 72 h of incubation at 37 °C in the dark

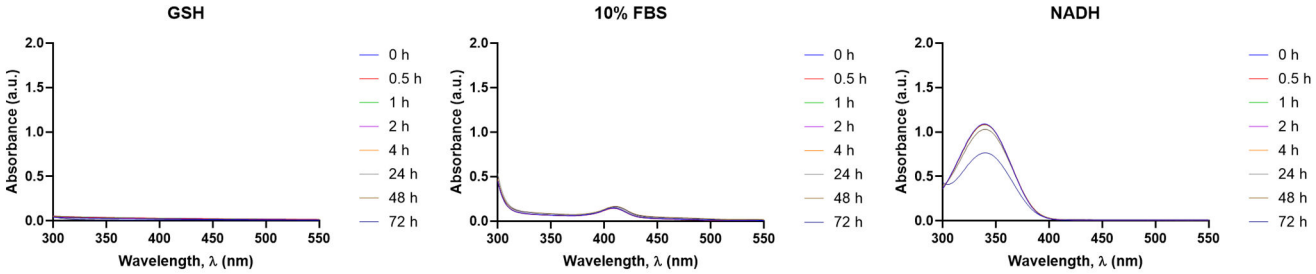

Figure S86. UV–vis absorption spectra of **5a** in H_2O, 180 μM NADH, 5 mM GSH, and 10% FBS, recorded over 72 h of incubation at 37 °C in the dark

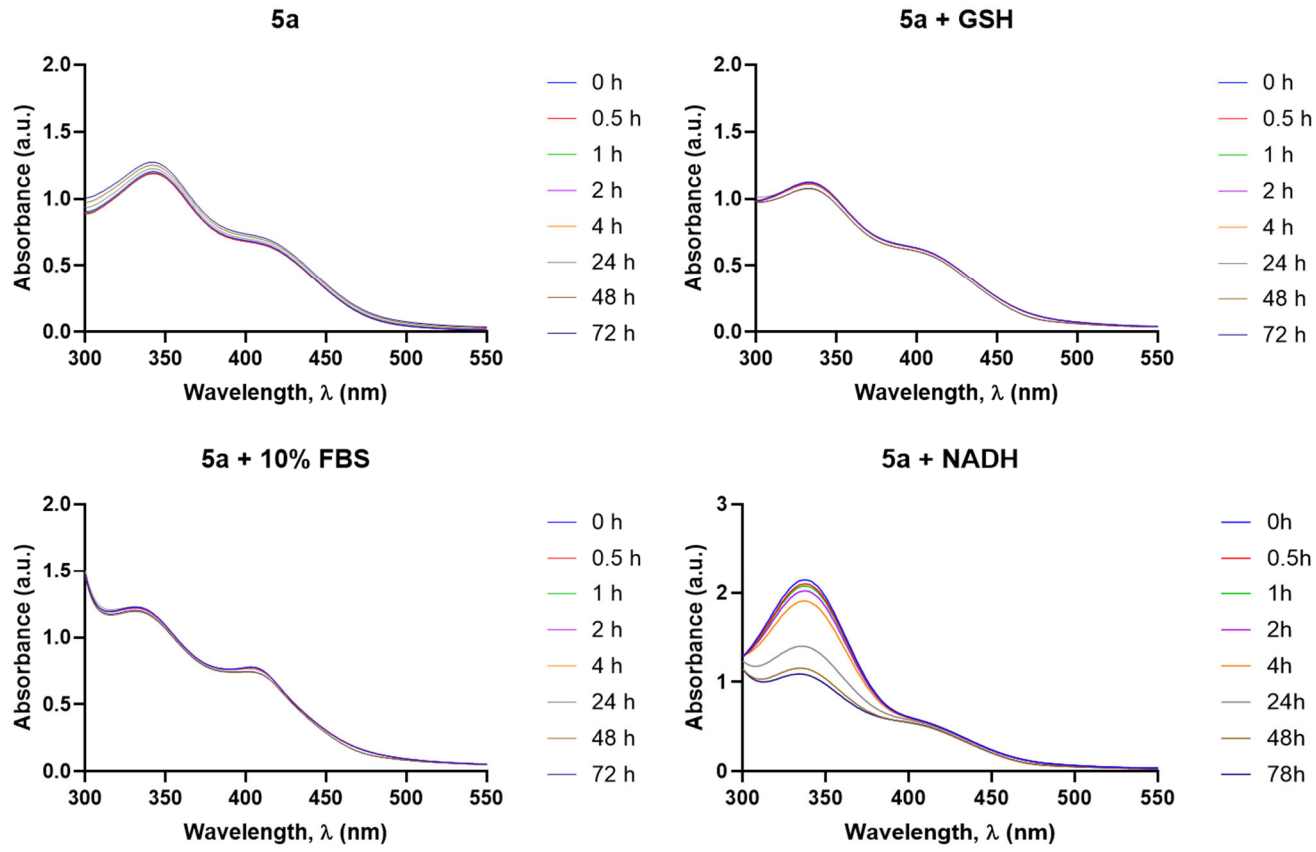

Figure S87. UV–vis absorption spectra of **5b** in 180 µM NADH, 5 mM GSH, and 10% FBS, recorded over 72 h of incubation at 37 °C in the dark

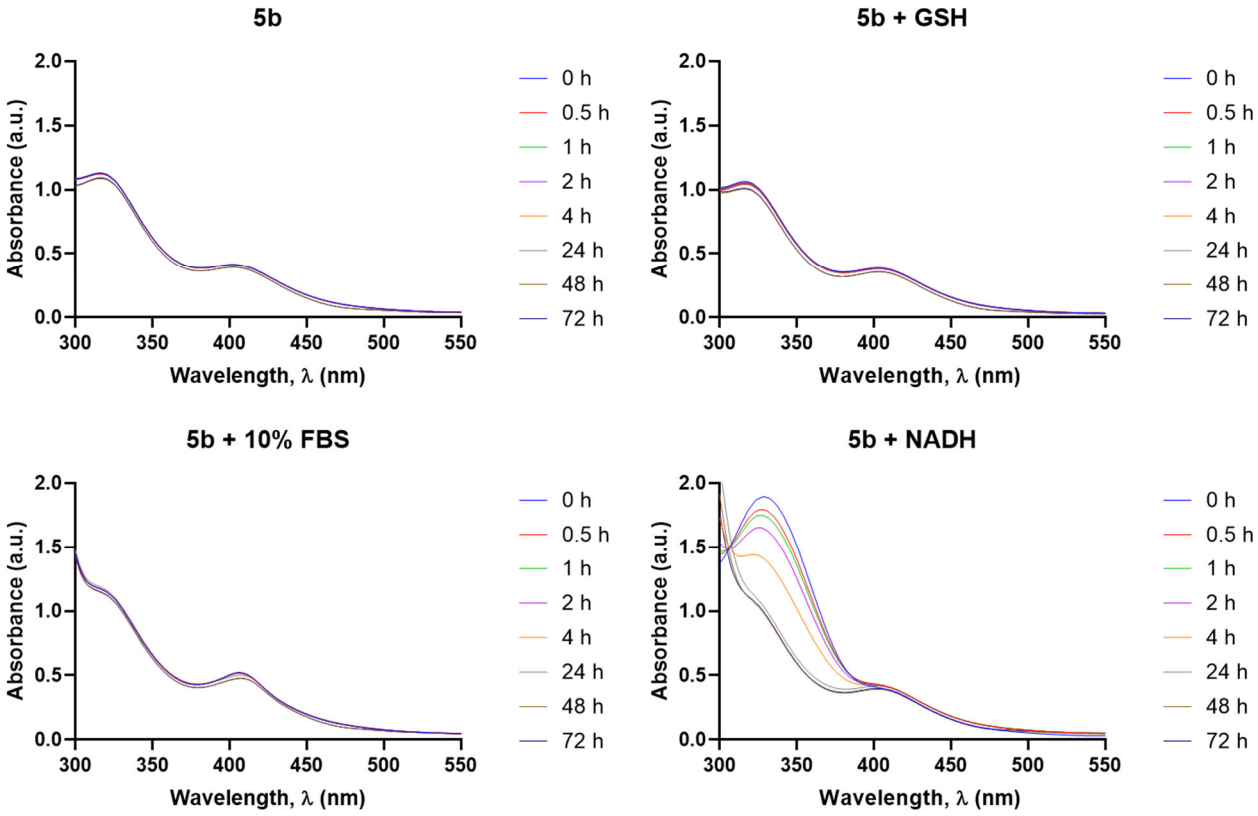

Figure S88. UV–vis absorption spectra of **5aEt** in 180 µM NADH, 5 mM GSH, and 10% FBS, recorded over 72 h of incubation at 37 °C in the dark

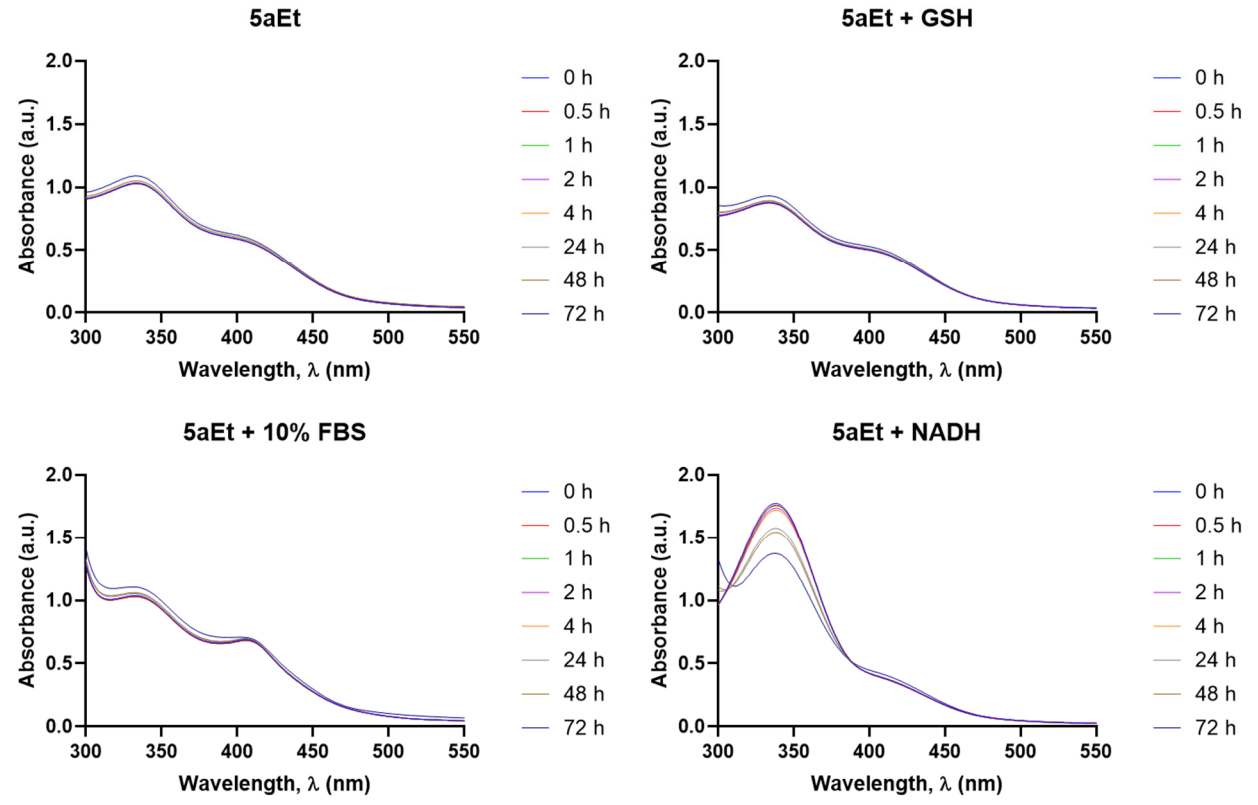

5.6. High-resolution ESI-QTOF mass spectrometry (HR-ESI-QTOF-MS) analysis

Prior to FIA-ESI-Q-ToF analysis, aliquots of freshly prepared (< 5 h) solutions of **5a**, **5b** and **5aEt** (500 ppm in DMSO, H_2O/DMSO 95:5 v/v and DMEM/DMSO 95:5 v/v) were diluted with water to a final concentration of approximately 1 μM, and filtered through PTFE filters (0.45 μm pores, Agilent). The starting solutions were then incubated at 37 °C for 48 h. After incubation, the same dilution and filtration procedure was repeated for FIA-ESI-Q-ToF analysis.

The Flow injection analyses (FIA) using ESI-Q/ToF were performed on a 1200 Infinity HPLC system (Agilent Technologies, USA), equipped with a Jet Stream ESI interface and coupled to a 6530 Infinity Q-ToF tandem mass spectrometer (Agilent Technologies). HPLC–MS grade acetonitrile (Carlo Erba, Italy) was used as the mobile phase at a flow rate of 0.2 mL/min (total run time: 3 min). Injection volume was 0.20 μL. The ESI source was operated under the following conditions: drying gas (N_2, purity >98%) at 350 °C and 10 L/min; capillary voltage: 4.5 kV; nozzle voltage: 1 kV; nebulizer pressure: 35 psig; sheath gas (N_2, purity >98%) at 375 °C and 11 L/min. The fragmentor voltage was set to 50 V, skimmer to 65 V, and OCT 1 RF to 750 V. High resolution MS spectra were acquired in positive mode in the range 100-1700 m/z; the mass axis was calibrated daily using the Agilent tuning mix HP0321 (Agilent Technologies) prepared in acetonitrile and water. Data analysis was performed using Agilent Mass Hunter 10.0 software (Agilent Technologies). For semi-quantitative analysis, peak areas of the complexes were integrated from the extracted ion chromatograms corresponding to the molecular ions identified using the Find by Formula algorithm, based on high-resolution MS data (mass tolerance <10 ppm). The obtained data are summarized in Table S15, and the corresponding MS spectra are reported in Figures S89-S95.

Table S15. HR-ESI-QTOF-MS peak areas of complexes in different solvents at time 0 and after 48 h incubation at 37 °C, and corresponding residual percentages of intact complexes.

Complex	Solvent	Initial peak area (average)	Final peak area (average)	% after 48h
5a	H_2O/1% DMSO	45.780.085	16.811.851	**37**
	DMEM/1% DMSO	47.243.210	24.711.804	**52**
5b	H_2O/1% DMSO	50.973.502	52.416.282	**100**
	DMEM/1% DMSO	48.312.798	43.439.927	**90**
5aEt	H_2O/1% DMSO	38.633.814	11.877.986	**31**
	DMEM/1% DMSO	48.264.338	16.412.612	**34**
	100% DMSO	66.210.624	46.588.063	**70**

Figure S89. HR-ESI-QTOF-MS spectra of complex **5aEt** in DMSO at time zero (**A**) and after 48 h incubation at 37 °C (**B**)

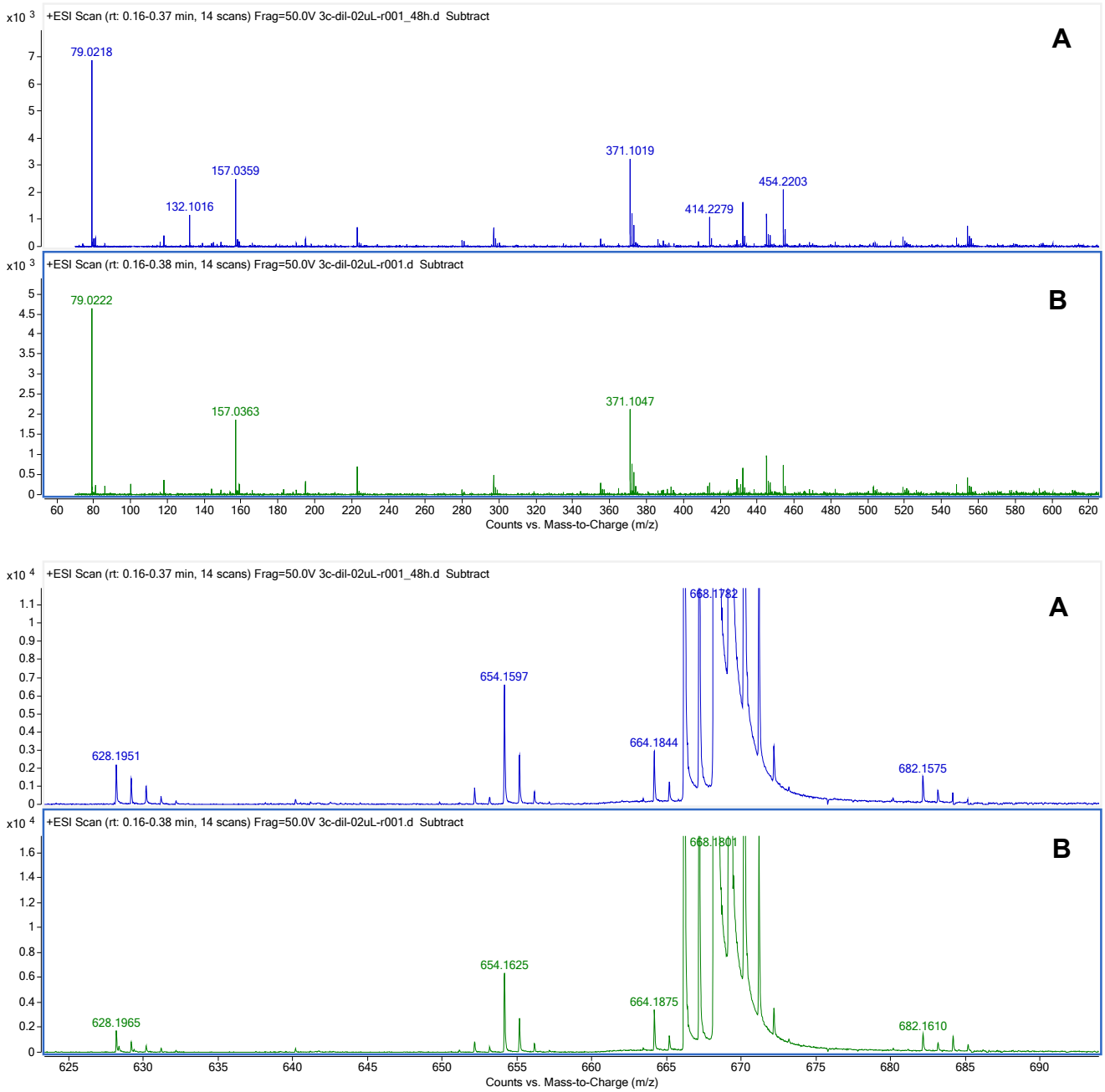

Figure S90. HR-ESI-QTOF-MS spectra of complex **5a** in H_2O/DMSO (9:1 v/v) at time zero (**A**) and after 48 h incubation at 37 °C (**B**). Panel **C**: magnified view of the molecular ion peak

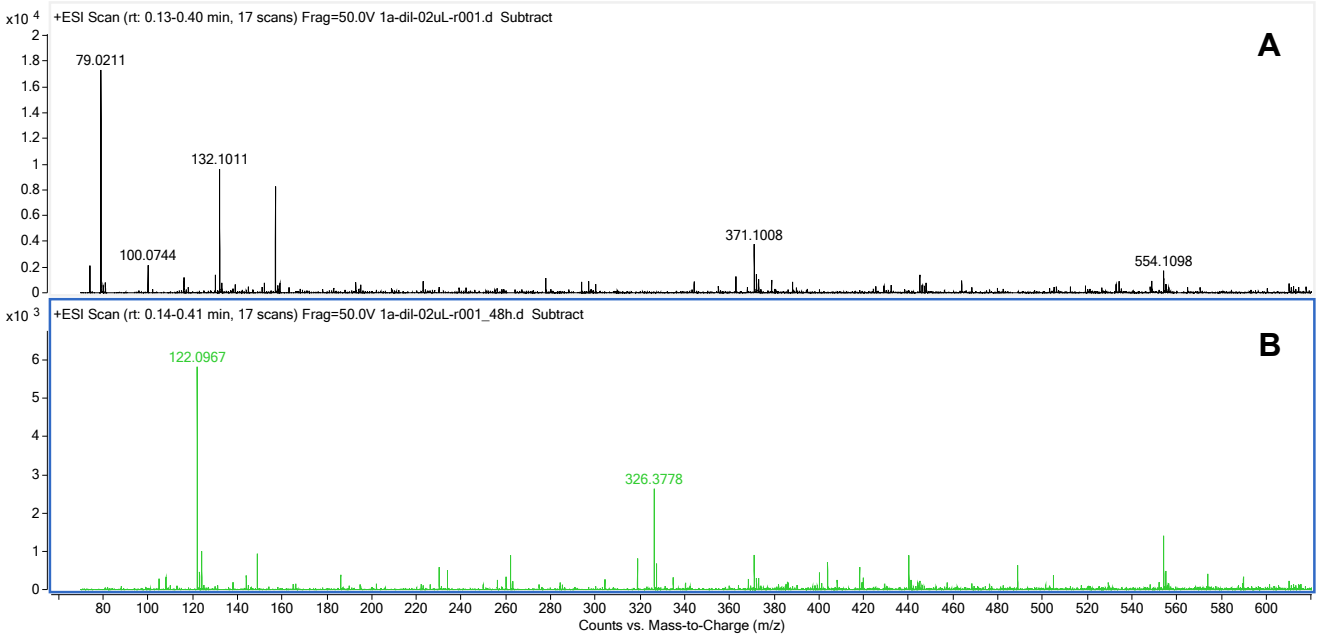

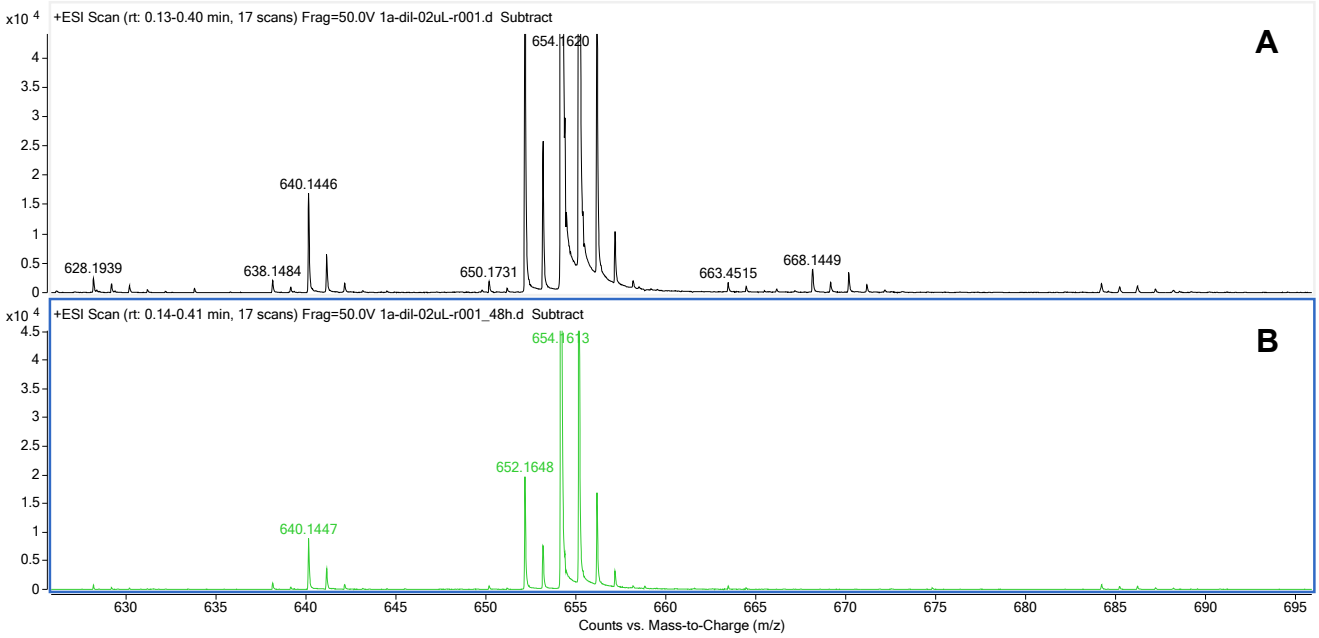

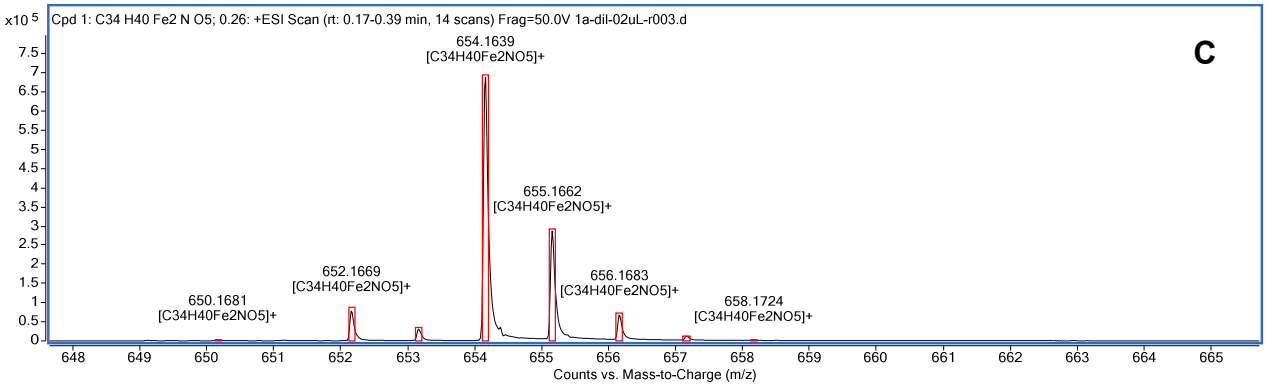

Figure S91. HR-ESI-QTOF-MS spectra of complex **5b** in H_2O/DMSO (9:1 v/v) at time zero (**A**) and after 48 h incubation at 37 °C (**B**). Panel **C**: magnified view of the molecular ion peak

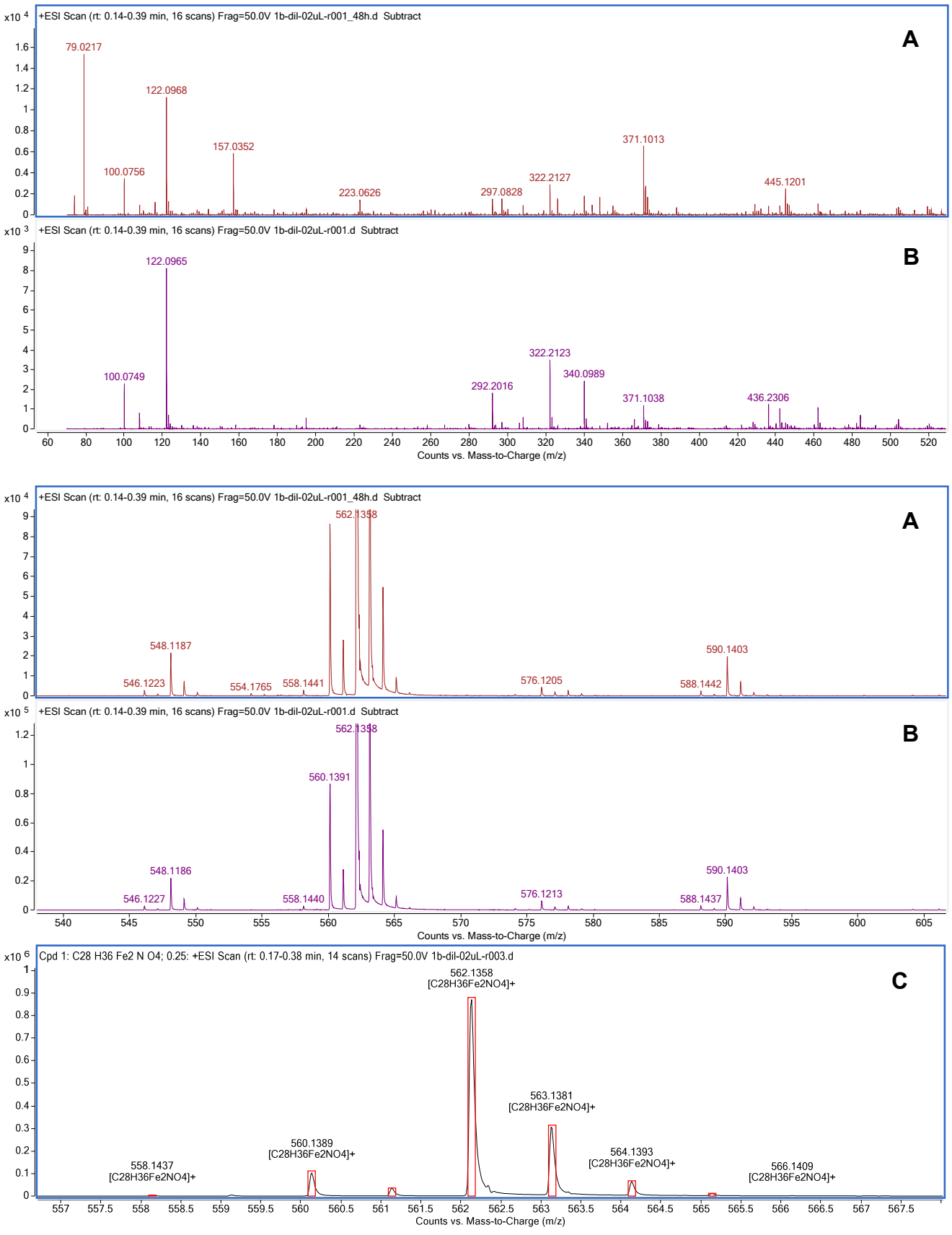

Figure S92. HR-ESI-QTOF-MS spectra of complex **5aEt** in H_2O/DMSO (9:1 v/v) at time zero (**A**) and after 48 h incubation at 37 °C (**B**). Panel **C**: magnified view of the molecular ion peak

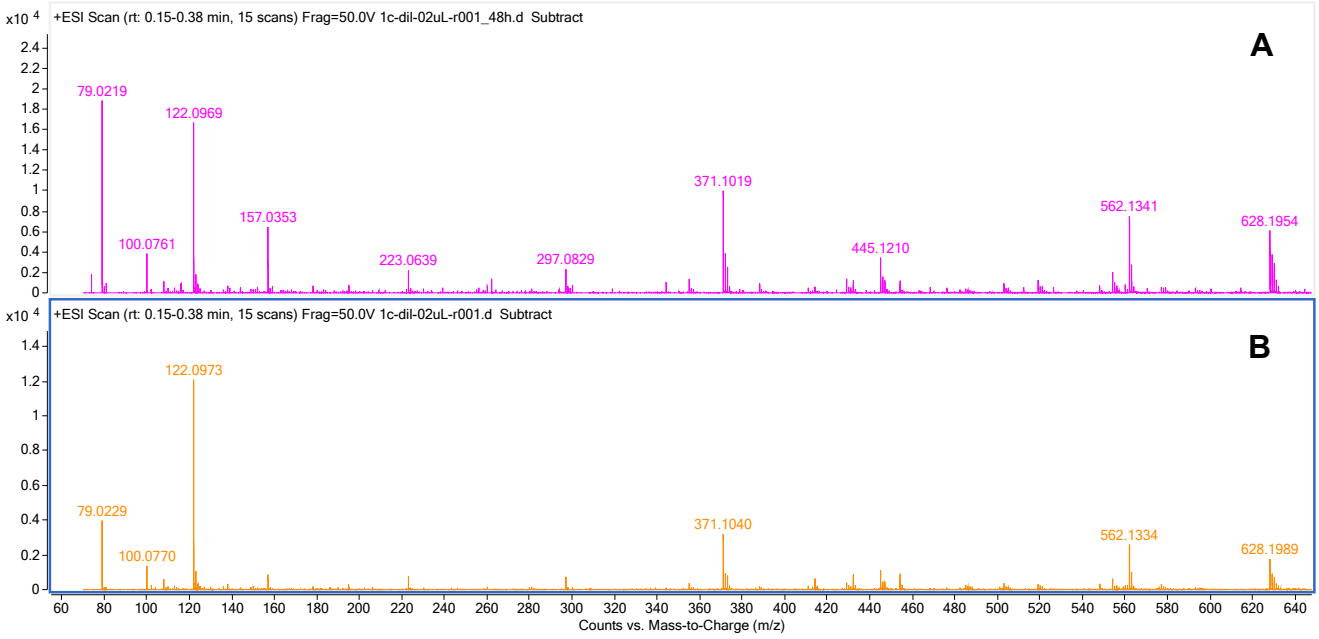

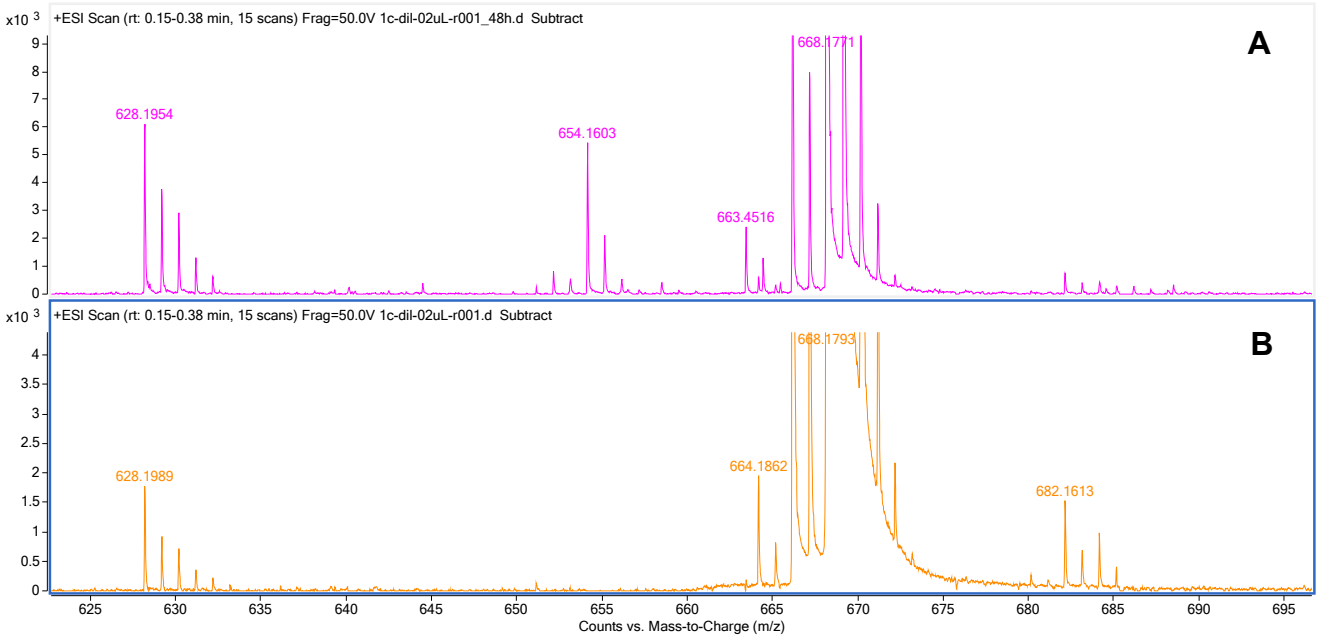

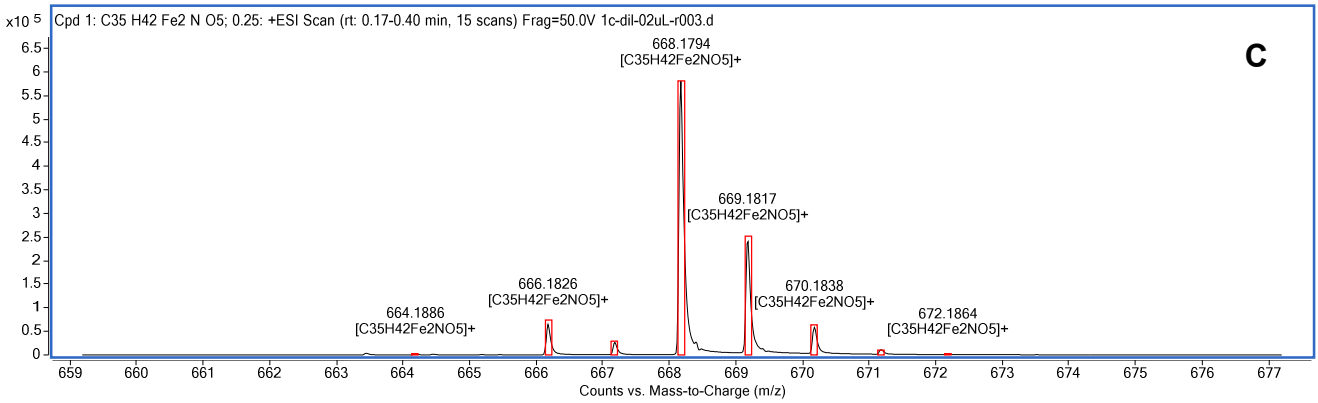

Figure S93. HR-ESI-QTOF-MS spectra of complex **5a** in DMEM/DMSO (9:1 v/v) at time zero (**A**) and after 48 h incubation at 37 °C (**B**)

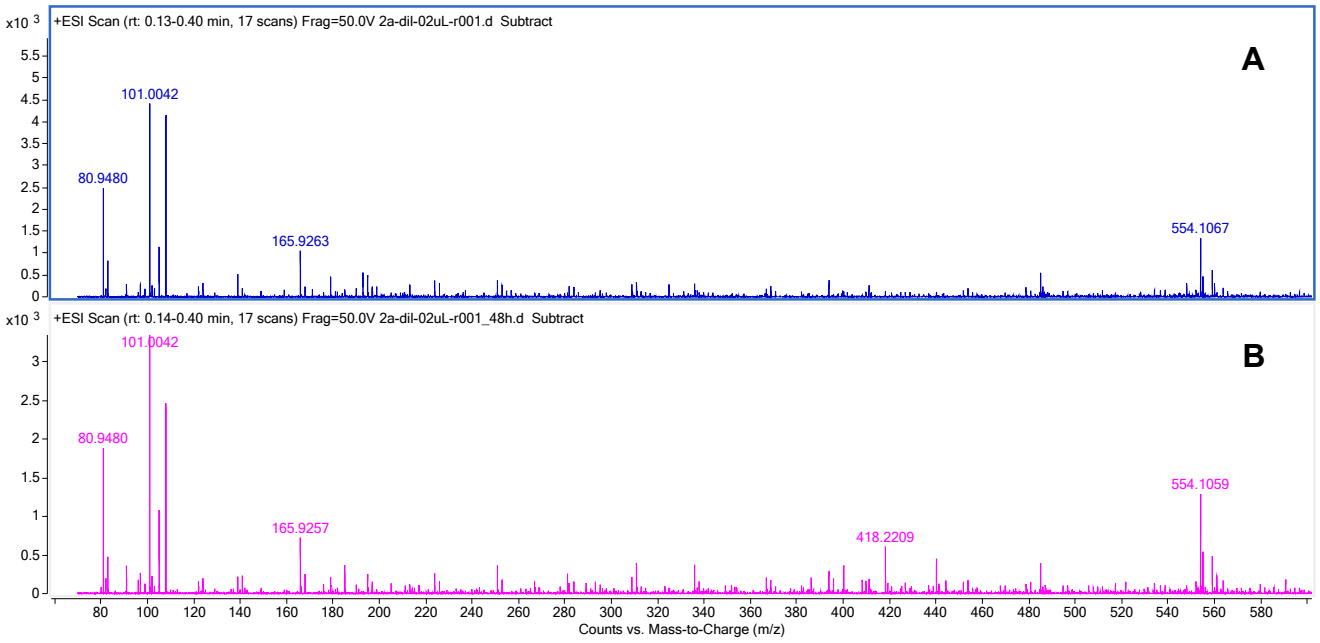

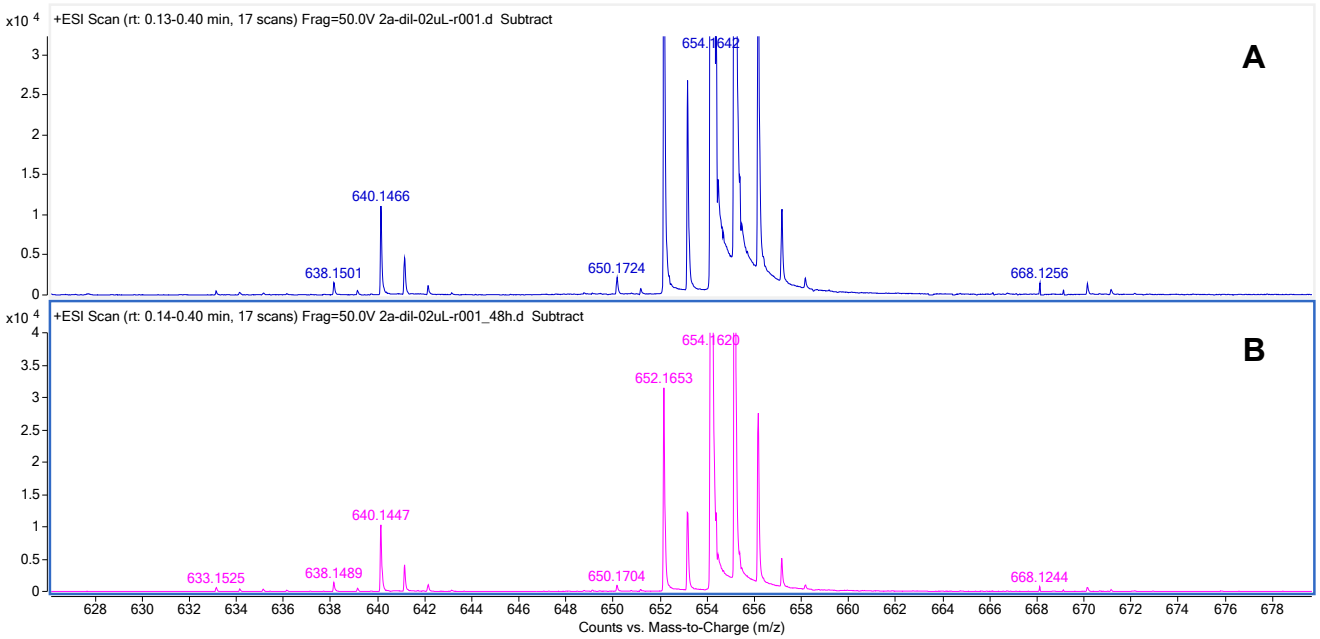

Figure S94. HR-ESI-QTOF-MS spectra of complex **5b** in DMEM/DMSO (9:1 v/v) at time zero (**A**) and after 48 h incubation at 37 °C (**B**)

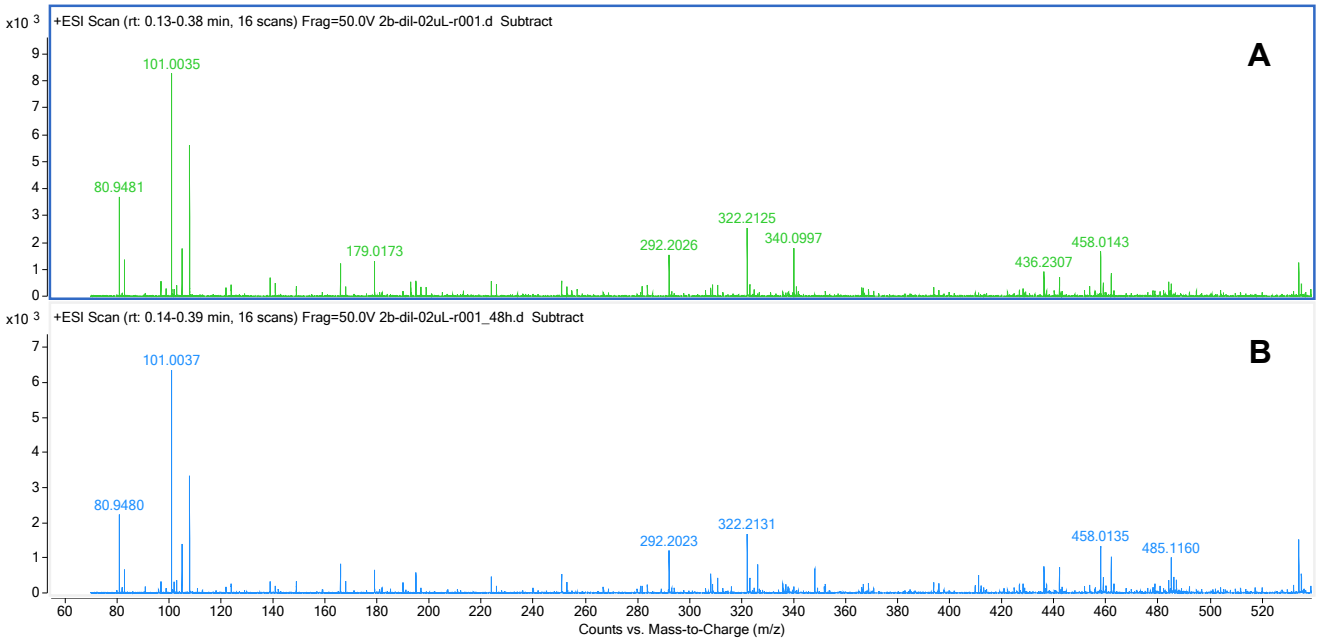

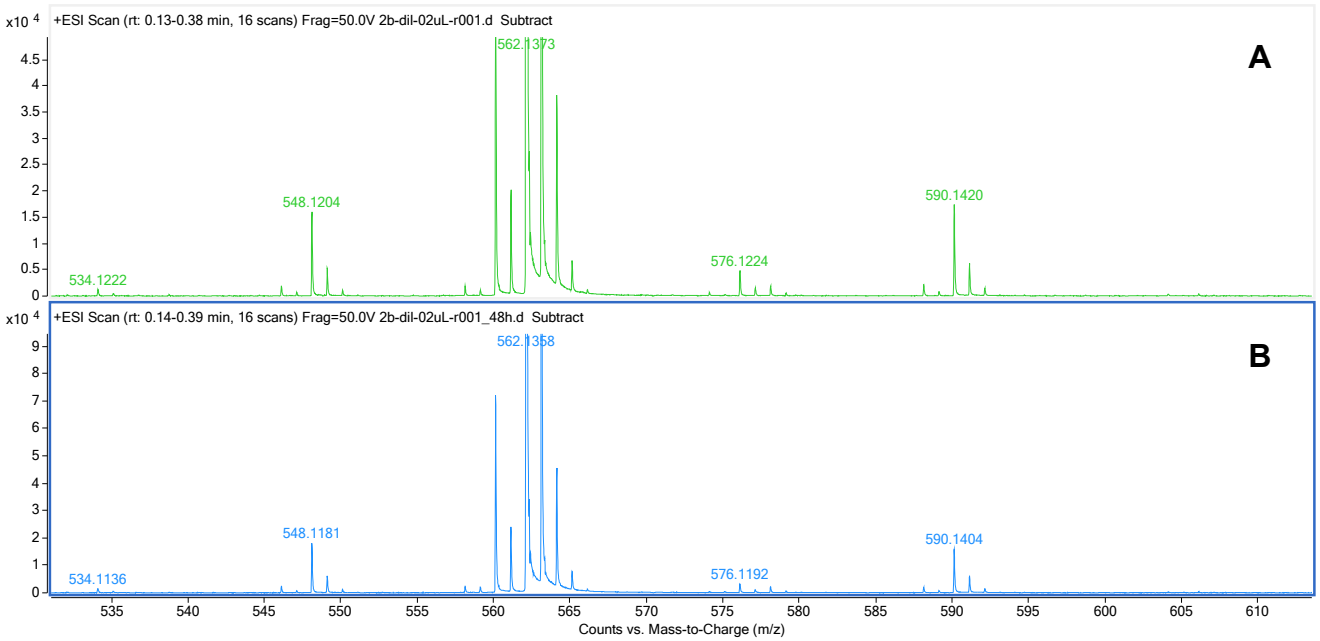

Figure S95. HR-ESI-QTOF-MS spectra of complex **5aEt** in DMEM/DMSO (9:1 v/v) at time zero (**A**) and after 48 h incubation at 37 °C (**B**)

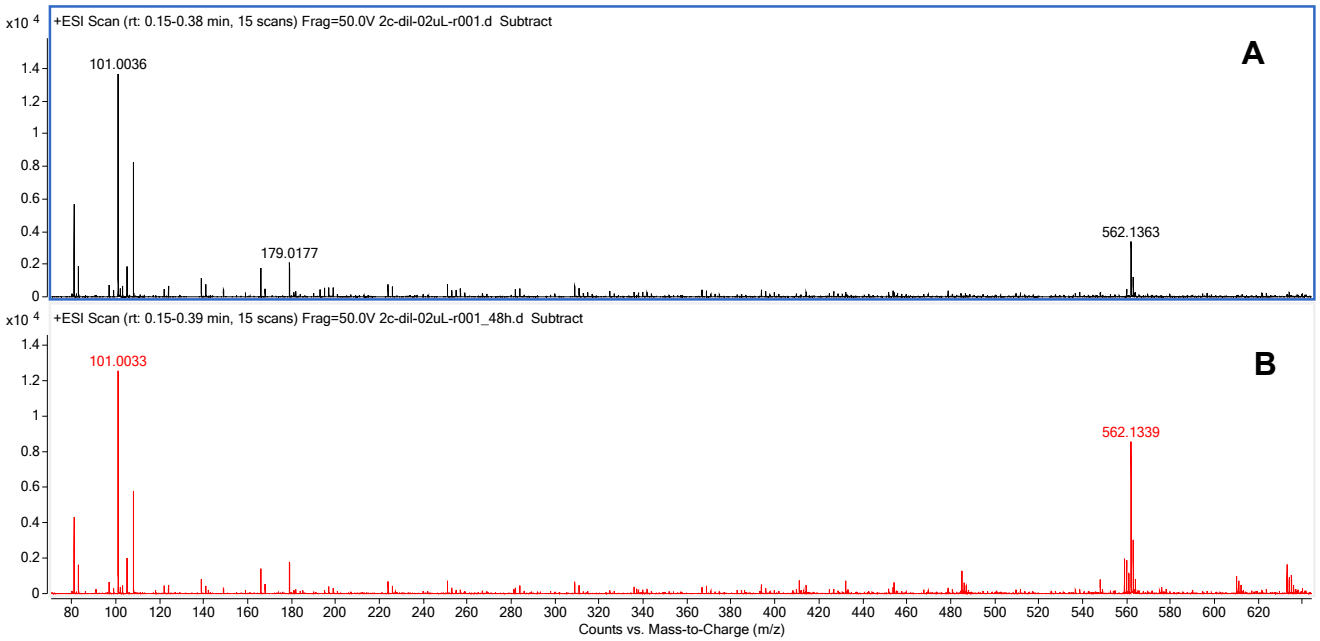

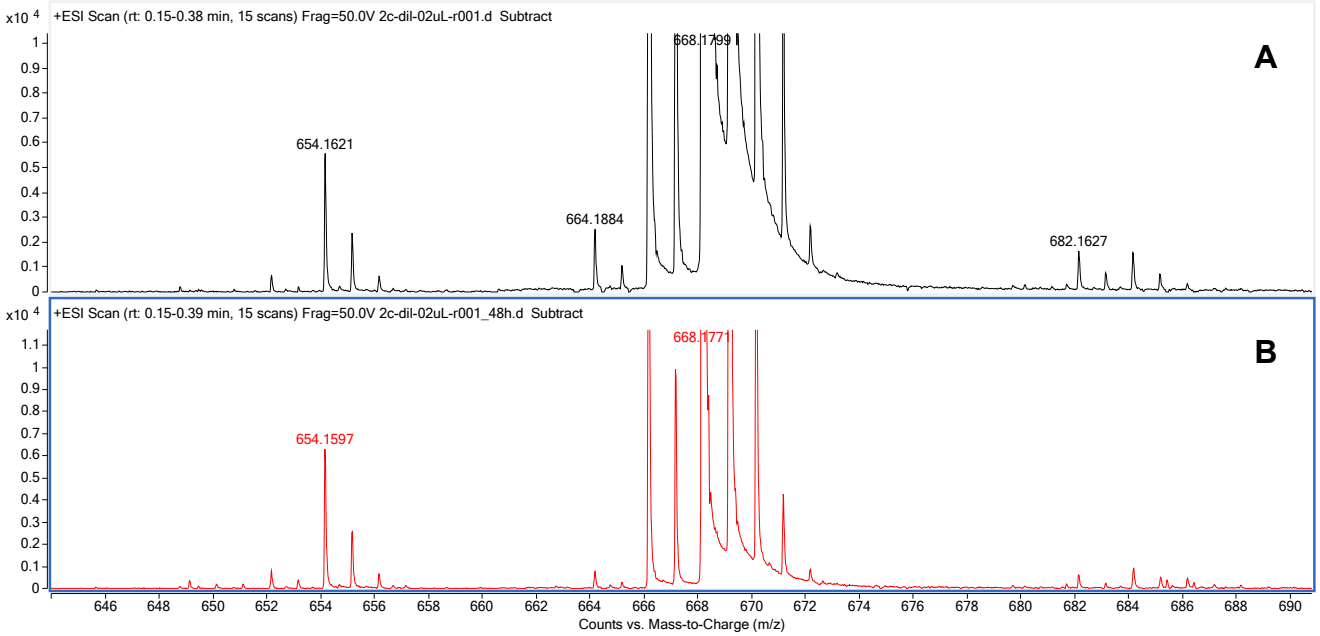

Table S16. Overview of stability data of ferrabenzene complexes in aqueous and dimethylsulfoxide solutions after 48h of incubation at 37°C (except for NMR experiments in 100% DMSO-d_6, conducted at room temperature). *Deuterated solvent.

	Medium	% DMSO	Complex concentration (M)	% detected complex after incubation	Method
5a	DMSO*	100*	5.7×10^{-3}	**92**	NMR
	H_2O	1	1.0×10^{-4}	**95**	UV-Vis
	H_2O	1	1×10^{-5}	**37**	HR-MS
	DMEM*	33*	2.4×10^{-3}	**80**	NMR
	DMEM	1	1×10^{-5}	**52**	HR-MS
5b	DMSO*	100*	8.7×10^{-3}	**97**	NMR
	H_2O	1	1.0×10^{-4}	**99**	UV-Vis
	H_2O	1	1×10^{-5}	**100**	HR-MS
	DMEM*	33*	3.8×10^{-3}	**89**	NMR
	DMEM	1	1×10^{-5}	**90**	HR-MS
5aEt	DMSO*	100*	5.5×10^{-3}	**94**	NMR
	DMSO	100	1×10^{-5}	**70**	HRMS
	H_2O	1	1.0×10^{-4}	**95**	UV-Vis
	H_2O	1	1×10^{-5}	**31**	HR-MS
	DMEM*	33*	1.0×10^{-3}	**76**	NMR
	DMEM	1	1×10^{-5}	**34**	HR-MS

5.7. Overview and discussion of stability data

The complexes are stable in DMSO-d_6 (92 – 97% of residual complexes after 48h incubation at room temperature) at concentrations comparable to those of the freshly prepared DMSO stock solutions used in cellular studies (approximately 10^{-2} M), thus validating DMSO as a suitable solvent for their initial dissolution (see Section 6.1 for details). At a significantly lower concentration level (10^{-5} M), the stability of **5aEt** in 100% DMSO decreased from 94% to 70%, as determined by HR-ESI-QTOF-MS. This dilution-dependent destabilization is a commonly observed phenomenon in metal complex chemistry.

In water at 10^{-4} M, UV–Vis data indicated 95–99% of residual intact complex after 48 h. At 10^{-5} M, HR-ESI-QTOF-MS evidenced reduced stability for **5a** and **5aEt** (31–37% residual complex), while **5b** retained full stability (100%). This contrasting behavior may correlate with the relatively higher hydrophilicity of **5b** (Log P_{ow} = 0.11, to be compared with 0.64 and 0.71 for **5a** and **5aEt**, respectively), which may contribute to its lower cytotoxicity.

Further UV-Vis experiments confirmed high stability of all complexes in 10% PBS and revealed no detectable interaction with GSH and NADH. The absence of GSH reactivity was confirmed by NMR using **5aEt** as a representative complex.

Stability in DMEM cell culture medium was assessed at 37 °C over 48h, via both NMR and HR-ESI-QTOF-MS (Section 5.6) on solutions differing in complex concentration and DMSO content: 33% DMSO for the NMR experiments, 1% DMSO for the MS analyses. MS results indicated that DMEM components do not alter the stability

trends observed in water. The detrimental effect of dilution was again confirmed, while **5b** consistently showed the highest stability (≈90%) across techniques. HR-ESI-QTOF-MS did not clearly reveal predominant metal fragments resulting from aqueous degradation.

Overall, these data indicate satisfactory stability of the complexes in aqueous media, and suggest a gradual decomposition process likely involving disassembly of the organometallic framework, similarly to what has been reported for other diiron bis(cyclopentadienyl) complexes.[1,11] This disassembly is presumably triggered in the cellular environment and is expected to release carbon monoxide and unidentified low-molecular-weight iron species, which may contribute to the observed increase in ROS production.

5.8. Dynamic Light Scattering analysis

Figure S96. Size distributions by intensity were determined by dynamic light scattering (DLS) using a Malvern ZetaSizer Nano ZS (scattering angle = 173°) at 25 °C, after an equilibrium time of 120 s. Stock solutions of the complexes (10 mM in DMSO) were diluted to a final concentration of 100 µM with Dulbecco's Modified Eagle Medium (DMEM) supplemented with 10% Fetal Bovine Serum (FBS), and filtered through a 0.22 µm membrane prior to measurement

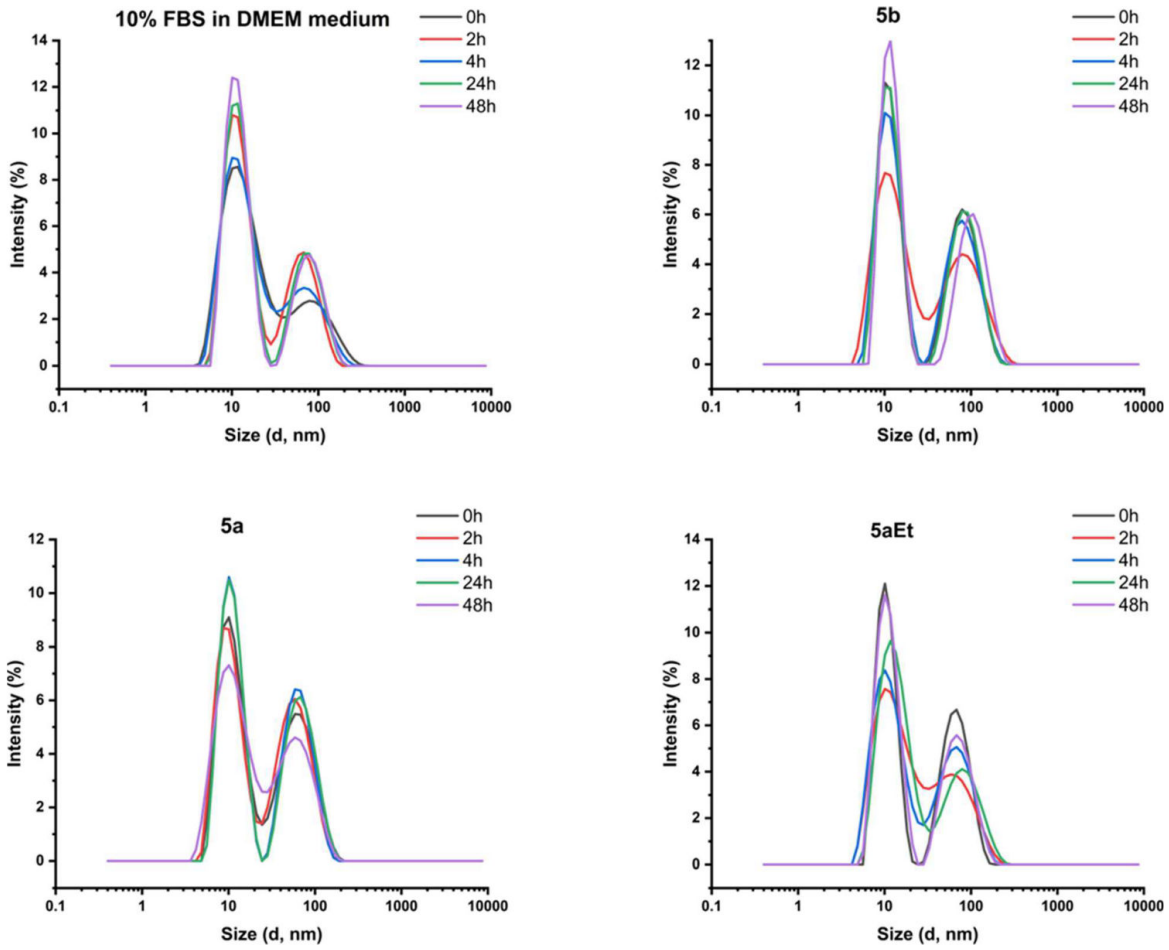

6. Cellular studies

6.1. Cytotoxicity

MCF7 cells were cultured in Dulbecco's Modified Eagle Medium (DMEM), A549 cells in F-12K, U87 cells in MEM, MRC-5 and RPE1 cells in DMEM/F-12 media (Gibco). All media were supplemented with 10% fetal bovine serum (FBS, Gibco) and 1% PenStrep (Gibco). MRC-5 and RPE1 cells were seeded in 96-well plates at a density of 8,000 cells per well, while U87, A549, and MCF7 cells were seeded at 4,000 cells per well, and incubated for 24 h. The complexes were dissolved in DMSO to prepare 10 mM stock solutions by accurately weighing the compounds and calculating molarities from their molecular weights. Freshly prepared stock solutions were subsequently diluted with culture medium, ensuring that the final DMSO concentration did not exceed 1% (v/v). After 24 h, the medium was replaced with fresh medium containing the complexes at the desired concentrations, and cells were incubated for an additional 48 h. Cell viability was then assessed by incubation with resazurin solution (0.2 mg/mL) for 4 h. Fluorescence was measured using a SpectraMax M2 Microplate Reader (λ_{exc} = 540 nm; λ_{em} = 590 nm). Data were normalized by defining 100% viability as the signal from the lowest tested concentration, and 0% viability as the signal from the highest concentration or from resazurin alone when no toxicity was observed. IC_{50} values were determined by non-linear regression using GraphPad Prism (v6). All experiments were performed in triplicate.

6.2. Cell Mitochondrial Stress Test

MRC-5 and A549 cells were seeded in Seahorse XFe96 well plates at a density of 20,000 cells/well in 80 µL medium, and cultured at 37°C for 24 h. The cells were then treated with the tested complexes at their IC_{50} concentration. After 24 h of incubation, the cells were washed twice with Seahorse Base Media and incubated in a non-CO_2 incubator at 37 °C for 1 h. The oxygen consumption rate (OCR) was measured following the sequential addition of oligomycin 10 µM, carbonyl cyanide 4-(trifluoromethoxy) phenylhydrazone (FCCP) 10 µM, and 10 µM rotenone and antimycin A. Data were analyzed using the Agilent Seahorse software.

6.3. ROS measurement

The level of reactive oxygen species (ROS) was measured using the commercially available dye 2′,7′-dichlorodihydrofluorescein (DCFH-DA). A549 cells were plated in 8-well plates with a density of 4 x 10^3 cells per well and allowed to adhere overnight. The medium was replaced with fresh medium containing the complexes at their IC_{50} concentration and hydrogen peroxide (H_2O_2, 200 µM). After 4 h of incubation, the cells were washed with cold PBS, and 20 µM DCFH-DA was added. Then, cells were incubated in the dark for 30 min, and ROS levels were assessed using confocal microscopy (Ex: 488 nm; Em:505 nm-550 nm).

Figure S97. IC_{50} plots for U87 cell line treated with metal complexes over 48 h. Data are presented as mean ± SD (n = 3), and error bars represent standard deviation

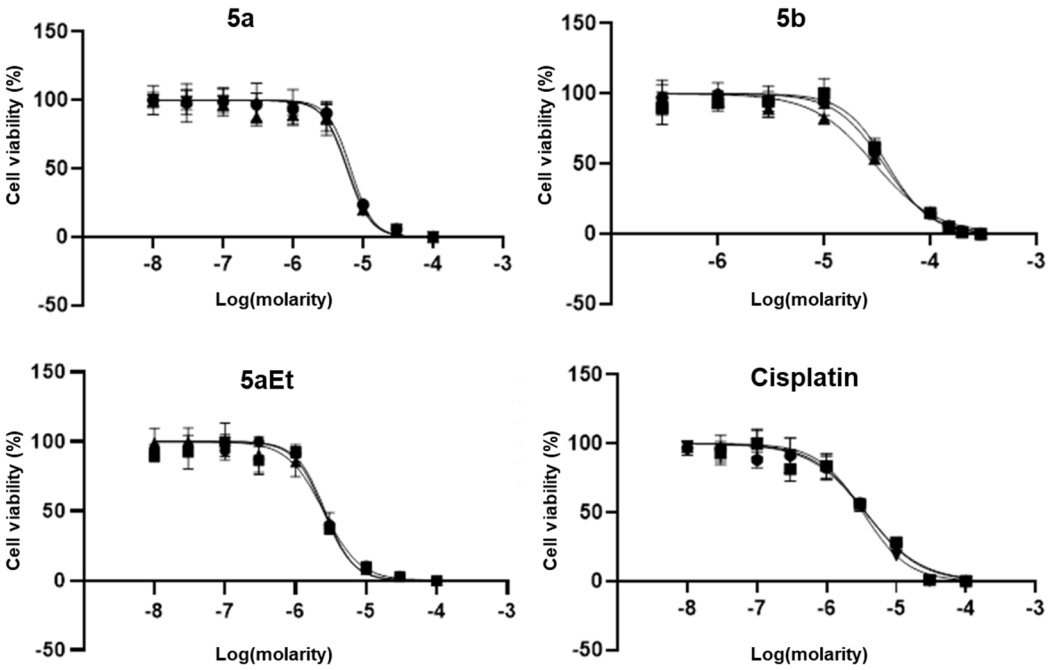

Figure S98. IC_{50} plots for MCF7 cell line treated with metal complexes over 48 h. Data are presented as mean ± SD (n = 3), and error bars represent standard deviation

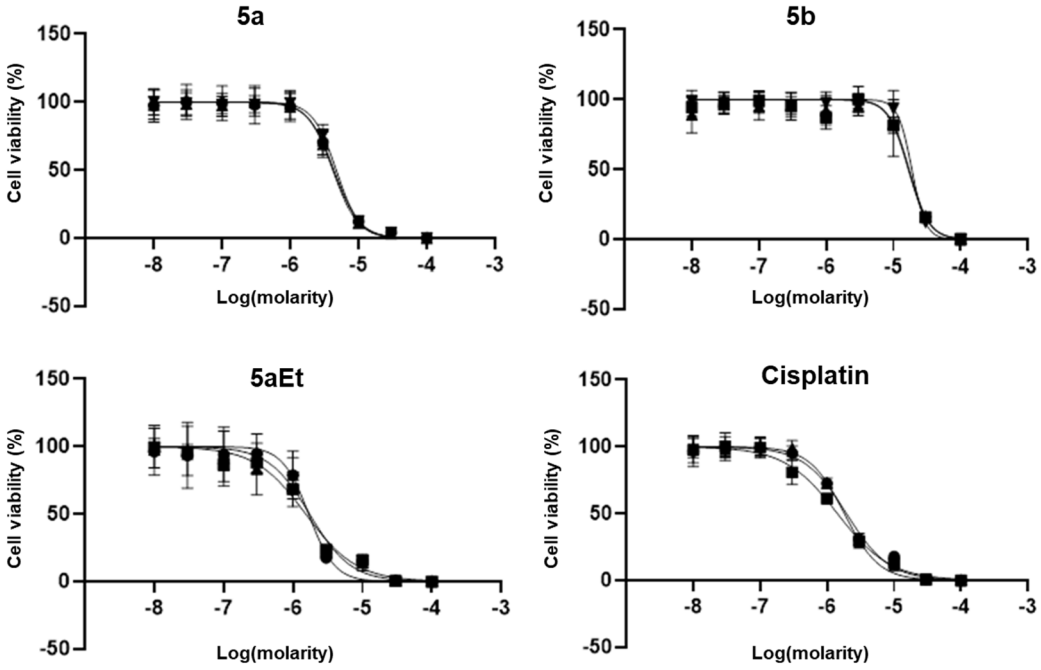

Figure S99. IC_{50} plots for A549 cell line treated with metal complexes over 48 h. Data are presented as mean ± SD (n = 3), and error bars represent standard deviation

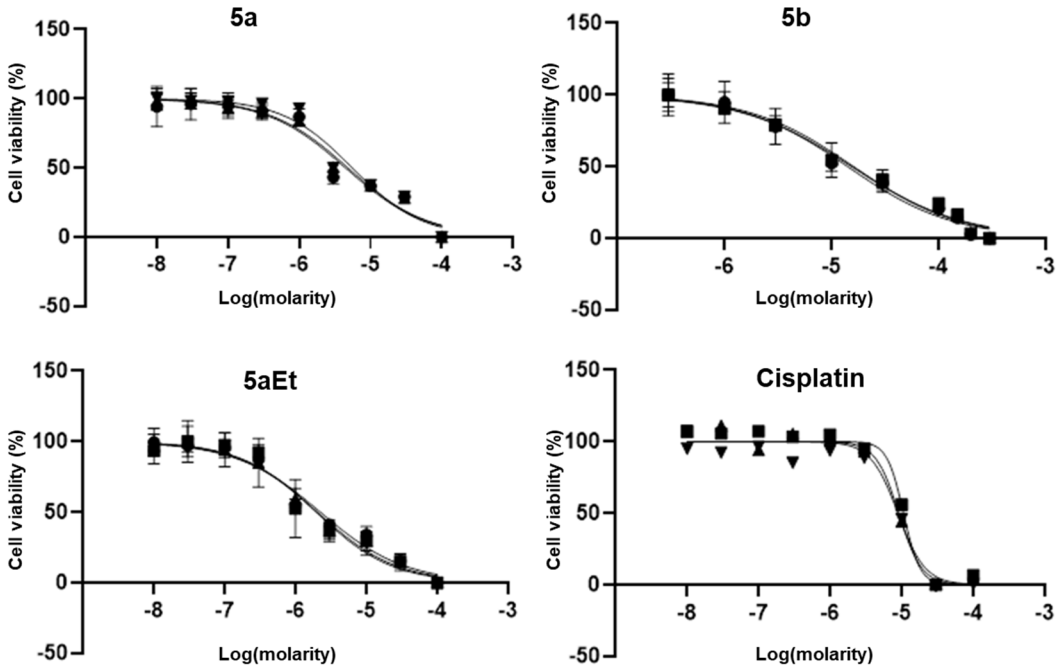

Figure S100. IC_{50} plots for RPE1 cell line treated with metal complexes over 48 h. Data are presented as mean ± SD (n = 3), and error bars represent standard deviation

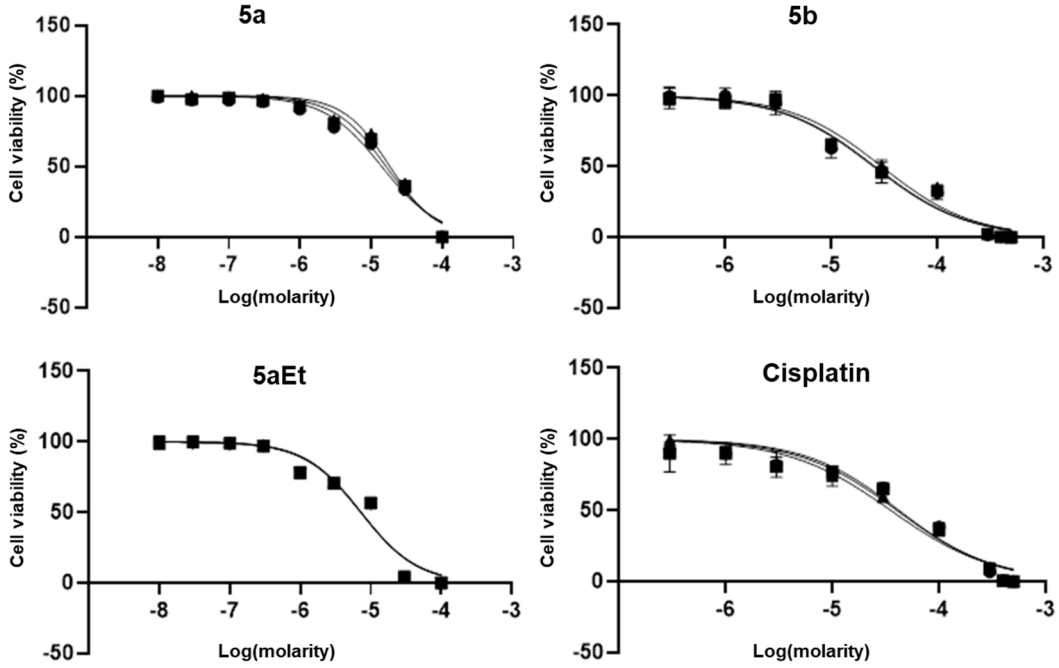

Figure S101. IC_{50} plots for MRC-5 cell line treated with metal complexes over 48 h. Data are presented as mean ± SD (n = 3), and error bars represent standard deviation

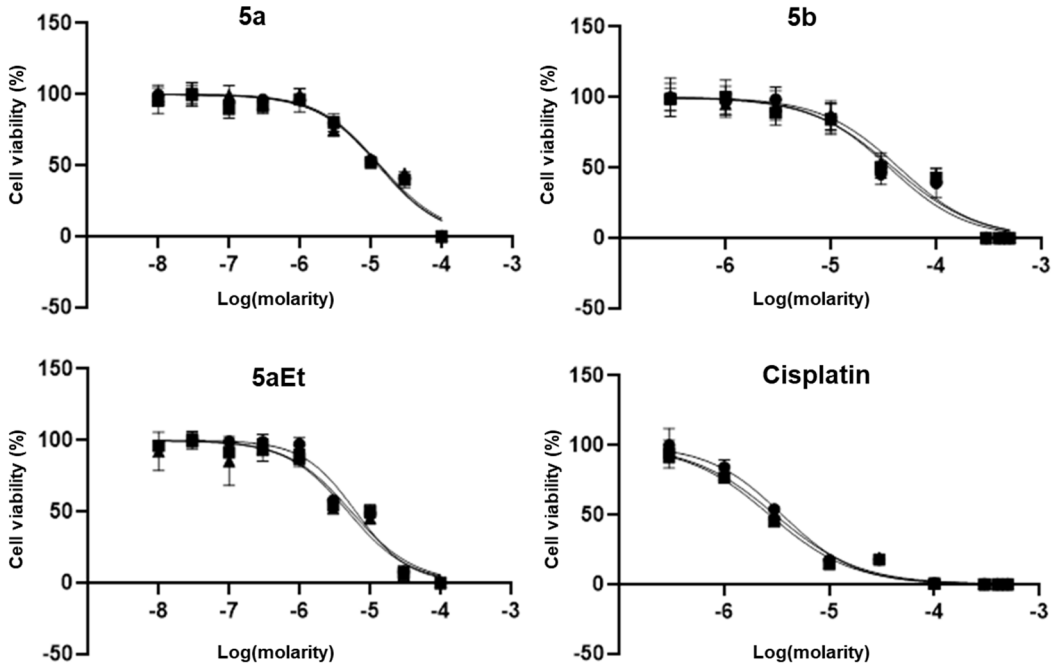

Figure S102. A) Cellular O_2 consumption in A549 cells, detected 24 h after treatment with metal complexes using the Seahorse analyzer. B) Quantitative comparison of basal respiration, ATP production and maximal respiration from panel A). Data are presented as mean ± SD (n = 3), and error bars represent standard deviation. Statistical analysis was performed using the non-parametric Kruskal-Wallis H test, followed by Dunn's post-hoc test for multiple comparisons. *p<0.05, **p<0.01 and ***p<0.001

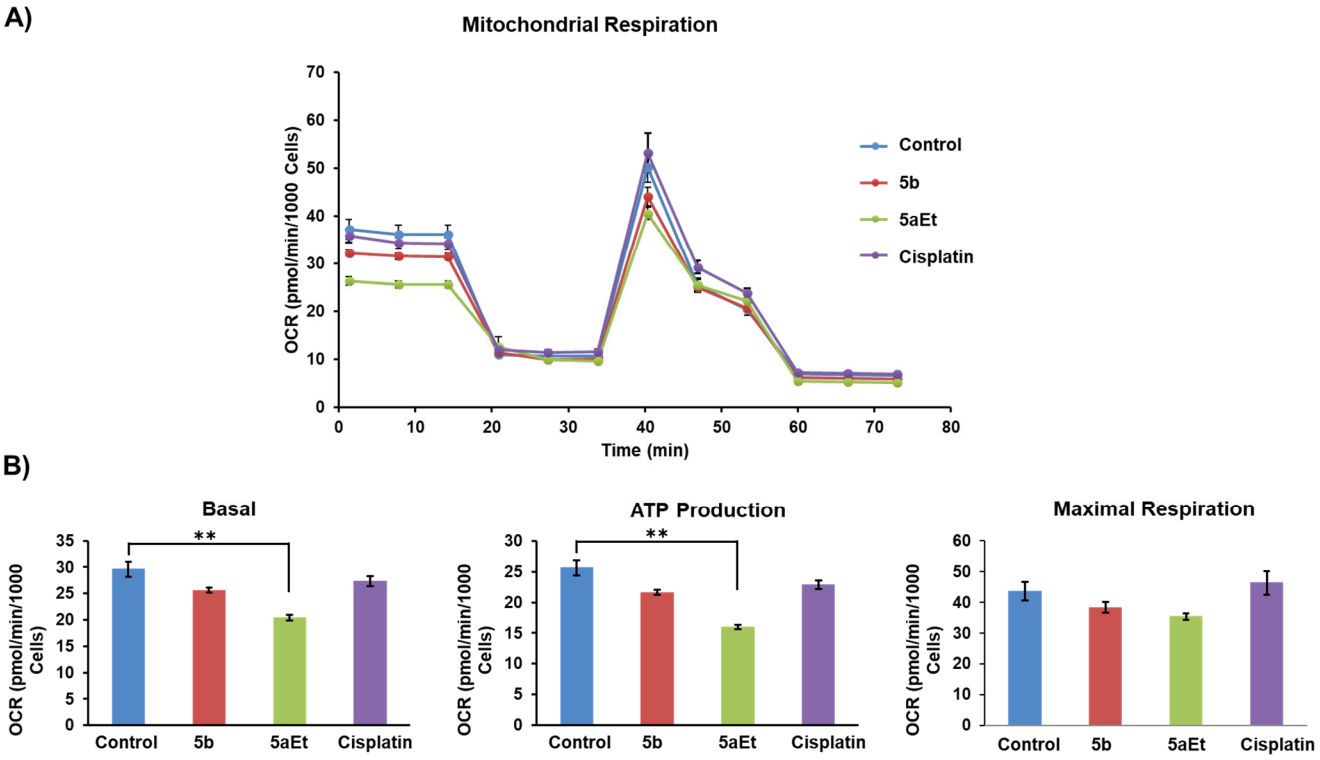

Figure S103. A) Cellular O_2 consumption in MRC-5 cells, detected 24 h after treatment with metal complexes using the Seahorse analyzer. B) Quantitative comparison of basal respiration, ATP production and maximal respiration from panel A). Data are presented as mean ± SD (n = 3), and error bars represent standard deviation

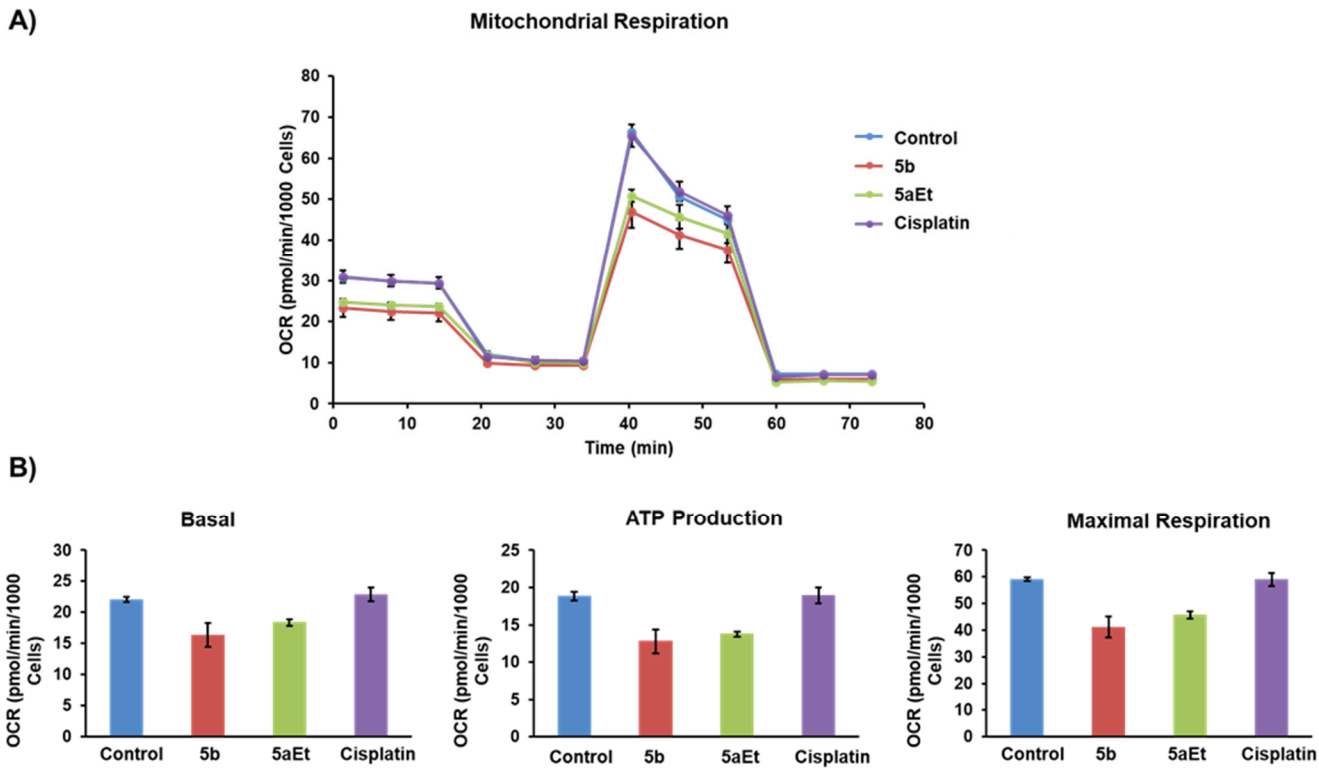

Notes and references

1 L. Biancalana, M. De Franco, G. Ciancaleoni, S. Zacchini, G. Pampaloni, V. Gandin, F. Marchetti, Easily Available, Amphiphilic Diiron Cyclopentadienyl Complexes Exhibit in Vitro Anticancer Activity in 2D and 3D Human Cancer Cells through Redox Modulation Triggered by CO Release, *Chem. Eur. J.* **2021**, *27*, 10169–10185.

2 F. Menges, "Spectragryph - optical spectroscopy software", Version 1.2.5, @ 2016-2017, http://www.effemm2.de/spectragryph.

3 G. R. Fulmer, A. J. M. Miller, N. H. Sherden, H. E. Gottlieb, A. Nudelman, B. M. Stoltz, J. E. Bercaw, K. I. Goldberg, NMR Chemical Shifts of Trace Impurities: Common Laboratory Solvents, Organics, and Gases in Deuterated Solvents Relevant to the Organometallic Chemist, *Organometallics* **2010**, *29*, 2176–2179.

4 W. Willker, D. Leibfritz, R. Kerssebaum, W. Bermel, Gradient selection in inverse heteronuclear correlation spectroscopy, *Magn. Reson. Chem.* **1993**, *31*, 287-292.

5 S. Benetti, M. Dalla Pozza, L. Biancalana, S. Zacchini, G. Gasser, F. Marchetti, The beneficial effect of cyclohexyl substituent on the in vitro anticancer activity of diiron vinyliminium complexes, *Dalton Trans.* **2023**, *52*, 5724–5741.

6 V. G. Albano, L. Busetto, M. Monari, V. Zanotti, Reactions of acetonitrile di-iron μ-aminocarbyne complexes; synthesis and structure of $[Fe_2(\mu\text{-}CNMe_2)(\mu\text{-}H)(CO)_2(Cp)_2]$, *J. Organomet. Chem.* **2000**, *606*, 163–168.

7 (a) G. Agonigi, G. Ciancaleoni, T. Funaioli, S. Zacchini, F. Pineider, C. Pinzino, G. Pampaloni, V. Zanotti, F. Marchetti, Controlled Dissociation of Iron and Cyclopentadienyl from a Diiron Complex with a Bridging C_3 Ligand Triggered by One-Electron Reduction, *Inorg. Chem*. **2018**, *57*, 15172−15186. (b) D. Rocco, L. K. Batchelor, E. Ferretti, S. Zacchini, G. Pampaloni, P. J. Dyson, F. Marchetti, Piano Stool Aminoalkylidene-Ferracyclopentenone Complexes from Bimetallic Precursors: Synthesis and Cytotoxicity Data, *ChemPlusChem* **2020**, *85*, 110–122. (c) L. Busetto, F. Marchetti, S. Zacchini, V. Zanotti, Deprotonation of μ-Vinyliminium Ligands in Diiron Complexes: A Route for the Synthesis of Mono- and Polynuclear Species Containing Novel Multidentate Ligands, *Organometallics* **2005**, *24*, 2297-2306.

8 G. M. Sheldrick, SADABS-2008/1 - Bruker AXS Area Detector Scaling and Absorption Correction, Bruker AXS: Madison, Wisconsin, USA, **2008**.

9 G. M. Sheldrick, Crystal structure refinement with SHELXL, *Acta Cryst. C* **2015**, *71*, 3-8.

10 M. Krejčik, M. Daněk and F. Hartl, Simple construction of an infrared optically transparent thin-layer electrochemical cell: Applications to the redox reactions of ferrocene, $Mn_2(CO)_{10}$ and $Mn(CO)_3$(3,5-di-t-butyl-catecholate)$^-$, *J. Electroanal. Chem.* **1991**, *317*, 179–187.

11 G. Agonigi, L. Biancalana, M. G. Lupo, M. Montopoli, N. Ferri, S. Zacchini, F. Binacchi, T. Biver, B. Campanella, G. Pampaloni, V. Zanotti, F. Marchetti, Exploring the Anticancer Potential of Diiron Bis-cyclopentadienyl Complexes with Bridging Hydrocarbyl Ligands: Behavior in Aqueous Media and In Vitro Cytotoxicity, *Organometallics* **2020**, *39*, 645−657.

12 a) OECD Guidelines for Testing of Chemicals, in OECD, Paris: 1995; Vol. 107. b) J. C. Dearden, G. M. Bresnen, The Measurement of Partition Coefficients, *Quant. Struct.-Act. Relat.* **1988**, *7*, 133-144.

13 D. J. Currie, C. E. Lough, R. F. Silver, H. L. Holmes, partition coefficients of some conjugated heteroenoid compounds and 1,4-naphthoquinones, *Can. J. Chem.* **1966**, *44*, 1035-1043.

14 (a) “Internal Standard Reference Data for qNMR: Dimethyl Sulfone”, **2018**, https://www.bipm.org/documents/20126/27085544/bipm%20publication-ID-3141/3e1311b4-d4c3-7b98-6f93-f2bcd6478b07. (b) R. J. Wells, J. Cheung, J. M. Hook, Dimethylsulfone as a universal standard for analysis of organics by QNMR, *Accred Qual Assur* **2004**, *9*, 450–456.

15 L. Pohl, M. Eckle, Sodium 3-(trimethylsilyl)tetradeuteriopropionate, a new water-soluble standard for ^{1}H NMR, *Angew. Chem. Int. Ed.* **1969**, *8*, 381.

16 Calculated by the formula pD = pH* + 0.4, where pH* is the value measured for H_2O-calibrated pH-meter. a) C. C. Westcott, pH Measurements; Academic Press: New York, **1978**. b) A. K. Covington, M. Paabo, R. A. Robinson, R. G. Bates, Use of the glass electrode in deuterium oxide and the relation between the standardized pD (paD) scale and the operational pH in heavy water, Anal. Chem. 1968, 40, 700-706.

17 R. N. Duffin, L. J. Stephens, V. L. Blair, L. Kedzierski, P. C. Andrews, The thiol-based reduction of Bi(V) and Sb(V) anti-leishmanial complexes, *J. Inorg. Biochem.* **2021**, *221*, 111470.